



— BUREAU OF —  
RECLAMATION

**Technical Memorandum No. 86-68330-2024-7**

# **Development of a New Velocity Model for the Paradox Valley Area**

**Paradox Valley Unit, Colorado**

**Upper Colorado Basin Region**





## **Mission Statements**

The U.S. Department of the Interior protects and manages the Nation's natural resources and cultural heritage; provides scientific and other information about those resources; honors its trust responsibilities or special commitments to American Indians, Alaska Natives, and affiliated Island Communities.

The mission of the Bureau of Reclamation is to manage, develop, and protect water and related resources in an environmentally and economically sound manner in the interest of the American public.



**Technical Memorandum No. 86-68330-2024-7**

# **Development of a New Velocity Model for the Paradox Valley Area**

**Paradox Valley Unit, Colorado  
Upper Colorado Basin Region**

Prepared by:

**Bureau of Reclamation  
Technical Service Center  
Denver, Colorado**



**Technical Memorandum No. 86-68330-2024-7**

# **Development of a New Velocity Model for the Paradox Valley Area**

**Paradox Valley Unit, Colorado  
Upper Colorado Basin Region**

**LISA BLOCK**

 Digitally signed by LISA BLOCK  
Date: 2024.08.05 15:50:46 -06'00'


---

Prepared by: Lisa Block, Geophysicist

## **Peer Review Certification**

This section has been reviewed and is believed to be in accordance with the service agreement and standards of the profession.



 DAVID HEESZEL  
2024.08.05 12:54:41 -06'00'

---

Peer reviewed by: David Heeszal, Geophysicist



# Acronyms and Abbreviations

1-D	one-dimensional
3-D	three-dimensional
API	American Petroleum Institute
dV <sub>P</sub>	perturbation to P-wave velocity
dV <sub>S</sub>	perturbation to S-wave velocity
dV <sub>SV</sub> , dV <sub>SH</sub>	perturbation to anisotropic S-wave velocity
ft	feet
km	kilometers
km/s	kilometers per second
m	meters
mag	duration magnitude
maxgap	maximum azimuthal gap in ray coverage
marr	number of arrival times
netCD	network common data form,
nPpicks	number of P-wave arrival times
nSpicks	number of S-wave arrival times
nsta	number of stations with arrival times
PVSN	Paradox Valley Seismic Network
PVU	Paradox Valley Unit
rms	root-mean-square
s	seconds
USGS	United States Geological Survey
V <sub>p</sub>	P-wave velocity
V <sub>s</sub>	S-wave velocity
V <sub>p</sub> /V <sub>s</sub>	Ratio of P-wave velocity to S-wave velocity

## Symbols

%	percent
°	degrees
=	equal to
>	greater than
≥	greater than or equal to
<	less than
≤	less than or equal to





# Contents

	Page
1.0 Introduction.....	1
1.1 Background.....	1
1.2 Geology.....	3
2.0 Method.....	6
2.1 Data Selection.....	6
2.2 Starting Velocity Model.....	10
2.3 Constraints.....	14
2.3.1 Velocity Regularization.....	14
2.3.2 First Induced Earthquakes.....	14
2.3.3 Velocity Well logs.....	14
2.3.4 Explosions.....	17
2.4 Inversion Procedure.....	17
3.0 Results.....	20
3.1 Arrival Time Residuals.....	20
3.2 Station Corrections.....	22
3.3 Velocities.....	23
3.4 Earthquake Locations.....	42
4.0 Conclusions.....	47
5.0 References.....	49

## Tables

Table	Page
Table 2-1: Starting model for the initial hypocenter-velocity inversion.....	12
Table 2-2: Elevation ranges of data points from smoothed velocity logs.....	16
Table 3-1: P-wave and S-wave arrival time residuals for five progressive models.....	21
Table 3-2: Station corrections for the final 1-D velocity model.....	22
Table 3-3: Station corrections for the final 3-D velocity model.....	22
Table 3-4: Final 1-D velocity model.....	23

## Figures

Figure	Page
Figure 1-1: Locations of the PVSN seismic stations, PVU injection well, and epicenters of earthquakes $\leq 10$ km deep recorded through 2023 .....	2
Figure 1-2: Vertical cross section roughly perpendicular to Paradox Valley, looking to the northwest.....	4
Figure 1-3: Stratigraphy and P-wave velocity (sonic) log in the PVU injection well. The entire well log is shown on the left, and the portion below 3.7 km depth is shown at expanded scale on the right. ....	5
Figure 2-1: Map of the Paradox Valley area showing the boundary of the velocity grid for the 3-D velocity inversions, all local earthquakes, earthquakes selected for inclusion in the inversion, all local events classified as explosions, and the explosions selected for inclusion in the inversions .....	8
Figure 2-2: Vertical cross sections showing the earthquakes and explosions selected for inclusion in the hypocenter-velocity inversions .....	9
Figure 2-3: Velocity-depth profiles of the regional crustal velocity models, the smoothed PVU P-wave velocity log, and the starting model for the initial hypocenter-velocity inversion: (a) P-wave velocities (b) S-wave velocities.....	11
Figure 2-4: Shallow P-wave velocity-depth profiles to -10 km elevation of the regional crustal velocity models, the smoothed PVU P-wave velocity log, and the starting model for the hypocenter-velocity inversion.....	13
Figure 2-5: Locations of wells within the inversion area where geophysical velocity well logs were available .....	15
Figure 2-6: Locations of velocity nodes in the initial coarse grid and the final finer grid used for the 3-D hypocenter-velocity inversions .....	19
Figure 3-1: (a) P-wave and (b) S-wave arrival time residuals of events located in the final models from the five stages of the progressive inversions.....	21
Figure 3-2: Initial and final 1-D P-wave and S-wave velocity models.....	23
Figure 3-3: (a) P-wave velocity and (b) S-wave velocity horizontal section through the final 3-D model at 1 km elevation.....	25

Figure 3-4: (a) P-wave velocity and (b) S-wave velocity horizontal section through the final 3-D model at 0 km elevation.....	26
Figure 3-5: (a) P-wave velocity and (b) S-wave velocity horizontal section through the final 3-D model at -1 km elevation.....	27
Figure 3-6: (a) P-wave velocity and (b) S-wave velocity horizontal section through the final 3-D model at -2 km elevation.....	28
Figure 3-7: (a) P-wave velocity and (b) S-wave velocity horizontal section through the final 3-D model at -3 km elevation.....	29
Figure 3-8: (a) P-wave velocity and (b) S-wave velocity horizontal section through the final 3-D model at -4 km elevation.....	30
Figure 3-9: (a) P-wave velocity and (b) S-wave velocity horizontal section through the final 3-D model at -5 km elevation.....	31
Figure 3-10: Locations of vertical cross sections presented in Figure 3-11 to Figure 3-14. ....	32
Figure 3-11: Vertical sections perpendicular to Paradox Valley through the final 3-D P-wave velocity model.....	33
Figure 3-12: Vertical sections perpendicular to Paradox Valley through the final 3-D S-wave velocity model.....	34
Figure 3-13: Vertical sections parallel to Paradox Valley through the final 3-D P-wave velocity model.....	35
Figure 3-14: Vertical sections parallel to Paradox Valley through the final 3-D S-wave velocity model.....	36
Figure 3-15: Velocity well logs compared to the final 3-D model velocities.....	38
Figure 3-16: Epicenters of earthquakes and explosions located in the final 1-D velocity model and in the final 3-D velocity model. ....	43
Figure 3-17: Vertical cross sections of earthquakes located in the final 1-D velocity model and in the final 3-D velocity model .....	44
Figure 3-18: Epicenters of earthquakes located in the previous 3-D velocity model from 2011 and in the new 3-D velocity model .....	45
Figure 3-19: Vertical cross sections of earthquakes located in the previous 3-D velocity model from 2011 and in the new 3-D velocity model .....	46

## Appendices

### Appendix

- A Mathematical Description of the Hypocenter-Velocity Inversion
- B Ray Coverage Plots
- C Electronic Attachment: 3-D Velocity Model and Station Corrections

# 1.0 Introduction

## 1.1 Background

The Bureau of Reclamation (Reclamation) operates the Paradox Valley Seismic Network (PVSN) in western Colorado (Figure 1-1). The purpose of this seismic network is to monitor earthquakes induced by a single deep injection well at Reclamation's Paradox Valley Unit (PVU), a component of the Colorado River Basin Salinity Control Program (Block et al., 2024). Installation of PVSN began in 1983, and the data have been continuously recorded and archived since 1985. When PVU injection began in July 1991, PVSN consisted of 14 stations. Thirteen of these stations had single-component, vertically oriented short-period seismometers, while the station closest to the injection well (PV11) had three components. Reclamation has upgraded PVSN several times over the years, and the network currently consists of 20 digital three-component broadband seismic stations and three strong motion sites. In six years of pre-injection monitoring (1985 to mid-1991), PVSN recorded only one naturally occurring local earthquake (within ~25 km of the injection well). Since injection began in July 1991, PVSN has recorded more than 11,000 induced earthquakes (Block et al., 2024).

In order for Reclamation staff to compute hypocenters of the local earthquakes and explosions recorded by PVSN, P-wave and S-wave velocity models of the subsurface are required. In the 1980s and early 1990s, readily available regional one-dimensional (1-D) velocity models were used for these calculations. As more local earthquakes were recorded by PVSN, the data were used to compute local 1-D, and later three-dimensional (3-D), velocity models to use in the hypocenter calculations. Station corrections were also computed as part of model development. As earthquakes occurred in new areas and additional seismic stations were added to PVSN, these models were periodically updated. These velocity models have been mentioned in previous Reclamation reports and publications (Ake et al., 2005; Block, 2020; Block et al., 2015), but the data and methods used to develop them have not been formally documented.

An updated 3-D body-wave tomographic velocity model and corresponding station corrections were recently computed for the Paradox Valley area. This model was developed by performing a series of hypocenter-velocity inversions, during which velocities, station corrections, and earthquake hypocenters were determined simultaneously from arrival time data. The data and methods used to develop this model are documented in this report. Similarities to the methodology used previously include: use of P-wave and S-wave arrival times from local earthquakes and explosions, setting the  $z$  coordinates of explosions to be at the local ground surface, using velocity regularization to create smooth models, and constraining the hypocenters of the 22 earthquakes recorded during the first injection test (in July 1991) to be near the deviated PVU wellbore at the depth of the Leadville formation (the primary target injection formation). Improvements in the current methodology compared to previous implementations include incorporation of well log velocities from 23 boreholes in the Paradox Valley area and computation of an independent 3-D S-wave velocity ( $V_s$ ) model. In previous implementations,

Technical Memorandum 86-68330-2024-7  
Development of a New Velocity Model for the Paradox Valley Area

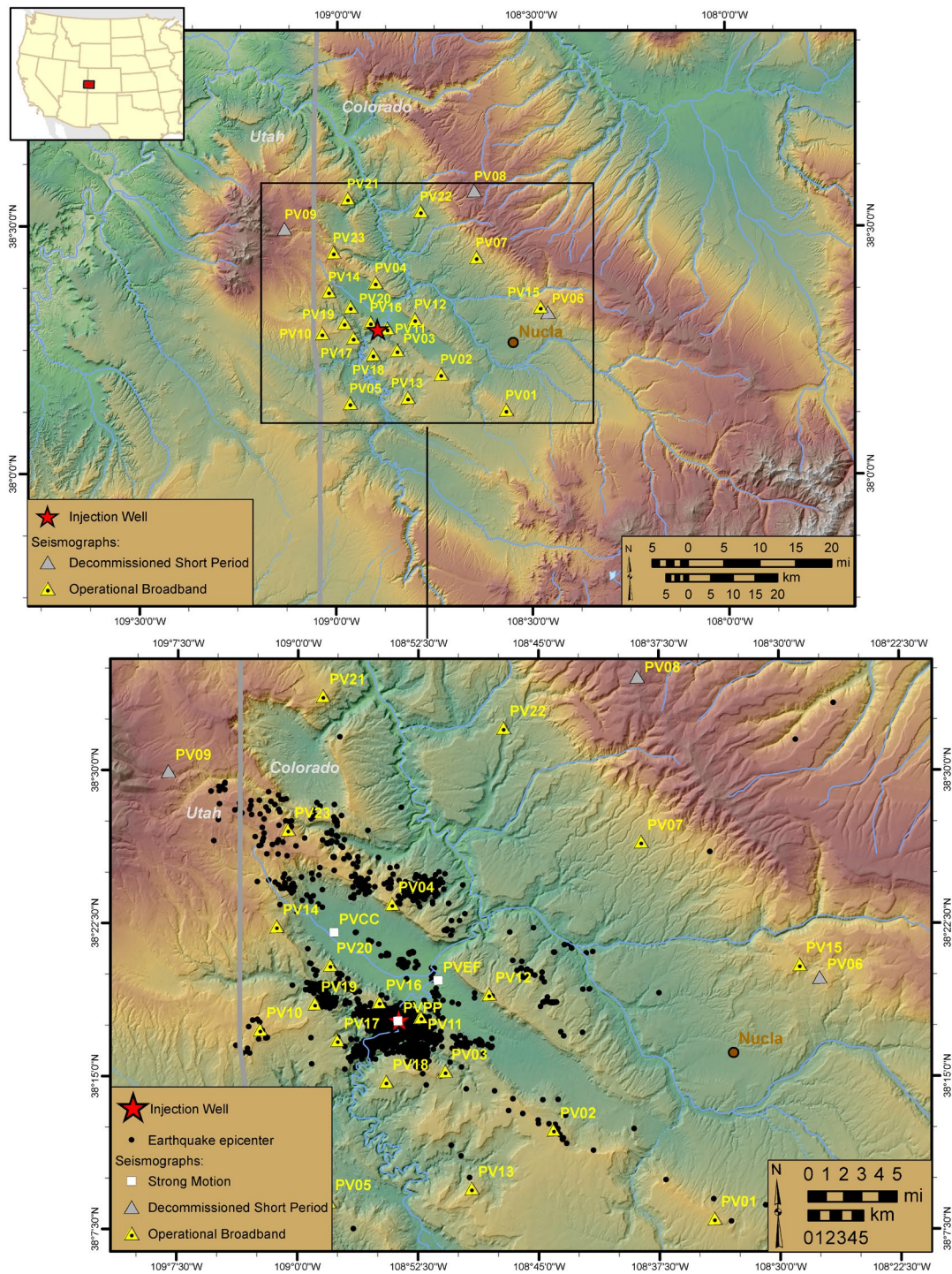


**Figure 1-1: Locations of the PVSN seismic stations, PVU injection well, and epicenters of earthquakes  $\leq 10$  km deep recorded through 2023. Station PV06 was decommissioned in 1994 due to repeated vandalism and replaced by PV15. Stations PV08 and PV09, which were at locations with poor site response, were decommissioned in 2015 when the network was upgraded from short-period sensors to broadband instrumentation. Figure from Block et al. (2024).**

the velocity structure was parameterized by a 3-D P-wave velocity ( $V_p$ ) model and a 1-D  $V_p/V_s$  model. Independent 3-D P-wave and S-wave velocity models were produced during the inversions documented in this report because many more S-wave arrival times are available now than in the past, due to upgrades of all seismic stations to three-component sensors (Block et al., 2024).

## 1.2 Geology

The geology of the Paradox Valley area is characterized by sub-horizontal sedimentary units and a northwest-trending salt anticline underlying Paradox Valley (Figure 1-2). Sedimentary units present in the Paradox Valley area are Cretaceous through Cambrian in age, although not all units are present in all locations. These units consist of sandstones, siltstones, shales, conglomerates, limestones, dolomites, and evaporites (King et al., 2014). The underlying Precambrian basement is composed of granite, schist, gneiss, and pegmatite (King et al., 2014). The rock units generally dip slightly to the northeast and are offset by a series of northwest-trending normal faults (Figure 1-2). The Pennsylvanian-age Paradox salt units are composed of up to 85% halite (Huntoon, 1988) and flow in response to tectonic deformation. As a result, the thickness of the Paradox formation can vary widely over relatively short distances. The Paradox formation was deformed into a series of northwest-trending diapiric salt anticlines in the Paradox Basin area of eastern Utah and western Colorado. This deformation occurred mainly during the Permian Period, in response to differential sediment loading from uplift and erosion of the Uncompahgre highland (Kluth and DuChene, 2009; Trudgill and Paz, 2009). One of these salt anticlines underlies Paradox Valley (Figure 1-2).

Based on regional core and log data, the Mississippian Leadville carbonate was selected as the primary injection zone for the PVU injection well, with the upper Precambrian as a secondary zone (Bremkamp and Harr, 1988). The overlying Paradox salt formation acts as a confining layer.

The P-wave velocity (sonic) log from the PVU injection well indicates a strong velocity contrast between the relatively high-velocity Leadville formation and the overlying formations (Figure 1-3). The overlying Molas, Pinkerton Trail, and lower Paradox formations, including the Paradox salt members and lower Ismay member, have relatively low P-wave velocities compared to most other formations. The lowest velocities occur in the main salt units of the Paradox formation.



Technical Memorandum 86-68330-2024-7  
Development of a New Velocity Model for the Paradox Valley Area

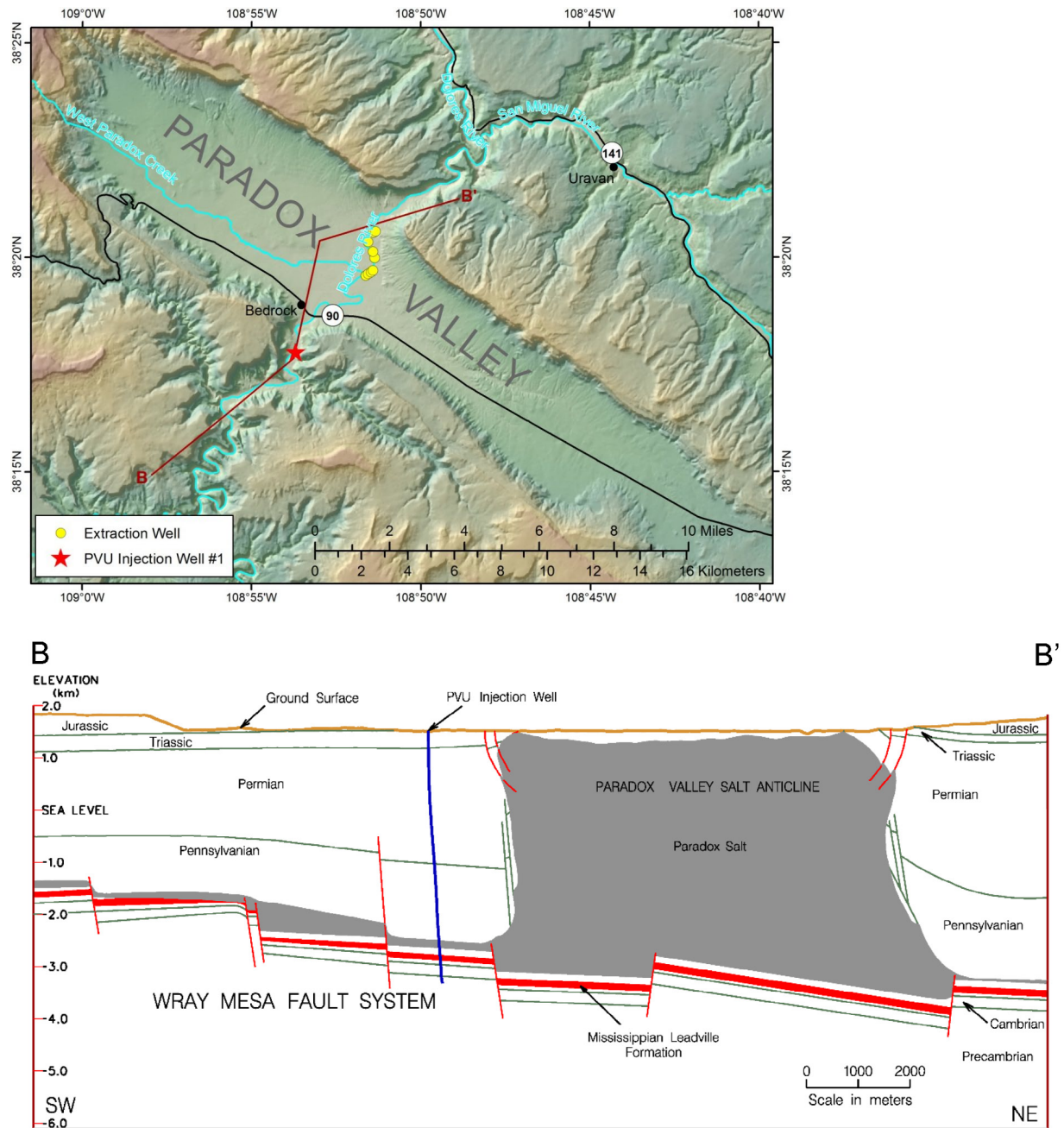


**Figure 1-2: Vertical cross section roughly perpendicular to Paradox Valley, looking to the northwest. The location of the cross section is shown on the map above. Based on figure from Bremkamp and Harr (1988). Taken from Block et al. (2024).**



# Technical Memorandum 86-68330-2024-7 Development of a New Velocity Model for the Paradox Valley Area

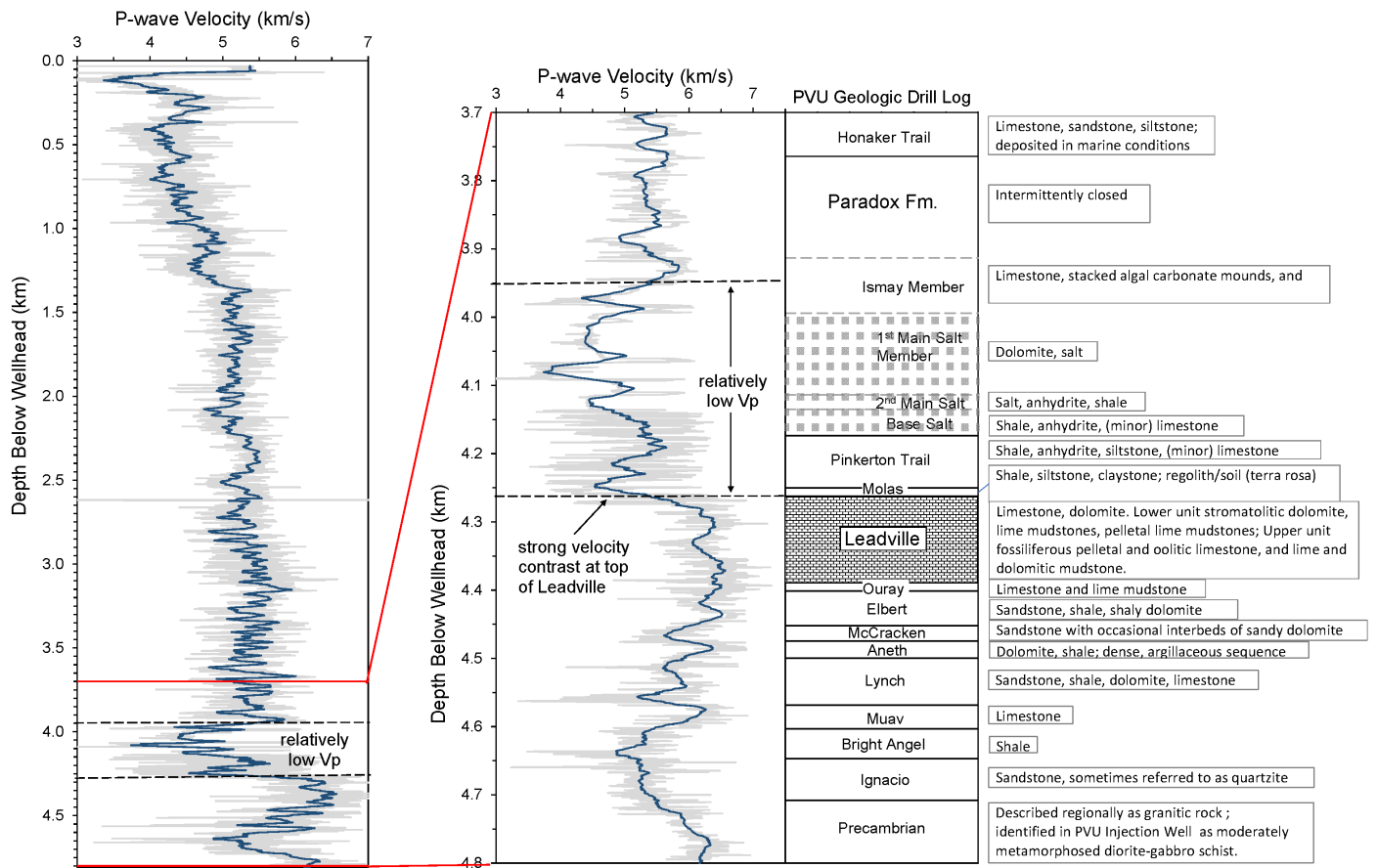


**Figure 1-3: Stratigraphy and P-wave velocity (sonic) log in the PVU injection well. The entire well log is shown on the left, and the portion below 3.7 km depth is shown at expanded scale on the right. The depths of geologic units and the sonic log are from the final geologic well report (Harr, 1988). Depths are relative to the ground surface and have been corrected for borehole deviation. Lithologic descriptions are from King et al. (2014) . The original sonic log with 0.5-ft (0.15-m) sampling (faint gray lines) and a smoothed log from a 51-ft (15.5-m) centered running average (dark blue lines) are shown.**

## 2.0 Method

Three-dimensional P-wave and S-wave velocity models for the Paradox Valley area were computed by performing a series of hypocenter-velocity inversions of P-wave and S-wave arrival times of local earthquakes and explosions with well-constrained hypocenters. The P-wave and S-wave velocity models were determined simultaneously but are independent, other than the indirect coupling through the earthquake hypocenters. P-wave and S-wave station corrections for all PVSN stations were also determined during the inversions.

The hypocenter-velocity inversions were performed in a local Cartesian coordinate system, with the origin of the system at the PVU injection well. The axes were rotated 55° counterclockwise, so that they align with the trend of Paradox Valley. This orientation was used because the strongest lateral velocity variations are expected to be associated with the salt anticline underlying the valley.

The velocity models are represented by a rectangular 3-D grid of velocity nodes. The velocity at any point is computed by tri-linear interpolation of the velocities of the eight surrounding nodes. The P-wave and S-wave velocity models use the same set of node points. The area within which the velocities varied during the inversions is shown by the 30 km by 50 km white rectangular outline on the map in Figure 2-1. This inversion area was restricted to the region where sufficient redundant event-station ray coverage was available to reasonably constrain the 3-D velocity models. For segments of ray paths that lie outside this boundary, the velocities were extrapolated by including extra planes of distant velocity nodes that have the same values as the nodes on the edges of the inversion boundary.

The nonlinear hypocenter-velocity inversion was performed by iteratively solving the linearized problem. The inversion was formulated as a least squares inversion, but residual weighting was used to approximate an L1-norm optimization. Weighted constraints were included to produce smooth velocities models, reduce inversion non-uniqueness, and to incorporate seismic velocity data from geophysical borehole logs. A mathematical description of the inversion method is provided in Appendix A.

### 2.1 Data Selection

A subset of local earthquakes with reasonably well-constrained hypocenters was selected for inclusion in the hypocenter-velocity inversion. The hypocenters in the dataset from which earthquakes were selected were from the combined PVSN earthquake catalog containing data through 2022. This catalog contains relative event locations (developed using time differences from waveform cross-correlations) for approximately 86% of the local earthquakes, and absolute locations for the remaining events (which do not have sufficient data to tie into the relative location procedure). Both the absolute and relative event location algorithms use a local 3-D velocity model developed previously. Since only absolute arrival times were used in the hypocenter-velocity inversions documented here, the selection criteria were based on the

absolute arrival time data and did not consider the time difference data. The selected events meet the following criteria:

- number of stations with arrival times ( $nsta$ )  $\geq 8$
- number of arrival times ( $narr$ )  $\geq 9$
- number of P-wave arrival times ( $nPpicks$ )  $\geq 8$
- number of S-wave arrival times ( $nSpicks$ )  $\geq 1$
- maximum azimuthal gap in ray coverage ( $maxgap$ )  $\leq 230^\circ$
- distance to closest station with arrival time divided by hypocenter depth  $\leq 3$
- root-mean-square arrival time residual ( $rms$ )  $\leq 0.5$  seconds (s)
- duration magnitude ( $mag$ )  $\geq 0.0$

These criteria were adjusted to incorporate some earthquakes from all the local seismically active areas while eliminating events with the most poorly constrained hypocenters. In addition to the criteria listed above, the local earthquakes were also selected based on their geographical location. This was done to produce a more spatially uniform distribution of hypocenters for input into the inversion. The spatial selection was performed by dividing the geographical area into 1 km x 1 km x 1 km cells (in the rotated Cartesian system) and limiting the number of earthquakes in each cell to a maximum of 10. If there were more than 10 earthquakes in a cell that meet the hypocenter selection criteria listed above, then they were prioritized during the spatial selection based on (in this order): most  $nSpicks$ , smallest  $maxgap$ , most  $nPpicks$ , most  $nsta$ , smallest  $rms$ . This initial selection contained 1,454 earthquakes. Once the initial selection was made, the waveforms for 307 of the earthquakes with the least robust hypocenters were manually examined. These events were generally those with  $narr < 10$  and/or  $rms > 0.1$  s. The arrival times for these events were manually repicked, and some of them were eliminated from the dataset due to poor data quality. The number of local earthquakes in the reviewed dataset was 1,319. All local earthquakes and the final selected subset are shown on the map in Figure 2-1.

A subset of local explosions was also selected for inclusion in the hypocenter-velocity inversion, using a similar procedure as that described above for the earthquakes. Many of these explosions are likely associated with mining in the greater Paradox area; some may be blasts associated with road work or other construction activities. The hypocenter selection criteria were adjusted because explosions don't produce direct S-wave arrivals and because they generally have larger magnitudes than many of the PVU-induced earthquakes. The criteria used were:

- $nsta \geq 8$
- $narr \geq 8$
- $nPpicks \geq 8$
- $nSpicks = 0$
- $maxgap \leq 230^\circ$
- $rms \leq 0.5$  s
- $mag \geq 0.5$

No criterium for distance to the closest station divided by hypocenter depth was used because the hypocenter depths of the explosions are set to be at the ground surface during the inversions, as discussed below (section 2.3.4). Because the explosions are at the ground surface, the spatial selection process only binned the data horizontally, using a 1-km x 1-km cell size. Because many

Technical Memorandum 86-68330-2024-7  
Development of a New Velocity Model for the Paradox Valley Area

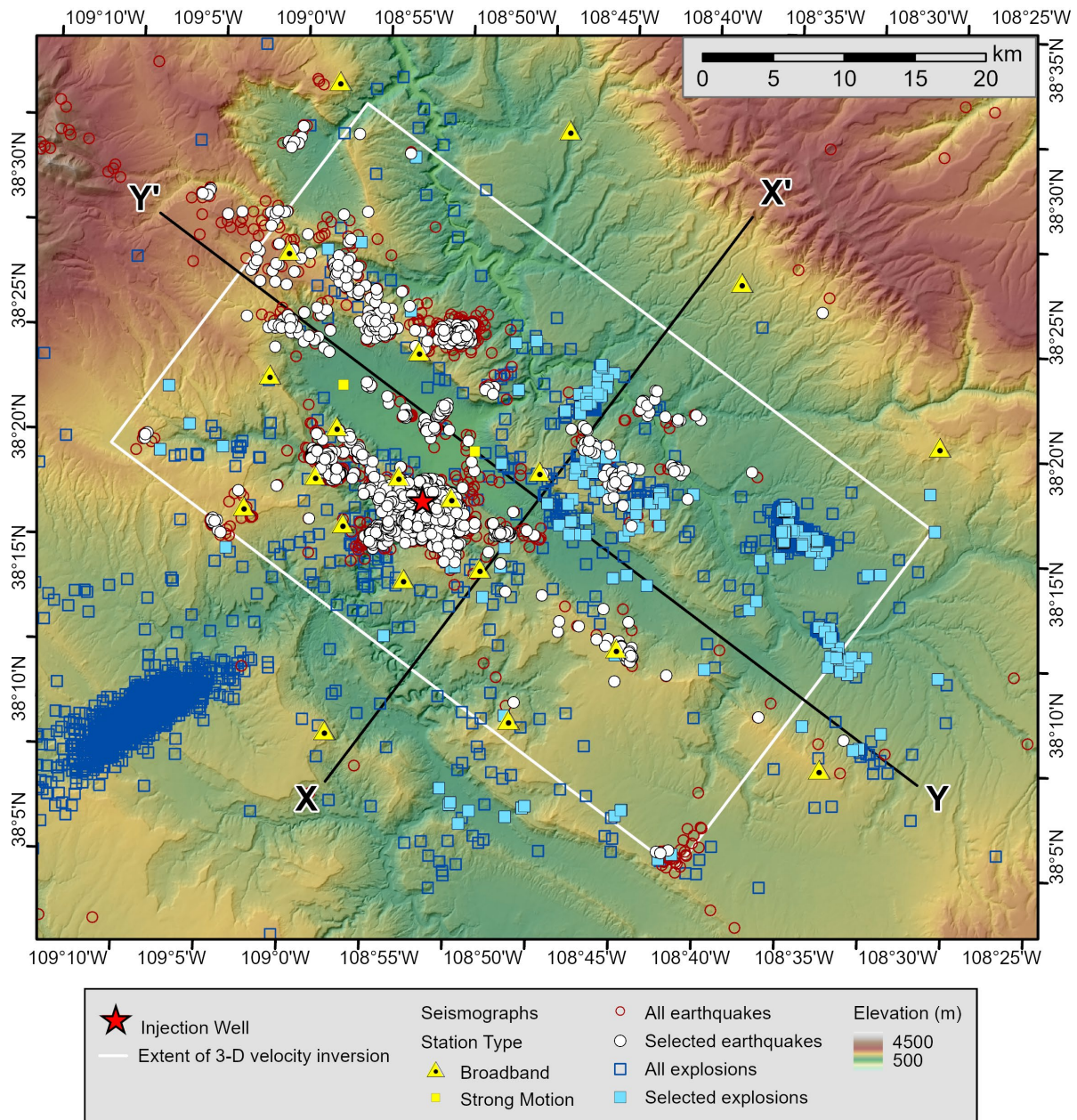
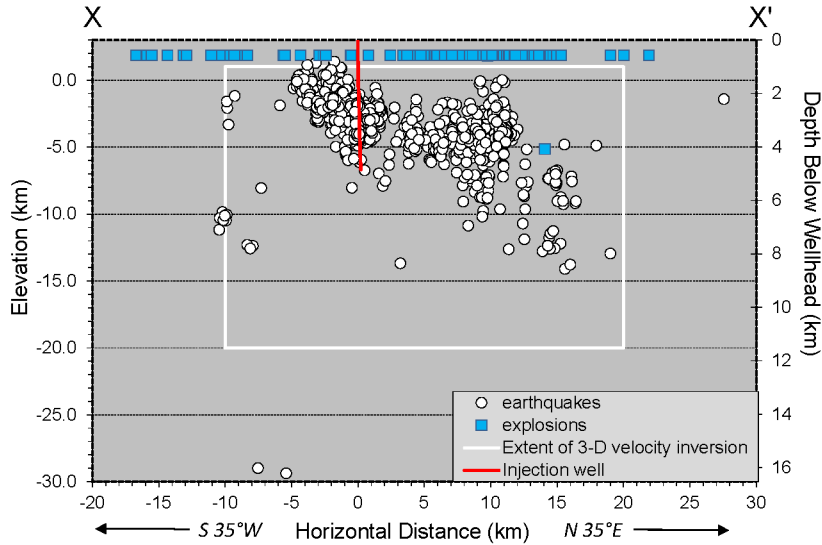


**Figure 2-1: Map of the Paradox Valley area showing the boundary of the velocity grid for the 3-D velocity inversions (white rectangle), all local earthquakes (red open circles), earthquakes selected for inclusion in the inversions (filled white circles), all local events classified as explosions (open dark blue squares), and the explosions selected for inclusion in the inversions (filled light blue squares). The PVU injection well and PVSN seismic stations are shown for reference, as indicated in the legend. Vertical cross sections indicated by lines X-X' and Y-Y' are shown in Figure 2-2.**

(a) Section perpendicular to Paradox Valley, looking to the northwest



(b) Section parallel to Paradox Valley, looking to the southwest

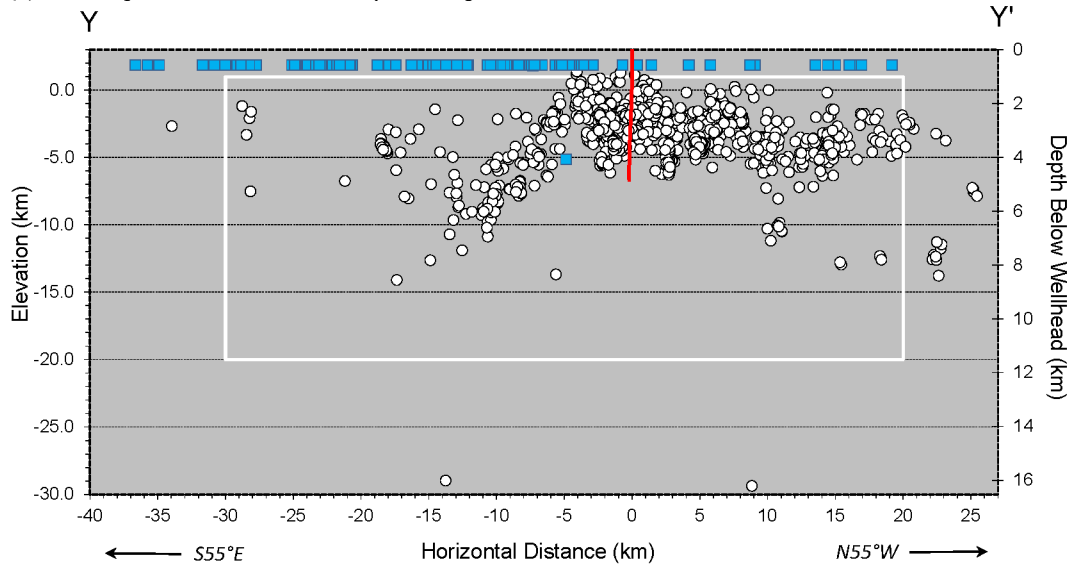


**Figure 2-2: Vertical cross sections showing the earthquakes (white circles) and explosions (blue squares) selected for inclusion in the hypocenter-velocity inversions. All events are projected onto the sections: (a) perpendicular to Paradox Valley, X coordinates increase to the northeast (b) parallel to Paradox Valley, Y coordinates increase to the northwest. The white rectangles indicate the boundary of the velocity grid for the 3-D inversions. The depth scale is relative to the ground surface at the PVU injection well (1.524 km elevation). Orientations of these cross sections are shown in Figure 2-1. The single deep explosion seen in these plots was mis-located in the original data set but was constrained to be at the ground surface during the hypocenter-velocity inversions.**

of the explosions occur at or near the same location, the maximum number of explosions accepted per cell was 5. The same criteria were used for prioritizing explosions within cells as for the earthquakes. This initial dataset contained 393 explosions. The waveforms for all of these explosions were manually reviewed and repicked or eliminated based on data quality. Some of the events classified as explosions, especially the spatially scattered events, may not be explosions but rather other non-earthquake seismic events, such as rock falls. (They lack the strong surface waves typical of near-surface explosions.) These events were eliminated. The final reviewed dataset contained 208 explosions. All local events classified as explosions and the final subset of explosions selected for inclusion in the inversions are shown on the map in Figure 2-1.

As discussed below in section 2.3.2, the hypocenters of the 22 induced earthquakes that occurred near the PVU injection well during the first injection test in July 1991 are used as constraints in the inversion. Adding these 22 earthquakes to the 1,319 local earthquakes and 208 explosions selected based on data quality and spatial location results in a set of 1,549 events for inclusion in the hypocenter-velocity inversions.

Despite efforts to make the distribution of events included in the inversions as spatially uniform as feasible, strong variations still exist. The majority of local earthquakes, virtually all of which are induced by PVU injection, occur in the northwestern two-thirds of the inversion area (Figure 2-1). In addition, the depths of the clusters of induced earthquakes vary, with the deeper earthquakes generally occurring on the northeast side of Paradox Valley. This spatial variation is due to basement faulting, which down-drops the deep geologic units targeted for PVU injection to the northeast, across a series of northwest-trending normal faults (King et al., 2014; see Figure 1-2). In addition, most of the explosions, which mainly constrain shallow velocities, occur in the southeastern half of the inversion area (Figure 2-1). The 3-D distribution of selected earthquakes and explosions is illustrated by the vertical cross sections shown in Figure 2-2.

## 2.2 Starting Velocity Model

For the initial, or starting, velocity model, P-wave and S-wave velocity-depth profiles were constructed by combining regional crustal velocity models and well log velocities from the PVU injection well. The regional models were used for the deeper velocity nodes, while the PVU well log was used for the shallowest nodes. The regional velocity models, PVU well log velocities, and the starting model derived from them are presented in Figure 2-3 and Table 2-1.

Three regional crustal models were used:

- DNA13 (Porritt et al., 2014) – model of perturbations to P-wave velocity ( $dV_P$ , %) and anisotropic S-wave velocity ( $dV_{SV}$ ,  $dV_{SH}$ , %), based on the Pollitz and Snoke (2010) reference model. The model was determined from inversion of teleseismic earthquake body wave data and surface wave phase velocities from teleseismic earthquakes and ambient noise. The reference model uses local crustal thicknesses to vary the depth to the moho. I assumed a crustal thickness of 40 km for the PVSN region, based on



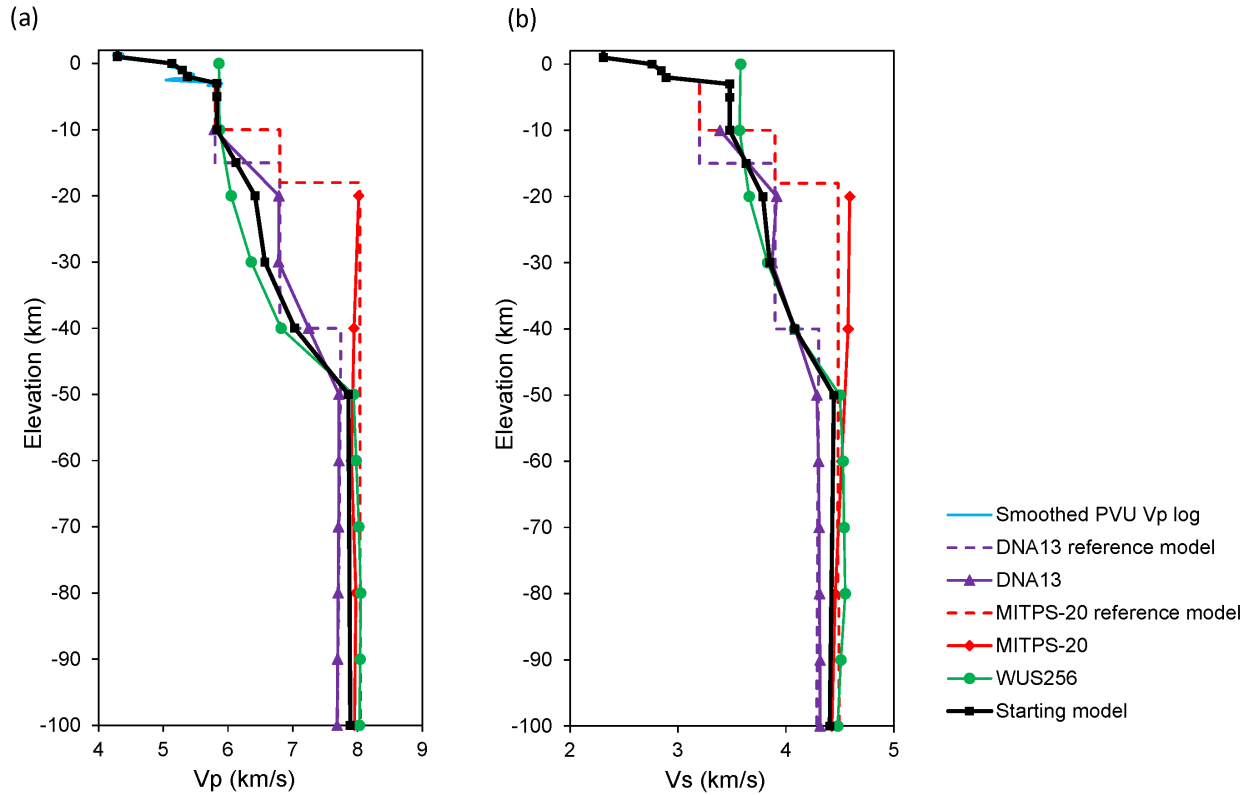


**Figure 2-3: Velocity-depth profiles of the regional crustal velocity models, the smoothed PVU P-wave velocity log, and the starting model for the initial hypocenter-velocity inversion: (a) P-wave velocities (b) S-wave velocities.**

Chulick and Mooney (2002) (which is referenced by Porritt et al. (2014) ), as well as a 2013 report completed by the U.S. Nuclear Regulatory Commission under an agreement with the United States Geological Survey (USGS) (Anooshehpour, 2013) and associated 2021 USGS data release (Mooney and Boyd, 2021). This model contains velocity values every 10 km from 0 to -400 km elevation; values from -10 to -100 km elevation were incorporated into the starting model for the initial hypocenter-velocity inversion. The  $V_{sv}$  component was used for the starting S-wave velocity model.

- MITPS-20 (Golos et al., 2020) -  $dV_p$  and  $dV_s$  (%) model, based on the AK135 reference model (Kennett et al., 1995). The model was determined from inversion of earthquake P-wave and S-wave arrival times and Rayleigh wave phase velocities. This model contains values every 20 km from -20 to -300 km elevation. The model does not reflect the local crustal thickness in the Paradox Valley area ( $\sim 40$  km), and therefore the value at -20 km elevation was discarded. An interpolated value at -50 km elevation and the value at -100 km elevation were incorporated into the starting model.

**Table 2-1: Starting model for the initial hypocenter-velocity inversion**

Elevation (km)	Vp (km/s)	Vs (km/s)	Vp/Vs	Vp source	Vs source
1	4.29	2.31	1.86	smoothed PVU well log	computed from Vp using Vp/Vs from PVU well logs <sup>1</sup>
0	5.13	2.76	1.86	smoothed PVU well log	computed from Vp using Vp/Vs from PVU well logs <sup>1</sup>
-1	5.29	2.85	1.86	smoothed PVU well log	computed from Vp using Vp/Vs from PVU well logs <sup>1</sup>
-2	5.38	2.89	1.86	smoothed PVU well log	computed from Vp using Vp/Vs from PVU well logs <sup>1</sup>
-3	5.83	3.48	1.68	DNA13, WUS256 at -10 km	DNA13, WUS256 at -10 km
-5	5.83	3.48	1.68	DNA13, WUS256 at -10 km	DNA13, WUS256 at -10 km
-10	5.83	3.48	1.68	DNA13, WUS256	DNA13, WUS256
-15	6.12	3.63	1.69	DNA13, WUS256	DNA13, WUS256
-20	6.42	3.79	1.69	DNA13, WUS256	DNA13, WUS256
-30	6.57	3.85	1.71	DNA13, WUS256	DNA13, WUS256
-40	7.03	4.08	1.72	DNA13, WUS256	DNA13, WUS256
-50	7.86	4.44	1.77	DNA13, WUS256, MITPS-20	DNA13, WUS256, MITPS-20
-100	7.89	4.41	1.79	DNA13, WUS256, MITPS-20	DNA13, WUS256, MITPS-20

<sup>1</sup>A median Vp/Vs ratio of 1.86 was computed from Vp and Vs logs acquired in the PVU injection well from ~-2.8 to ~-3.1 km elevation.

- WUS256 (Rodgers et al., 2022) - Vp and Vs (km/s) model determined from adjoint waveform tomography of earthquake data. This model contains velocity values every 10 km from 0 to -400 km elevation. The values from -10 to -100 km elevation were incorporated into the starting model.

Network common data form (netCD, .nc) files and associated metadata and documentation files for these crustal velocity models were downloaded from the *Earthscope Data Services* website (<https://ds.iris.edu/ds/products>, accessed late December, 2023). Text files containing the reference models for the DNA13 and MITPS-20 perturbation models were also downloaded from the *Earthscope* website. The netCDF files were imported into *Arcgis Pro*, and rasters were created from them. These rasters were then clipped to the extent of PVSN, and average values at each elevation of interest were determined. For the two perturbation models, the layered reference model velocities (in km/s) and mean clipped model raster values (percent perturbations in velocity) were combined to compute the total velocities. The starting velocity profiles for the initial hypocenter-velocity inversion were constructed using averages of the velocities from the regional crustal velocity models at and below -10 km elevation.

Above -3 km elevation, P-wave velocities from the well log in the PVU injection well, smoothed by a moving average with a window length of 0.5 km, were used (Figure 2-4). PVU well log S-wave velocities are only available for the deepest section of the well, from approximately -2.8 to -3.3 km elevation. The Vp/Vs ratios computed from the well log data indicate that Vp/Vs is



fairly uniform above about -3.1 km elevation. Therefore, the median  $V_p/V_s$  ratio between  $\sim -2.8$  and  $\sim -3.1$  km elevation was computed (1.86) and used to calculate corresponding S-wave velocities from the smoothed  $V_p$  well log values above -3 km elevation (Table 2-1).

Precambrian basement was encountered near the bottom of the PVU injection well, at an elevation of -3.18 km. The well did not penetrate far enough into the basement to get representative values of P-wave and S-wave velocities in unfractured, unweathered basement. Therefore, the values from the regional crustal models at an elevation of -10 km were projected up to -3 km elevation (the velocity node closest to the top of basement) for the starting model (Figure 2-4, Table 2-1).

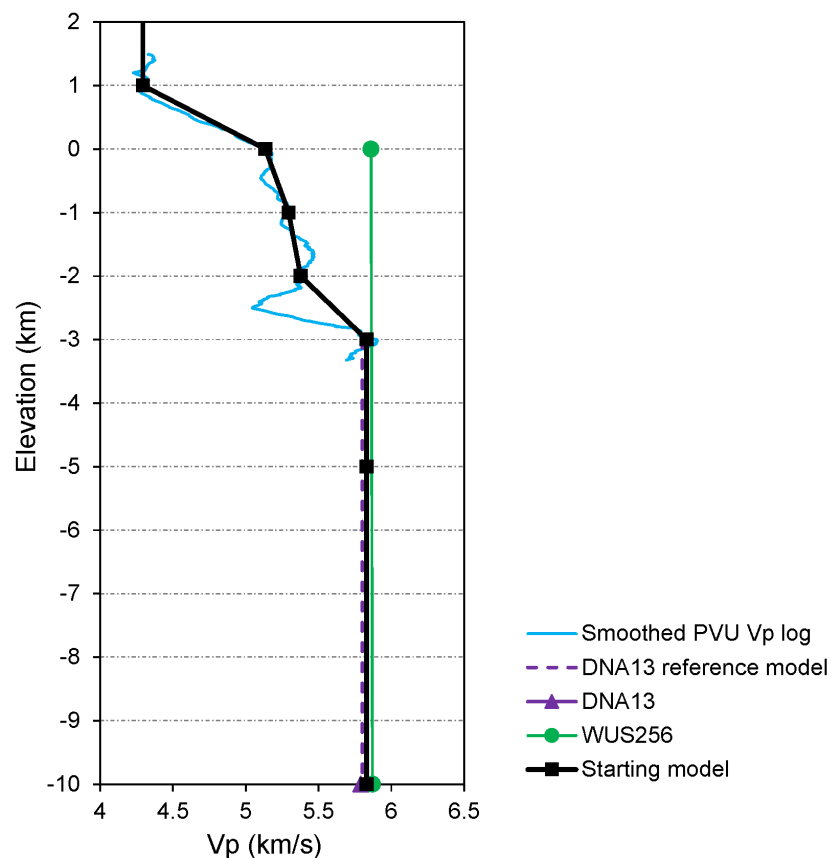


**Figure 2-4: Shallow P-wave velocity-depth profiles to -10 km elevation of the regional crustal velocity models, the smoothed PVU P-wave velocity log, and the starting model for the initial hypocenter-velocity inversion.**

## **2.3 Constraints**

Five constraints were included in the hypocenter-velocity inversions. These constraints helped reduce model non-uniqueness. Three of these constraints were incorporated as weighted constraints. These constraints included: an assumption about the approximate location of the initial induced earthquakes, velocity values from geophysical well logs, and velocity model regularization (smoothing). These constraints were weighted to influence the model solution toward satisfying them, but to also allow the solution to deviate from them if the arrival time data require it. The other two constraints were included as fixed (non-weighted constraints): the explosions were required to occur at the local ground surface, and the sum of the P-wave station corrections was required to be zero.

### **2.3.1 Velocity Regularization**

To reduce velocity fluctuations in areas with limited ray coverage, velocity regularization was applied. This was a weighted constraint that sought to minimize first spatial velocity derivatives in each coordinate direction. A separate weighting scheme was used for the P-wave and S-wave velocity structures because the resolution of each model was different due to differing ray coverage and because the sum-squared P-wave and S-wave residuals were different.

### **2.3.2 First Induced Earthquakes**

The induced earthquakes that were recorded during the first PVU injection test were constrained to locate near the PVU injection borehole, at the mid-depth of the perforations in the Leadville formation. This injection test was conducted in July 1991 and lasted 14 days. Twenty-two induced earthquakes were recorded near the injection well during the test. The hypocenters of these events are within 80 m of each other following event relative relocation based on waveform cross-correlations, and most of them nearly co-locate. Hence, the data indicate that they occurred at practically the same location. Due to the short duration of the injection test and the low permeability of the target injection formations, it is reasonable to assume that these events occurred close to the injection well. Furthermore, a flow profile conducted in the PVU wellbore in 1993 indicated that 83% of the fluid was flowing into the Leadville formation (Envirocorp Services and Technology Inc., 1995), and thus it is reasonable to assume that the initial induced earthquakes occurred close to that depth. Taking the deviation of the PVU injection well into account, this constraint weighted these first 22 earthquakes to occur near the location ( $x = 0.182$  km,  $y = -0.210$  km,  $z = -2.8$  km).

### **2.3.3 Velocity Well Logs**

P-wave and S-wave velocities were constrained to match data from geophysical borehole logs in the Paradox Valley area. Within the 3-D inversion boundary, P-wave velocity logs were available from 23 wells, and S-wave velocity logs were available from 3 of these wells

Technical Memorandum 86-68330-2024-7  
Development of a New Velocity Model for the Paradox Valley Area

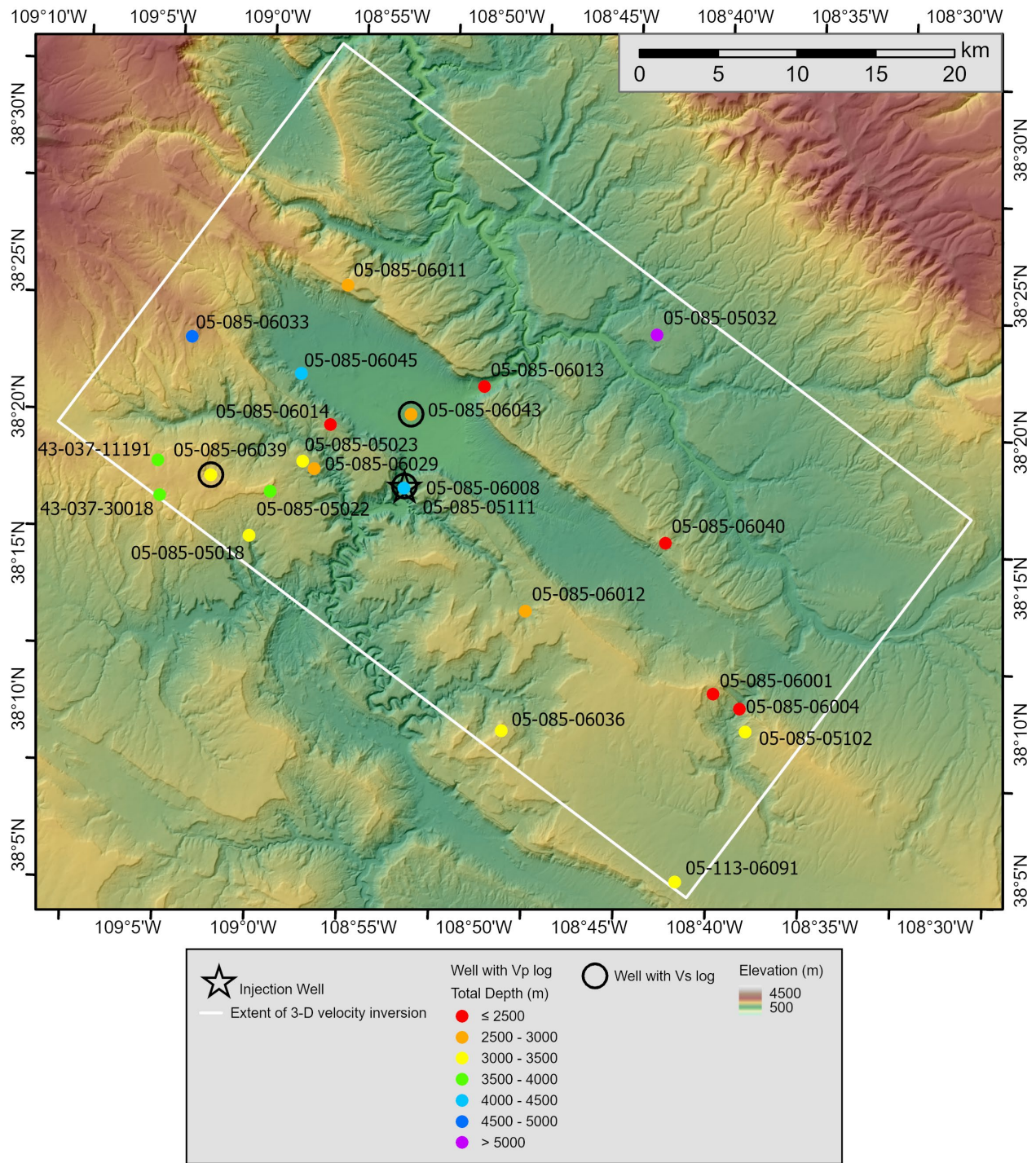


**Figure 2-5: Locations of wells within the inversion area where geophysical velocity well logs were available. Wells with P-wave velocity logs are indicated by the filled circles, which are color-coded by the total depth of the wellbore (see legend). Wells with S-wave velocity logs are indicated by open black circles. The wells are labeled with their American Petroleum Institute (API) numbers (see Table 2-2).**

(Figure 2-5). For some of the wells, the velocities are only available over a short depth section, while for others, velocities are available for nearly the entire depth range of the well (Table 2-2). Only five of the well logs extend deeper than an elevation of -2.0 km, and the deepest log extends to -3.7 km elevation. These well data were compiled during previous PVU studies and are documented more thoroughly in King (2017). The velocity values from the well logs, which are available at a 0.5-ft (0.15-m) depth interval, were smoothed using a centered moving average with a window length of 250 ft (76.20 m). The smoothed well logs were then sampled at a depth interval of 100 ft (30.48 m). Depths in feet were subsequently converted to elevations in kilometers, using the ground elevations at the wells. These point velocity values were then input into the inversion as weighted data point constraints, as described in Appendix A.

**Table 2-2: Elevation ranges of data points from smoothed velocity logs**

Well Name	API	Latitude (deg.)	Longitude (deg.)	Elevation Range of Smoothed Vp Log (km)	Elevation Range of Smoothed Vs Log (km)
WRAY MESA UNIT 3	05-085-05018	38.265	-109.006	-1.4 to 1.6	
WRAY MESA UNIT 2	05-085-05022	38.291	-108.992	-1.3 to 1.5	
WRAY MESA UNIT 1	05-085-05023	38.308	-108.969	-1.4 to -1.1	
URAVAN UNIT 1	05-085-05032	38.388	-108.716	-3.7 to 1.2	
KIRBY-GOVERNMENT 1	05-085-05102	38.176	-108.647	-0.4 to -0.2	
MONTROSE UNIT 1	05-085-06001	38.184	-108.666	-0.1 to 1.5	
MONTROSE UNIT WELL 3	05-085-06004	38.163	-108.642	1.3 to 1.9	
OTHO AYERS 1-0-30	05-085-06008	38.295	-108.895	-2.8 to 0.9	
FEDERAL SINBAD RIDGE UNIT 14-14	05-085-06011	38.410	-108.941	-0.6 to 1.1	
WILD STEER UNIT-FEDERAL 32-24	05-085-06012	38.228	-108.804	-0.9 to 0.8	
FEDERAL MARTIN MESA 33-3	05-085-06013	38.355	-108.840	-0.7 to 1.4	
FEDERAL WILD STEER UNIT 32-15	05-085-06014	38.330	-108.950	-0.4 to 1.1	
WRAY MESA 1	05-085-06029	38.305	-108.961	-0.6 to 1.3	
HAUKELID 35-1	05-085-06033	38.377	-109.053	-2.4 to 1.5	
BULL CANYON 14-14	05-085-06036	38.159	-108.818	-1.2 to 1.1	
FOSSIL FEDERAL 1-13	05-113-06091	38.076	-108.689	-1.0 to 0.9	
CIMARRON FEDERAL 25-31	05-085-06039	38.299	-109.036	-0.8 to 1.5	-0.8 to 1.5
SABERTOOTH 1-2	05-085-06040	38.269	-108.704	-0.1 to 1.4	
BEDROCK UNIT 16-7-47-18	05-085-06043	38.338	-108.892	-0.9 to 1.2	-0.9 to 1.2
BEDROCK UNIT 6-4-47-19	05-085-06045	38.359	-108.973	-2.4 to 0.7	
HORSETHIEF CANYON UNIT 1-5	43-037-11191	38.306	-109.074	-1.4 to 1.0	
HORN UNIT FED 1	43-037-30018	38.286	-109.072	-1.3 to 2.0	
PVU INJECTION WELL	05-085-05111	38.297	-108.895	-3.3 to 1.4	-3.3 to -2.8

The spatial resolution of the 3-D velocity models is low in areas with limited ray coverage from the earthquakes and explosions. Also, velocity regularization was used to smooth the velocity models, as discussed above. If the velocity well log constraints were heavily weighted, the inversion would produce small velocity anomalies at the wells to satisfy them, in areas where the velocity model otherwise has lower spatial resolution. For this reason, this constraint was only weighted enough for the velocity models to honor the broad trends of the well log data.

### **2.3.4 Explosions**

The explosions included in the inversion were constrained to occur at the local ground surface. This was implemented by: setting the initial  $z$  coordinates of all explosions to the ground elevations at their respective initial  $(x, y)$  locations; keeping the explosion  $z$  coordinates fixed during each iteration of the inversion while their  $(x, y)$  coordinates varied; and resetting the  $z$  coordinates of the explosions to the ground elevations at their new  $(x, y)$  locations after each iteration of the inversion. The ground elevations were taken from a topography file with a node spacing of 72.3-73.8 m longitude, 92.5-92.6 m latitude, and 1 m elevation.

### **2.3.5 P-wave Station Correction Sum**

When all station corrections are allowed to vary, they can trade off with the hypocenter origin times. All earthquake origin times and all station corrections for one phase (either P-wave or S-wave) could shift by the same amount, and the arrival time residuals would be unchanged. To eliminate this trade-off, the sum of the P-wave station corrections was required to be zero.

## **2.4 Inversion Procedure**

Inversions were performed in multiple stages, to ultimately determine 3-D P-wave and S-wave velocity models, station corrections, and corresponding hypocenters. Each stage started with the result (hypocenters, stations corrections, velocity model) from the end of the previous stage. As the stages progressed, more parameters were allowed to vary. Velocity models were allowed to become more spatially variable by changing the velocity node spacing and decreasing the velocity regularization weighting. For the initial inversions, large arrival time residuals do not necessarily indicate errors in the data but rather likely represent signals of velocity anomalies. For this reason, the initial inversions were performed using an L2 norm. An L1 norm was used during the last set of inversions, to reduce the likelihood of modeling errors in the data.

The stages of the inversion procedure were:

1. Compute hypocenters of the earthquakes and explosions with the starting velocity model fixed and all station corrections fixed at 0.
2. With the starting velocity model fixed, allow hypocenters and all station corrections to vary.

3. Allow hypocenters, station corrections, and 1-D P-wave and S-wave velocities to vary. During this stage, the velocities were only allowed to vary in the vertical direction. Hence, this inversion determined the best-fitting P-wave and S-wave velocity-depth profiles. The node spacing in the vertical direction was the same as the starting velocity model (Table 2-1), and velocities below -20 km elevation were fixed (because only two earthquakes below that elevation are available in the dataset; Figure 2-2). Two inversions were performed, with strong velocity regularization weighting in the first inversion and less velocity regularization in the second.
4. Allow hypocenters, station corrections, and 3-D P-wave and S-wave velocities to vary, using a coarse velocity node model. The velocity node spacing was 5 km in the  $x$  (northeast) direction and 10 km in the  $y$  (northwest) direction (Figure 2-6, open black circles). The node spacing in the vertical direction was the same as in stage 3, and velocities below -15 km elevation were fixed. Four inversions were performed. The initial inversion used a horizontal-to-vertical velocity regularization weight ratio of 10 (i.e., the velocities were allowed to vary more vertically than horizontally). This weighting was subsequently decreased to 5, and then to 3, and finally to 1 for a fully 3-D velocity model. For the last two inversions, the velocities below -10 km elevation were fixed because deep ray path coverage is limited.
5. Allow hypocenters, station corrections, and 3-D P-wave and S-wave velocities to vary, using a finer node model. The final velocity model from stage 4 was interpolated onto a grid with a node spacing of 2.5 km in the  $x$  direction and 5 km in the  $y$  direction. Velocities were only allowed to vary over the region with the better ray coverage (Figure 2-6, magenta plus symbols). Velocities below -5 km elevation were fixed. Multiple inversions were performed. Initial inversions used stronger velocity regularization weighting, and later inversions used less weighting. An L2 norm was used for the first two inversions, and subsequent inversions used an L1 norm. In addition, the lateral and vertical extent of the area where velocities were allowed to vary decreased as the inversions progressed, based on ray coverage and the location of the low-velocity anomaly beneath Paradox Valley.

Additional inversions were performed with even finer node spacing, to see if they would allow for better spatial resolution of the low-velocity anomaly beneath Paradox Valley. These inversions did not provide better fits to the arrival time data nor substantially different velocity models. Hence, these models were discarded.



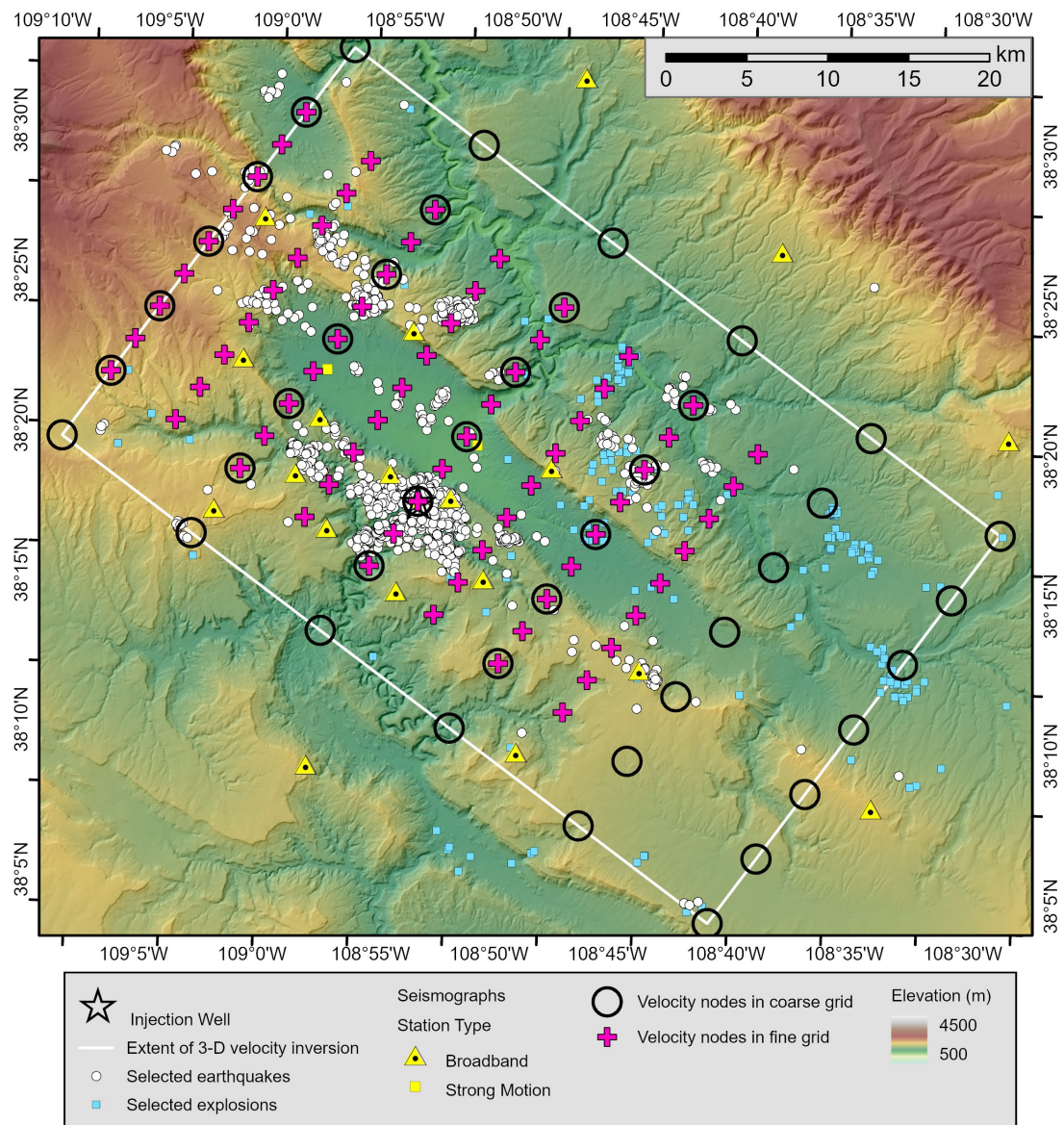


**Figure 2-6: Locations of velocity nodes in the initial coarse grid (open black circles) and the final finer grid (magenta plus symbols) used for the 3-D hypocenter-velocity inversions. For the fine grid, only the velocity nodes that were allowed to vary during the inversions are shown. The locations of the seismic stations and earthquakes and explosions used in the inversions are included for reference.**

## 3.0 Results

### 3.1 Arrival Time Residuals

Arrival time residuals decreased during each stage of the progressive inversion procedure described above (section 2.4). Histograms of the P-wave and S-wave arrival time residuals for the final models from the five stages of the progressive inversions are presented in Figure 3-1. The corresponding mean absolute residuals are listed in Table 3-1. Large decreases in residuals were observed when station corrections were used with the starting velocity model (inversion stage 1 to stage 2). The mean absolute P-wave and S-wave residuals decreased 42.3% and 36.0%, respectively (Table 3-1), and the residual histograms became much less skewed (Figure 3-1, dashed black lines to dashed-and-double-dotted green lines). Relatively little additional improvement was observed when going from the 1-D starting velocity model to the final best-fitting 1-D velocity model (stage 2 to stage 3), although the S-wave residual histogram did become more zero-mean (Figure 3-1b, dashed-and-double-dotted green line to dashed-and-single-dotted blue line). The mean absolute P-wave residual decreased only 1.3%, while the mean absolute S-wave residual decreased 7.4% (Table 3-1). Substantial improvement was again observed when velocities were allowed to vary in 3-D using a coarse grid of nodes (stage 3 to stage 4). The mean absolute P-wave and S-wave residuals decreased 15.4% and 27.7%, respectively (Table 3-1). The residual histograms became narrower, most noticeably for the S-wave data, indicating a decrease in the residual standard deviations (Figure 3-1, dashed-and-single-dotted blue lines to dashed red lines). A modest additional improvement in the fit to the data was obtained with the 3-D velocity model with the finer node spacing (stage four to stage five). P-wave and S-wave mean absolute residuals decreased an additional 6.1% and 3.7%, respectively (Table 3-1).



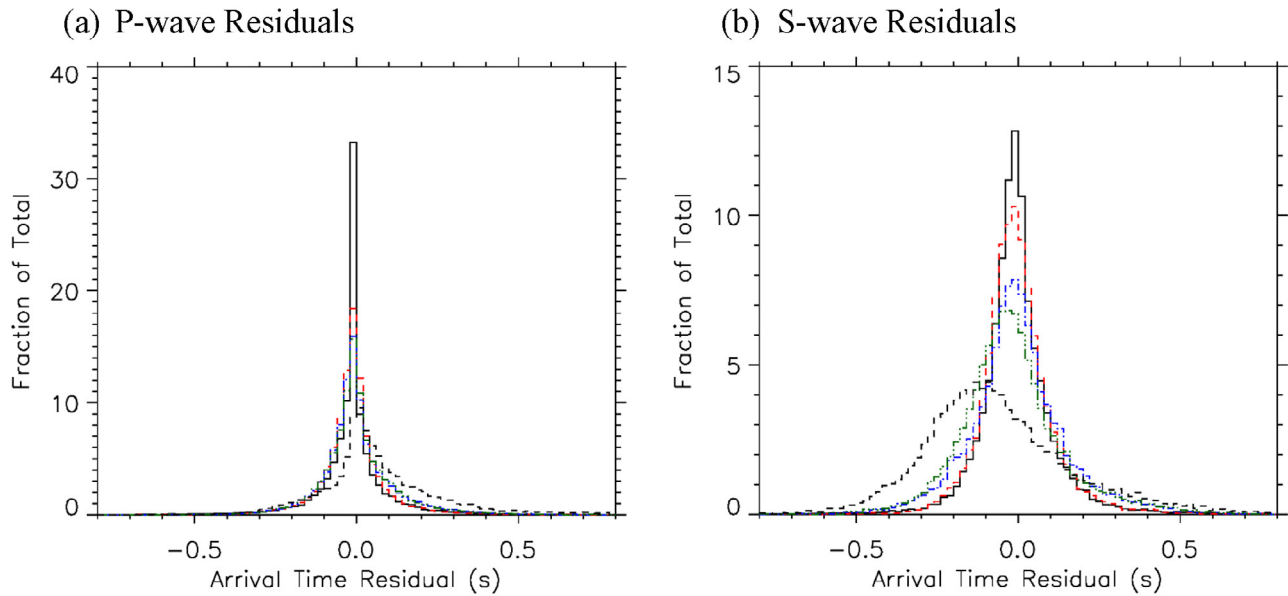


**Figure 3-1: (a) P-wave and (b) S-wave arrival time residuals of events located in the final models from the five stages of the progressive inversions: 1. starting velocity model without station corrections (dashed black lines), 2. starting velocity model with station corrections (dashed and double-dotted green lines), 3. final 1-D velocity model (dashed and single-dotted blue lines), 4. 3-D velocity model with coarse grid (dashed red lines), and 5. final 3-D velocity model with fine grid (solid black lines).**

**Table 3-1: P-wave and S-wave arrival time residuals for the five progressive models**

Inversion Stage	Model	Mean Absolute P-wave Residual (s)	Change from Previous Stage	Mean Absolute S-wave Residual (s)	Change from Previous Stage
1	Starting velocity model and no station corrections	0.137		0.189	
2	Starting velocity model with station corrections	0.079	-42.3%	0.121	-36.0%
3	Final 1-D velocity model and corresponding station corrections	0.078	-1.3%	0.112	-7.4%
4	3-D velocity model with coarse grid and corresponding station corrections	0.066	-15.4%	0.081	-27.7%
5	Final 3-D velocity model with fine grid and corresponding station corrections	0.062	-6.1%	0.078	-3.7%

## 3.2 Station Corrections

The corresponding station corrections for the best-fitting 1-D velocity model and the best-fitting 3-D velocity model with the fine node spacing are listed in Table 3-2 and Table 3-3, respectively. (There are no S-wave corrections for stations PV06, PV08, and PV09 because these sites hosted vertically oriented single-component seismometers, and only S-wave arrival times determined from horizontal seismometer components were included in the inversions.) Station corrections are both positive and negative, and their absolute values range from nearly zero up to about 0.8 s.

**Table 3-2: Station corrections for the final 1-D velocity model**

Station	P-wave Correction (s)	S-wave Correction (s)	Station	P-wave Correction (s)	S-wave Correction (s)
PV01	-0.286	-0.297	PV14	-0.056	0.031
PV02	-0.120	-0.058	PV15	-0.106	-0.117
PV03	-0.067	0.050	PV16	0.073	0.252
PV04	0.237	0.576	PV17	-0.022	0.064
PV05	0.004	-0.117	PV18	-0.043	0.035
PV06	-0.004		PV19	-0.011	0.108
PV07	0.012	0.175	PV20	0.021	0.249
PV08	-0.266		PV21	0.060	0.199
PV09	0.138		PV22	0.038	0.120
PV10	0.027	0.124	PV23	0.111	0.435
PV11	0.067	0.297	PVPP	-0.011	0.130
PV12	0.174	0.443	PVEF	0.098	0.368
PV13	-0.100	-0.113	PVCC	0.033	0.236

**Table 3-3: Station corrections for the final 3-D velocity model**

Station	P-wave Correction (s)	S-wave Correction (s)	Station	P-wave Correction (s)	S-wave Correction (s)
PV01	-0.546	-0.489	PV14	-0.009	-0.171
PV02	0.189	0.176	PV15	-0.579	-0.453
PV03	0.297	0.37	PV16	0.354	0.463
PV04	0.237	0.181	PV17	0.225	0.247
PV05	-0.001	-0.093	PV18	0.254	0.307
PV06	-0.429		PV19	0.191	0.205
PV07	-0.121	-0.11	PV20	0.188	0.29
PV08	-0.804		PV21	-0.244	-0.394
PV09	-0.269		PV22	-0.229	-0.296
PV10	0.059	0.014	PV23	-0.09	-0.162
PV11	0.377	0.583	PVPP	0.292	0.417
PV12	0.331	0.318	PVEF	0.293	0.425
PV13	0.108	0.165	PVCC	0.082	0.048

### 3.3 Velocities

The node values of the final 1-D velocity model are listed in Table 3-4. Only the nodes at and above -20 km elevation are included since the velocities of the deeper nodes were fixed at their starting values (Table 2-1). P-wave and S-wave velocity profiles of the final model are compared to those of the starting model in Figure 3-2. The velocity profiles changed slightly, with the profiles becoming smoother and the shallowest velocities becoming somewhat higher.

**Table 3-4: Final 1-D velocity model**

Elevation (km)	Vp (km/s)	Vs (km/s)
1	5.13	2.96
0	5.37	3.04
-1	5.63	3.15
-2	5.84	3.28
-3	5.96	3.39
-5	5.98	3.46
-10	6.05	3.56
-15	6.14	3.58
-20	6.23	3.62

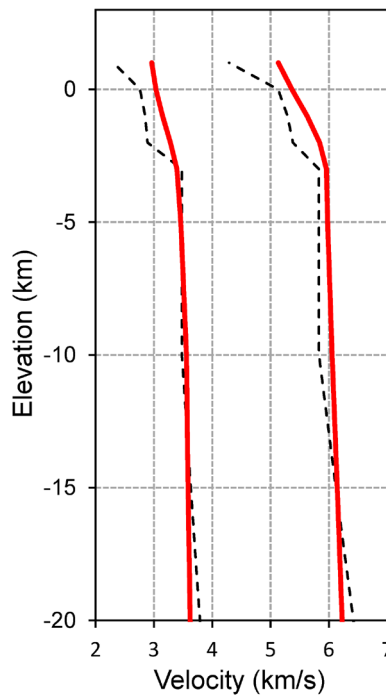


**Figure 3-2: Initial (dashed black curves) and final (solid red curves) 1-D P-wave and S-wave velocity models.**

Horizontal P-wave and S-wave velocity sections through the final 3-D model (with the finer node spacing) are presented in Figure 3-3 through Figure 3-9. The elevations of these sections range from 1 km (Figure 3-3) to -5 km (Figure 3-9). (Below -5 km elevation, there is little horizontal velocity variation.) The local topography, PVU injection well, and PVSN seismic stations are included on the plots for reference.

The strongest features of the 3-D velocity model are the low-velocity anomalies beneath Paradox Valley. These anomalies correspond to the salt anticline that underlies the valley. Both P-wave and S-wave velocities are relatively low in the area of this salt anticline, by roughly 15% to 25% compared to the surrounding areas. The low velocities are observed along most of the extent of Paradox Valley from the shallowest section at 1 km elevation to the section at an elevation of -1 km (Figure 3-3 to Figure 3-5). The low velocities persist at the northern end of Paradox Valley down to an elevation of -2 km (Figure 3-6), and small remnants at the northernmost end of the valley are seen at -3 km elevation (Figure 3-7). The low-velocity anomalies are also generally wider at the northern end of the valley than at the southern end, which mimics the widening of the valley topographically at the northern end.

The low-velocity anomaly beneath Paradox Valley can also be seen on a series of vertical cross sections perpendicular and parallel to the valley, which are presented in Figure 3-11 to Figure 3-14. The locations of these section lines are shown on the maps in Figure 3-10. The low-velocity anomaly beneath Paradox Valley is seen in the upper-central part of sections A-A', B-B', C-C', D-D', and E-E' perpendicular to the valley, with the anomaly becoming narrower on the more southern sections (Figure 3-11 and Figure 3-12). The low-velocity anomaly beneath Paradox Valley is seen in the upper right (northern) parts of sections K-K', L-L', and M-M' parallel to the valley (Figure 3-13 and Figure 3-14). These sections show the anomaly extending slightly deeper at the more northern end of Paradox Valley.

The earthquake hypocenters projected onto the vertical cross sections show that the earthquakes in the Paradox Valley area occur beneath or around the low-velocity anomaly underlying the valley but not in it. The vertical sections perpendicular to Paradox Valley are spaced 5 km apart, and hypocenters within 2.5 km of the sections are projected into them (Figure 3-11 and Figure 3-12). The vertical sections parallel to Paradox Valley are spaced 3 km apart, and hypocenters within 1.5 km of the sections are projected into them (Figure 3-13 and Figure 3-14). The hypocenters shown are those from the final 3-D hypocenter-velocity inversion. The fact that hypocenters do not occur within the low-velocity anomaly beneath Paradox Valley is consistent with the interpretation that this anomaly represents the Paradox salt. Since this salt has high plasticity, it is not expected to support brittle deformation that would generate earthquakes.

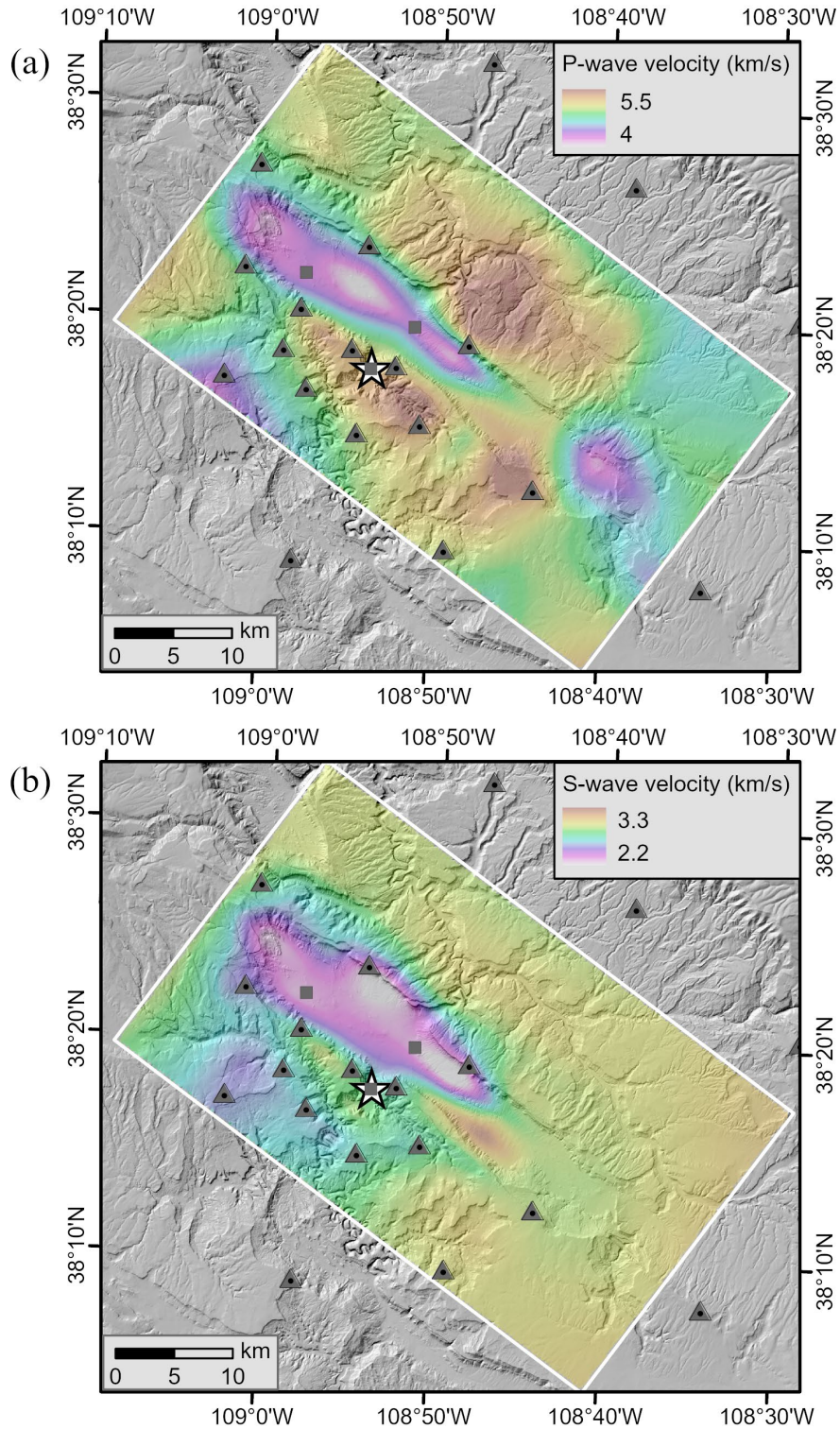


**Figure 3-3: (a) P-wave velocity and (b) S-wave velocity horizontal section through the final 3-D model at 1 km elevation. The white star is the location of the PVU injection well. The gray triangles are the locations of the broadband seismic stations, and the gray squares are the locations of the strong motion stations.**



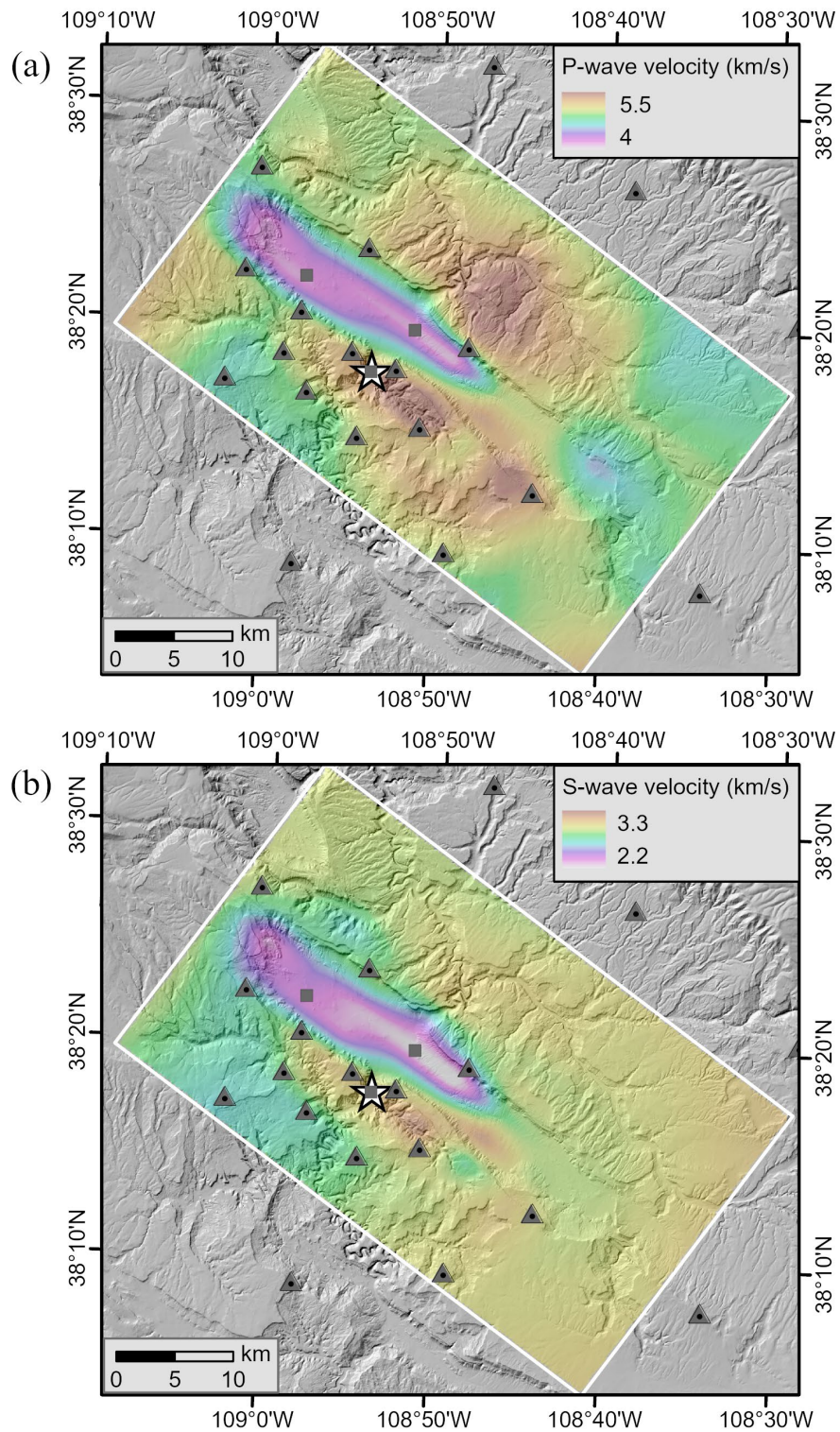


**Figure 3-4: (a) P-wave velocity and (b) S-wave velocity horizontal section through the final 3-D model at 0 km elevation. The white star is the location of the PVU injection well. The gray triangles are the locations of the broadband seismic stations, and the gray squares are the locations of the strong motion stations.**

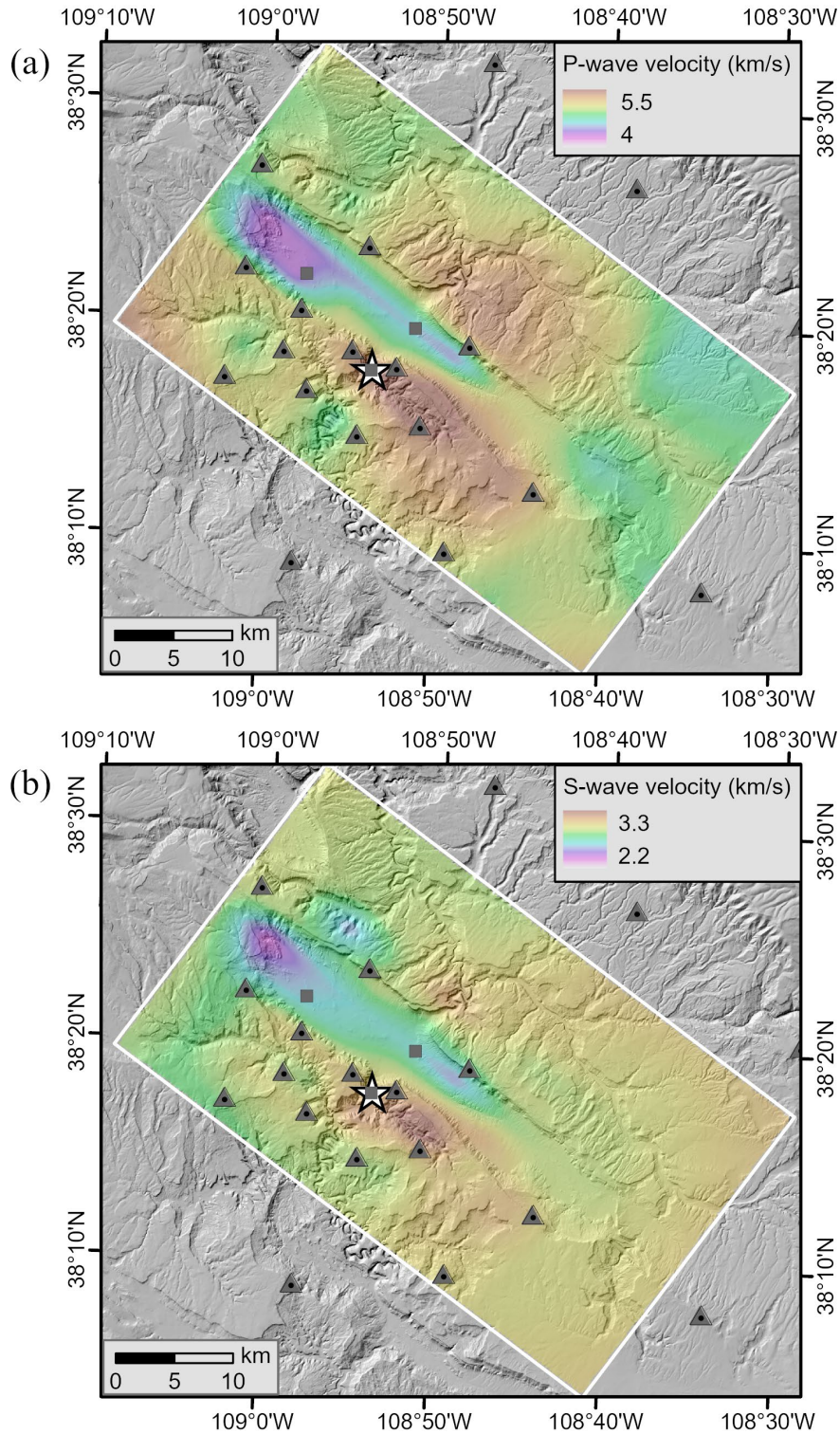


**Figure 3-5: (a) P-wave velocity and (b) S-wave velocity horizontal section through the final 3-D model at -1 km elevation. The white star is the location of the PVU injection well. The gray triangles are the locations of the broadband seismic stations, and the gray squares are the locations of the strong motion stations.**



Technical Memorandum 86-68330-2024-7  
Development of a New Velocity Model for the Paradox Valley Area

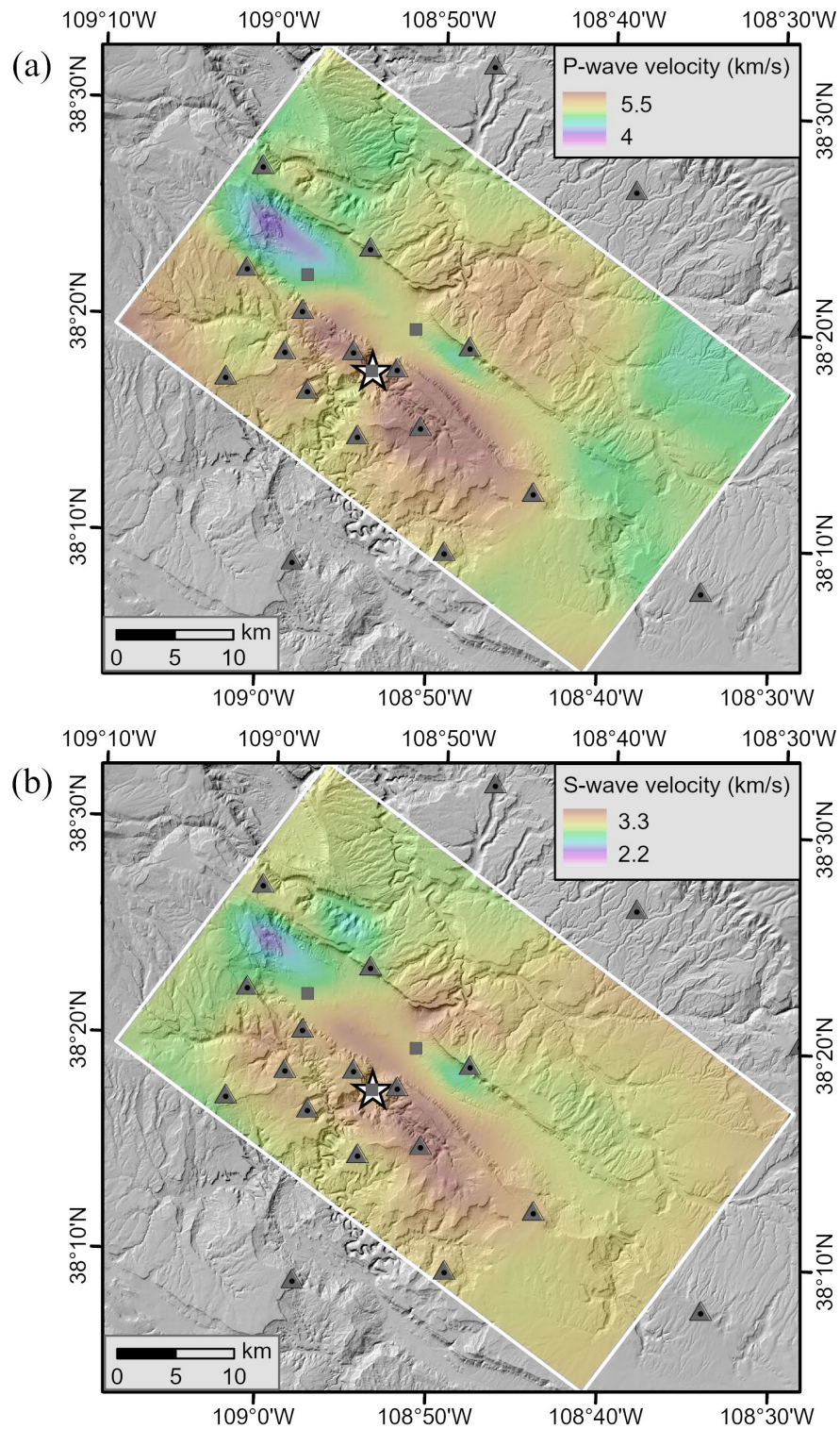


**Figure 3-6: (a) P-wave velocity and (b) S-wave velocity horizontal section through the final 3-D model at -2 km elevation. The white star is the location of the PVU injection well. The gray triangles are the locations of the broadband seismic stations, and the gray squares are the locations of the strong motion stations.**



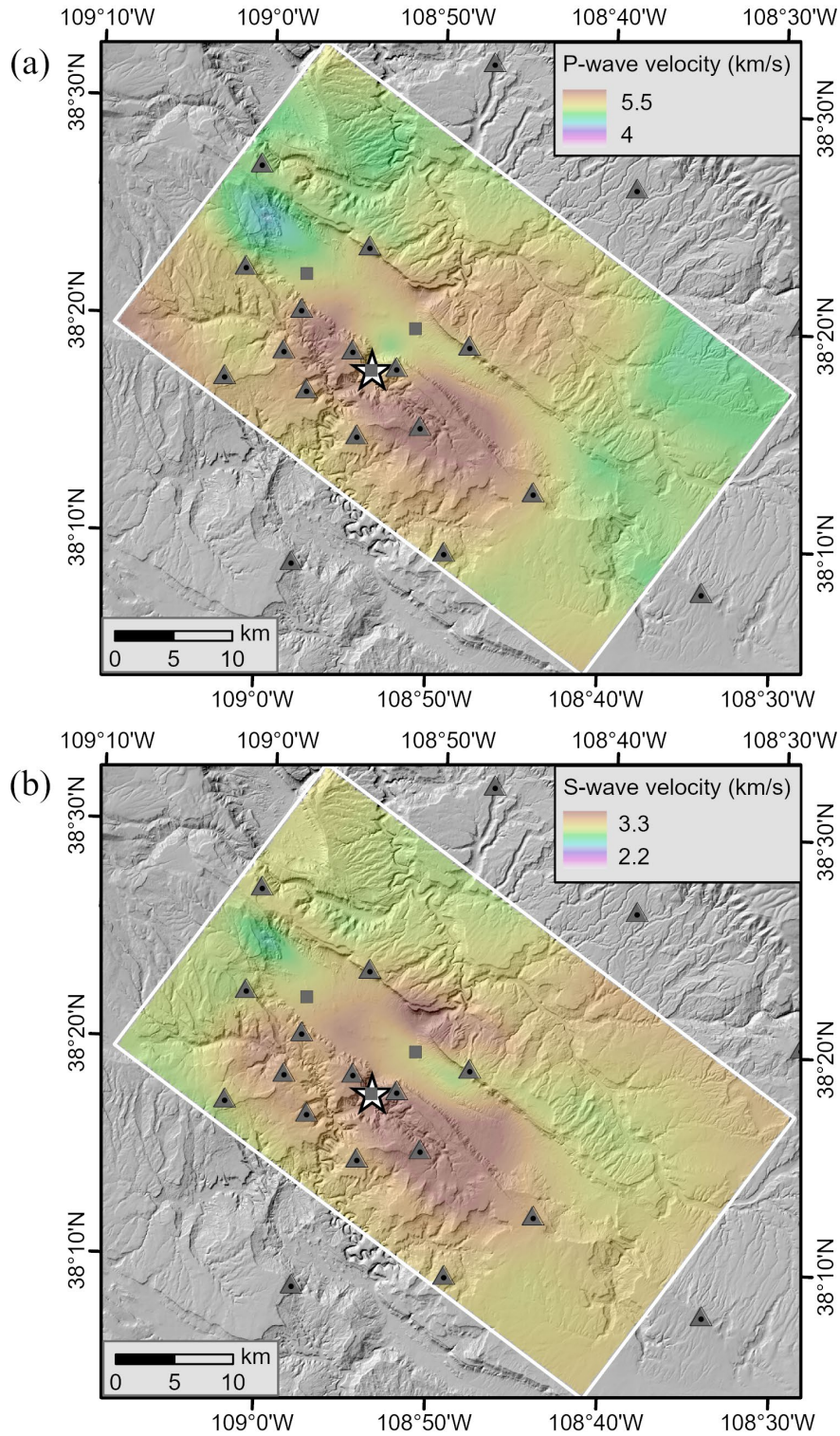
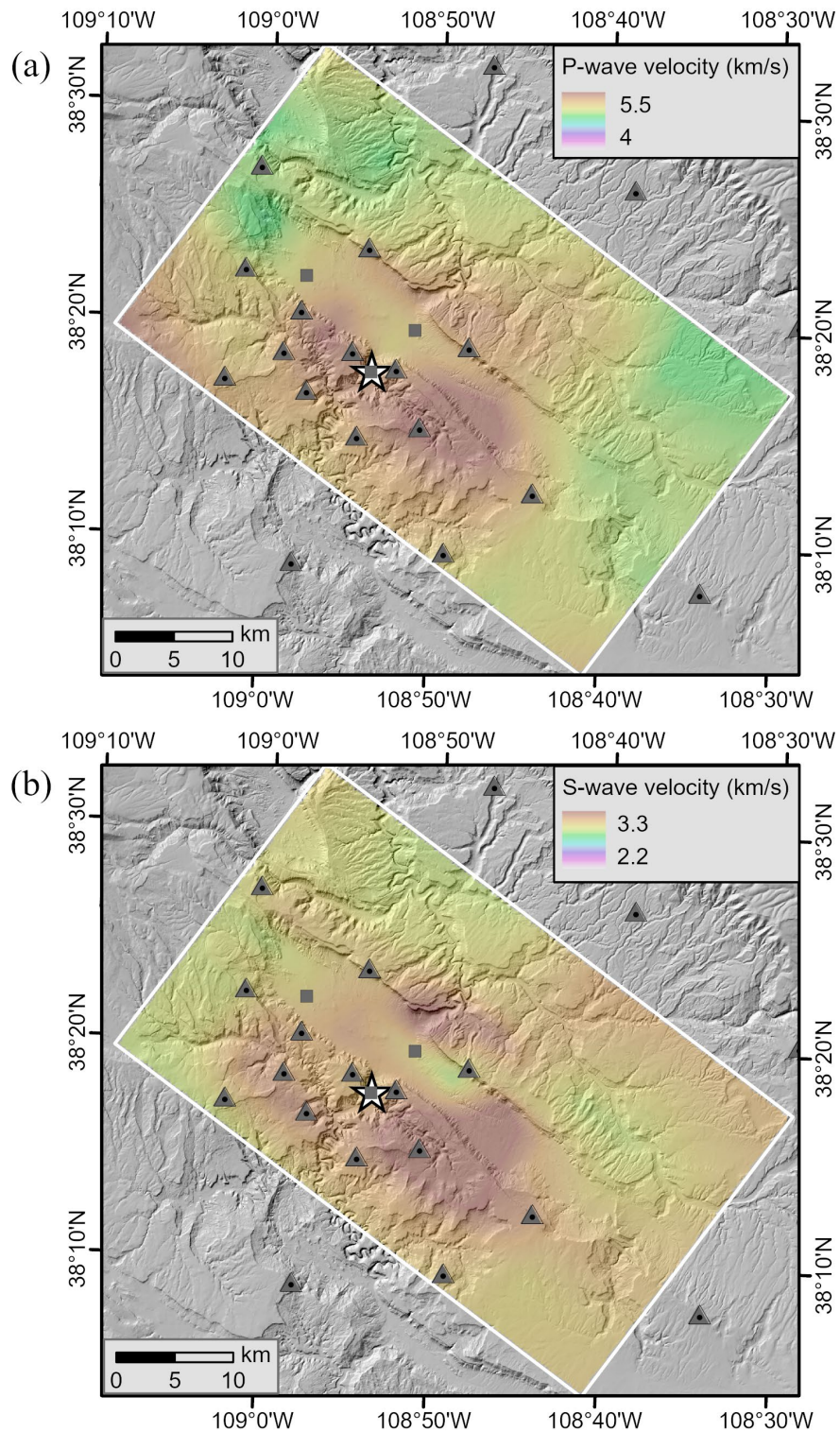


Figure 3-7: (a) P-wave velocity and (b) S-wave velocity horizontal section through the final 3-D model at -3 km elevation. The white star is the location of the PVU injection well. The gray triangles are the locations of the broadband seismic stations, and the gray squares are the locations of the strong motion stations.

Technical Memorandum 86-68330-2024-7  
Development of a New Velocity Model for the Paradox Valley Area



**Figure 3-8: (a) P-wave velocity and (b) S-wave velocity horizontal section through the final 3-D model at -4 km elevation. The white star is the location of the PVU injection well. The gray triangles are the locations of the broadband seismic stations, and the gray squares are the locations of the strong motion stations.**



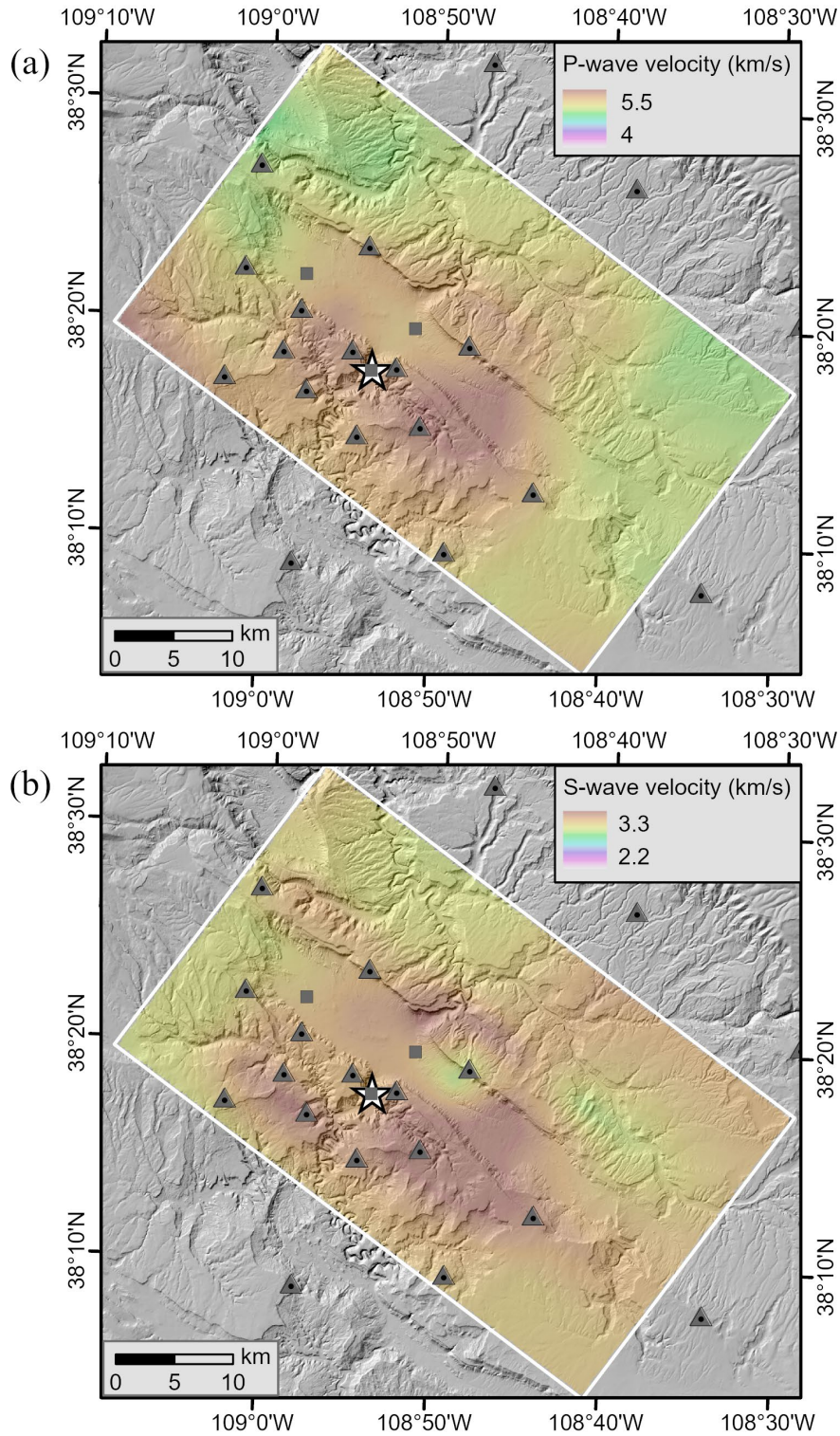
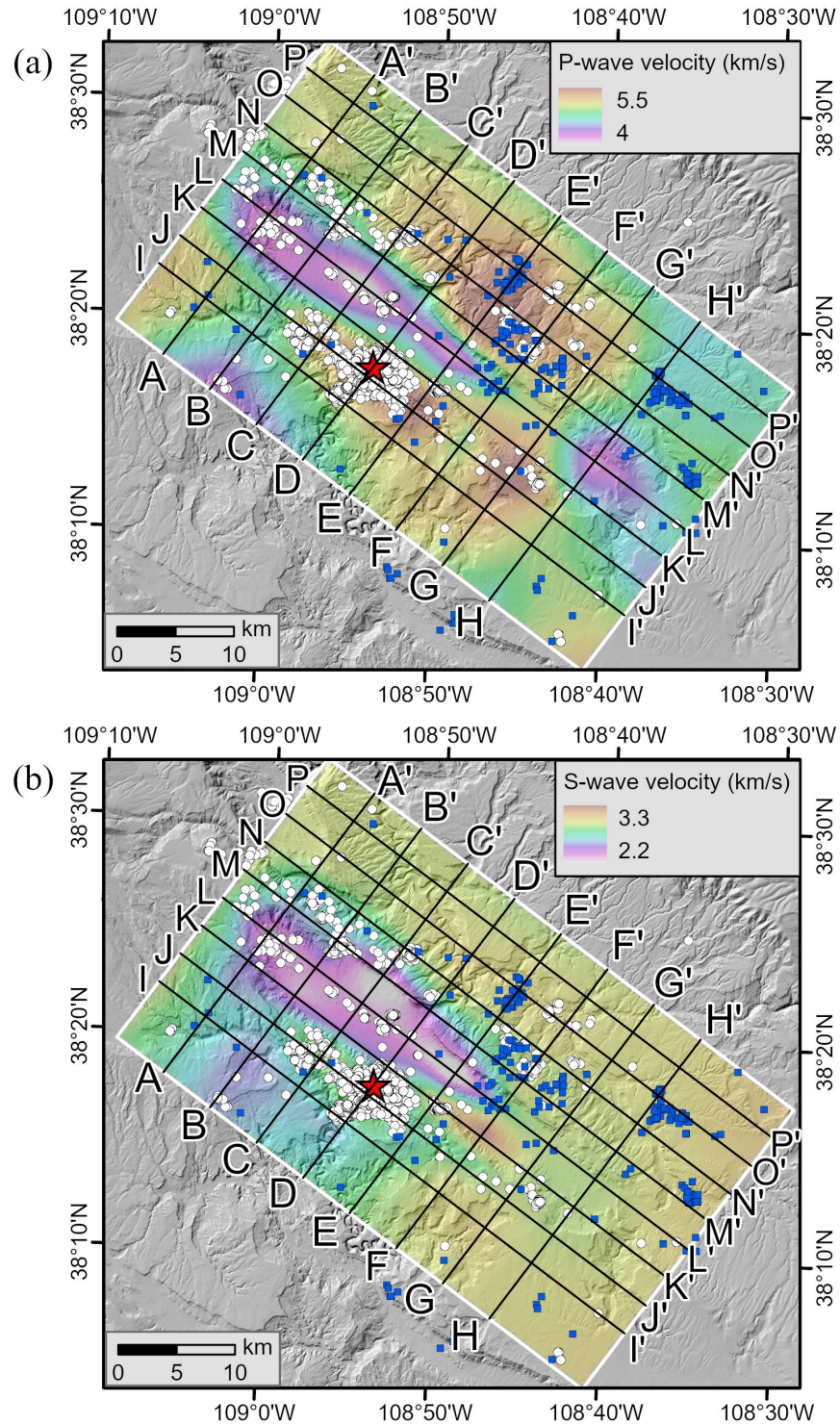
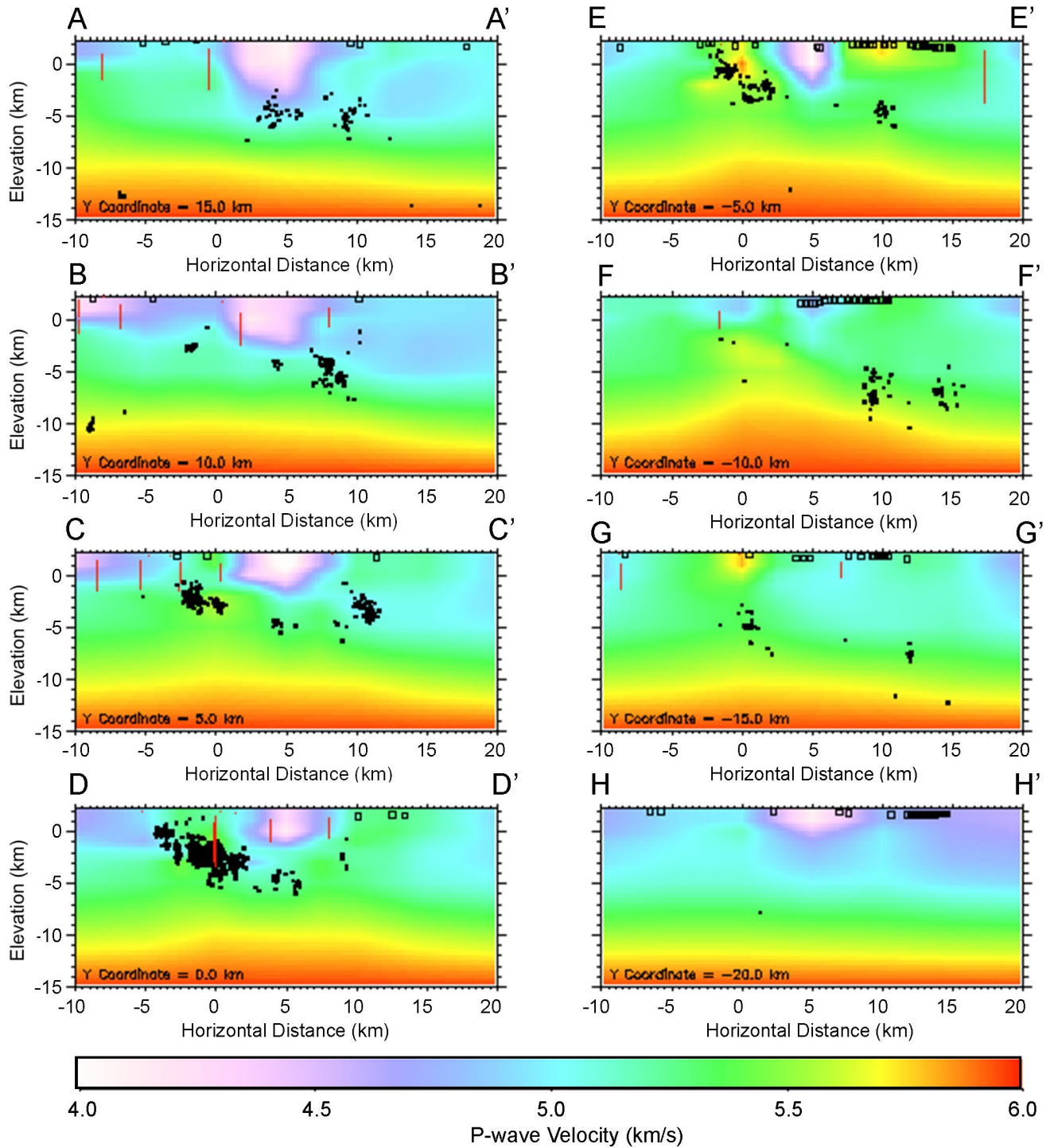


Figure 3-9: (a) P-wave velocity and (b) S-wave velocity horizontal section through the final 3-D model at -5 km elevation. The white star is the location of the PVU injection well. The gray triangles are the locations of the broadband seismic stations, and the gray squares are the locations of the strong motion stations.



**Figure 3-10: Locations of vertical cross sections presented in Figure 3-11 to Figure 3-14. For reference, the final locations of the earthquakes used in the hypocenter-velocity inversions (filled white circles), the final locations of the explosions (filled dark blue squares), and the velocity sections through the final 3-D P-wave (a) and S-wave (b) velocity models at 1 km elevation are shown.**





**Figure 3-11: Vertical sections perpendicular to Paradox Valley through the final 3-D P-wave velocity model. The cross sections are spaced 5 km apart; their locations are shown in Figure 3-10. The earthquakes (black dots), explosions (open black squares), and well log data points (red lines) within 2.5 km of each section are projected onto the sections.**

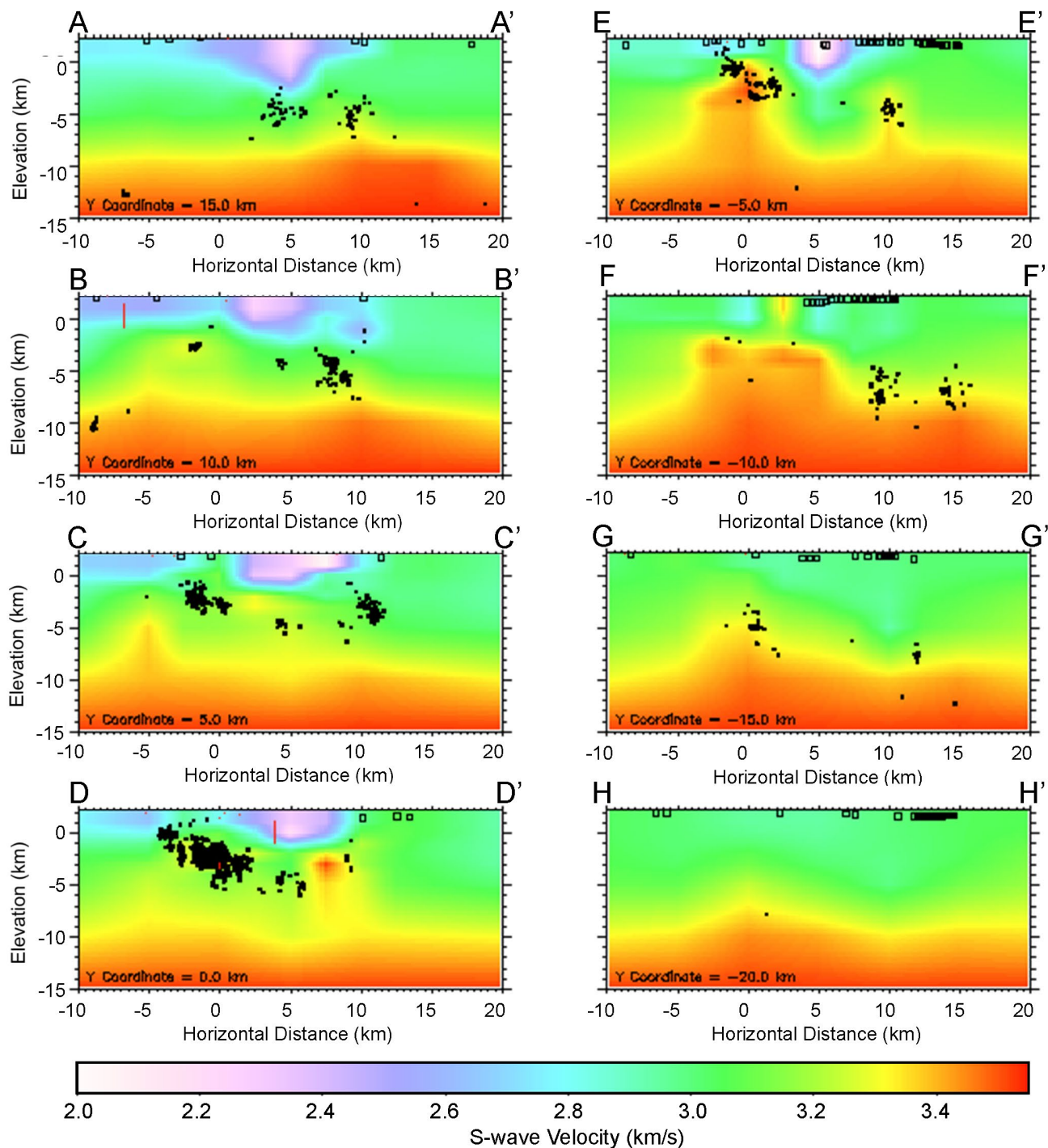


**Figure 3-12: Vertical sections perpendicular to Paradox Valley through the final 3-D S-wave velocity model. The cross sections are spaced 5 km apart; their locations are shown in Figure 3-10. The earthquakes (black dots), explosions (open black squares), and well log data points (red lines) within 2.5 km of each section are projected onto the sections.**

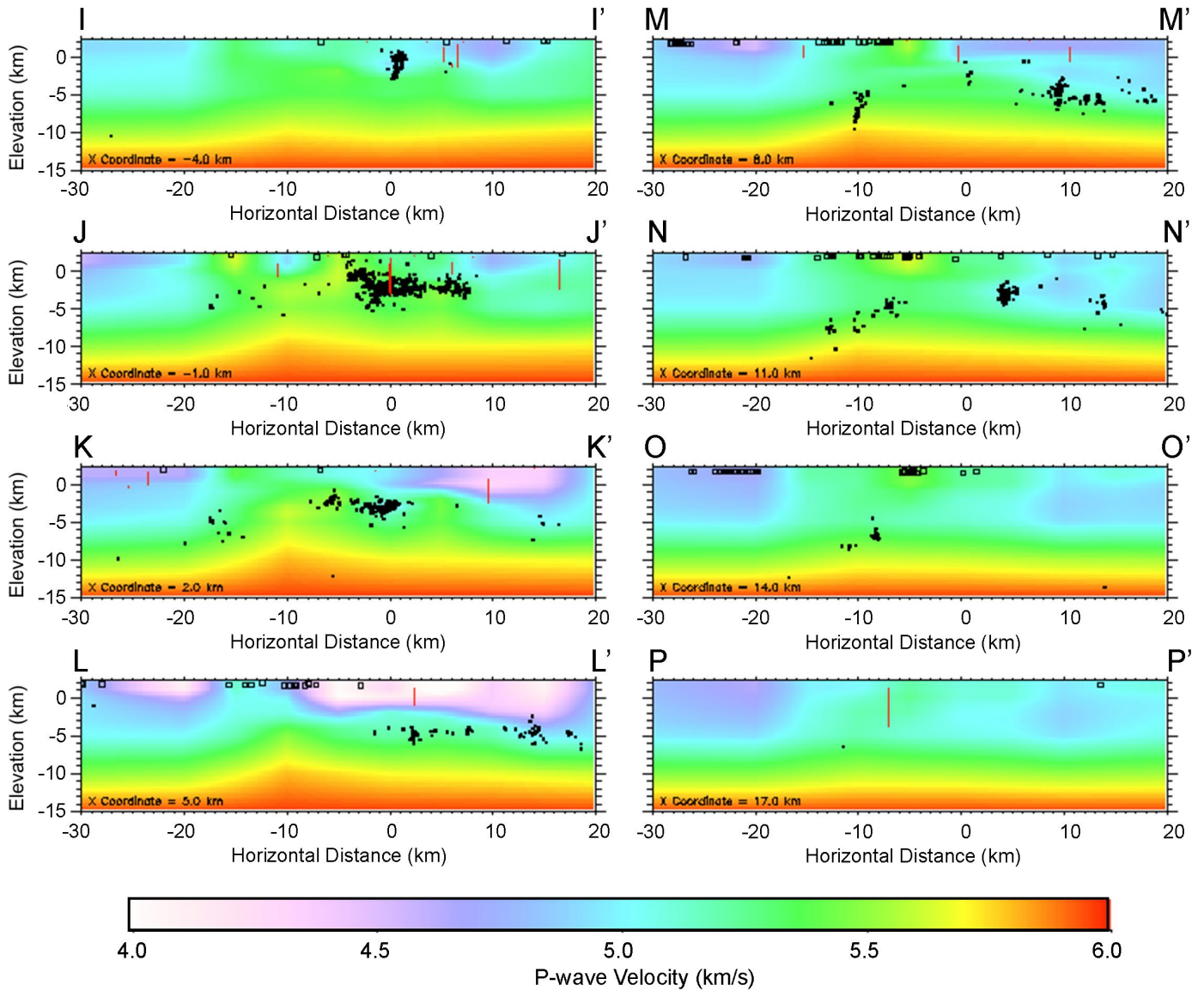


**Figure 3-13: Vertical sections parallel to Paradox Valley through the final 3-D P-wave velocity model. The cross sections are spaced 3 km apart; their locations are shown in Figure 3-10. The earthquakes (black dots), explosions (open black squares), and well log data points (red lines) within 1.5 km of each section are projected onto the sections.**



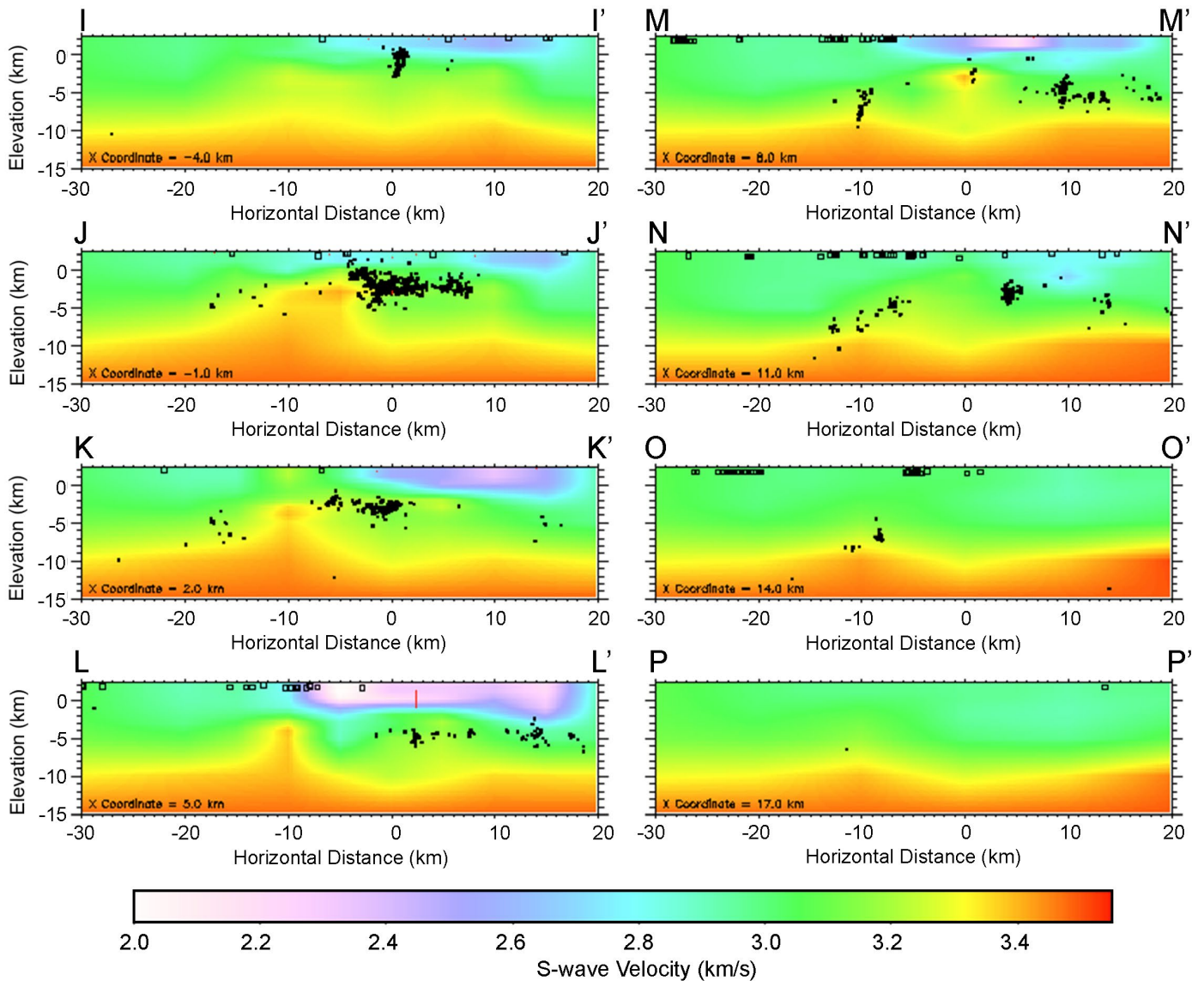


**Figure 3-14: Vertical sections parallel to Paradox Valley through the final 3-D S-wave velocity model. The cross sections are spaced 3 km apart; their locations are shown in Figure 3-10. The earthquakes (black dots), explosions (open black squares), and well log data points (red lines) within 1.5 km of each section are projected onto the sections.**



Information from two wells within northern Paradox Valley that penetrated into the Leadville formation provide constraints on the thickness of the overlying relatively low-velocity Paradox, Molas, and Pinkerton Trail formations (Figure 1-3). These wells are the Scrup Somerville Wilcox 1 well (API no. 05-085-05027) and the Bedrock Unit 6-4-47-19 well (API no. 05-085-06045). The location of the Bedrock Unit well is included in Figure 2-5. Because the Scrup Somerville well did not have a velocity well log to provide constraints for the inversions, its location is not included on the map in Figure 2-5. However, it is extremely close to the well shown on the map with API 05-085-06043 (Figure 2-5). The Leadville formation was encountered at a depth of 15,000 ft, or 4572 m, in the Scrup Somerville well (King, 2017). Taking into account the ground elevation at the well (1544 m), this corresponds to an elevation of  $\sim -3.0$  km. The Bedrock Unit well encountered the top of the Leadville formation at a depth of 13,816 ft, or 4211 m (King, 2017). Taking into account the ground elevation at the Bedrock Unit well (1626 m), this corresponds to an elevation of  $\sim -2.6$  km. The bottom elevation of the relatively low-velocity Paradox salt anticline and underlying Molas and Pinkerton Trail formations from the lithology data of these two wells ( $-2.6$  to  $-3.0$  km) is consistent with the elevation range of the low-velocity anomalies, which largely fade out between  $-2.0$  and  $-3.0$  km elevation (Figure 3-6 and Figure 3-7).

Comparisons between the well log velocities and the velocities along these wellbores from the final 3-D velocity model are presented in Figure 3-15. Except for the shallowest velocities, which can trade off with station corrections, the velocities from the model are generally consistent with observed trends in the velocity well logs. Because the velocity model resolution is limited by the ray coverage from the earthquakes and explosions and by the velocity regularization constraint, the model cannot match the smaller-scale details of the well logs.

### 3.4 Ray Coverage and Model Resolution

No formal resolution analyses, such as computation of resolution matrices and standard errors or checkerboard tests, were performed. However, to inform the relative resolution in different geographical areas, ray coverage parameters were computed. These parameters include: the number of rays, the maximum gap in horizontal angular (azimuthal) ray coverage, and the maximum gap in vertical angular ray coverage. These parameters were computed independently for the P-wave and S-wave ray coverage. Horizontal and vertical sections through the 3-D grid of ray coverage parameters are included in Appendix B.

The plots of the ray coverage parameters indicate that the model resolution is best in the northwestern two-thirds of the inversion area, at elevations above  $\sim -7$  km. Ray densities are high in the northwestern two-thirds of the inversion area and are substantially sparser in the southeastern part of the inversion area. Ray density is high above about  $-5$  to  $-7$  km elevation and much sparser at greater depths. The azimuthal ray coverage is very good (i.e., the maximum gaps in horizontal angular ray coverage are relatively small) throughout most of the inversion area at elevations between 0 km and  $\sim -7$  to  $\sim -8$  km, due to the good distribution of seismic stations. The maximum gaps in horizontal angular ray coverage are  $< 90^\circ$  in half or more of the inversion area down to  $-10$  km elevation (even though the numbers of ray paths are relatively

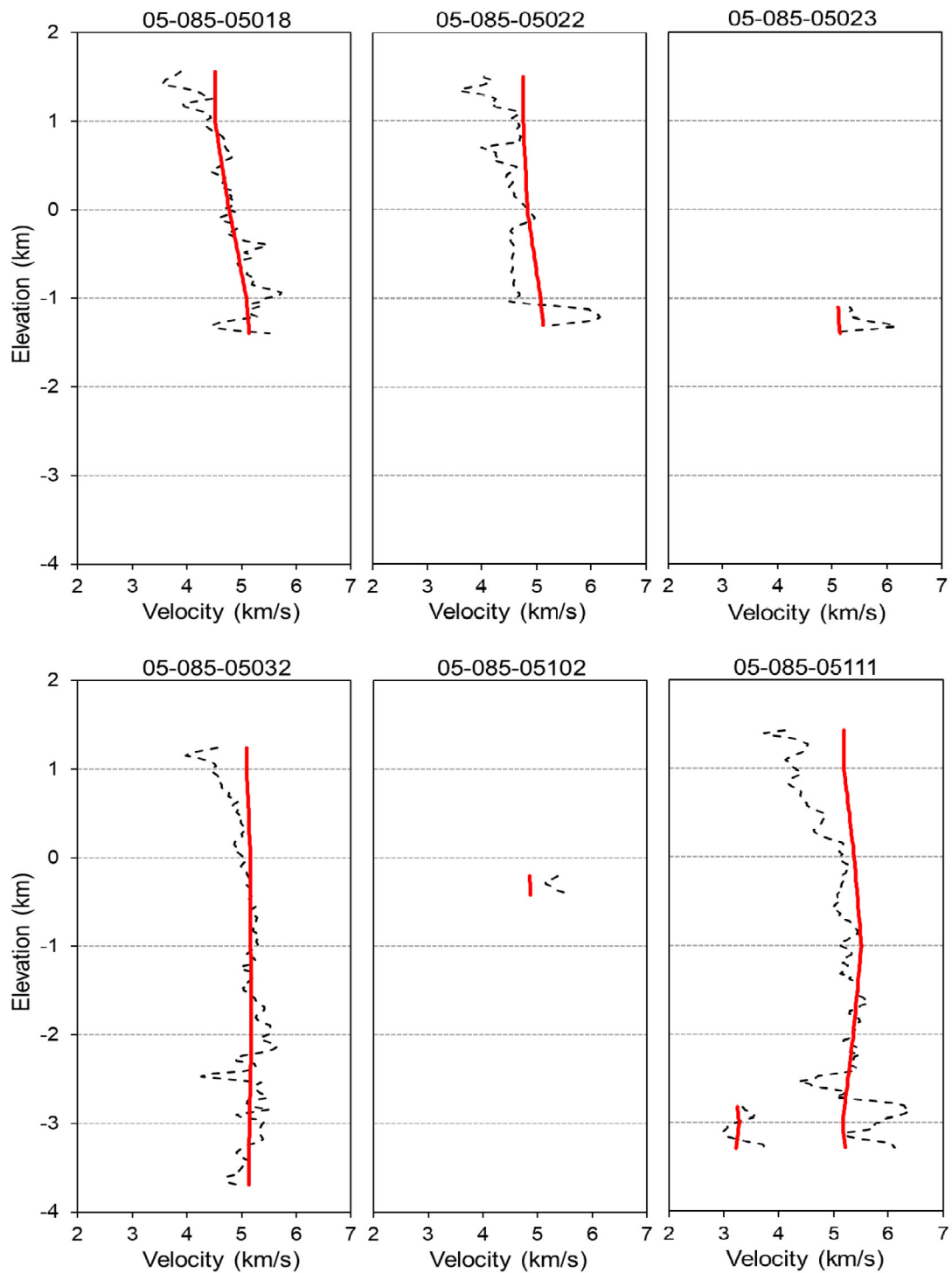


**Figure 3-15: Velocity well logs (dashed black lines) compared to the final 3-D model velocities (solid red lines). The API number of each well log is given in the plot title. Single well logs are Vp logs. For the three wells that have both Vp and Vs logs, both well logs are shown on the same plot.**

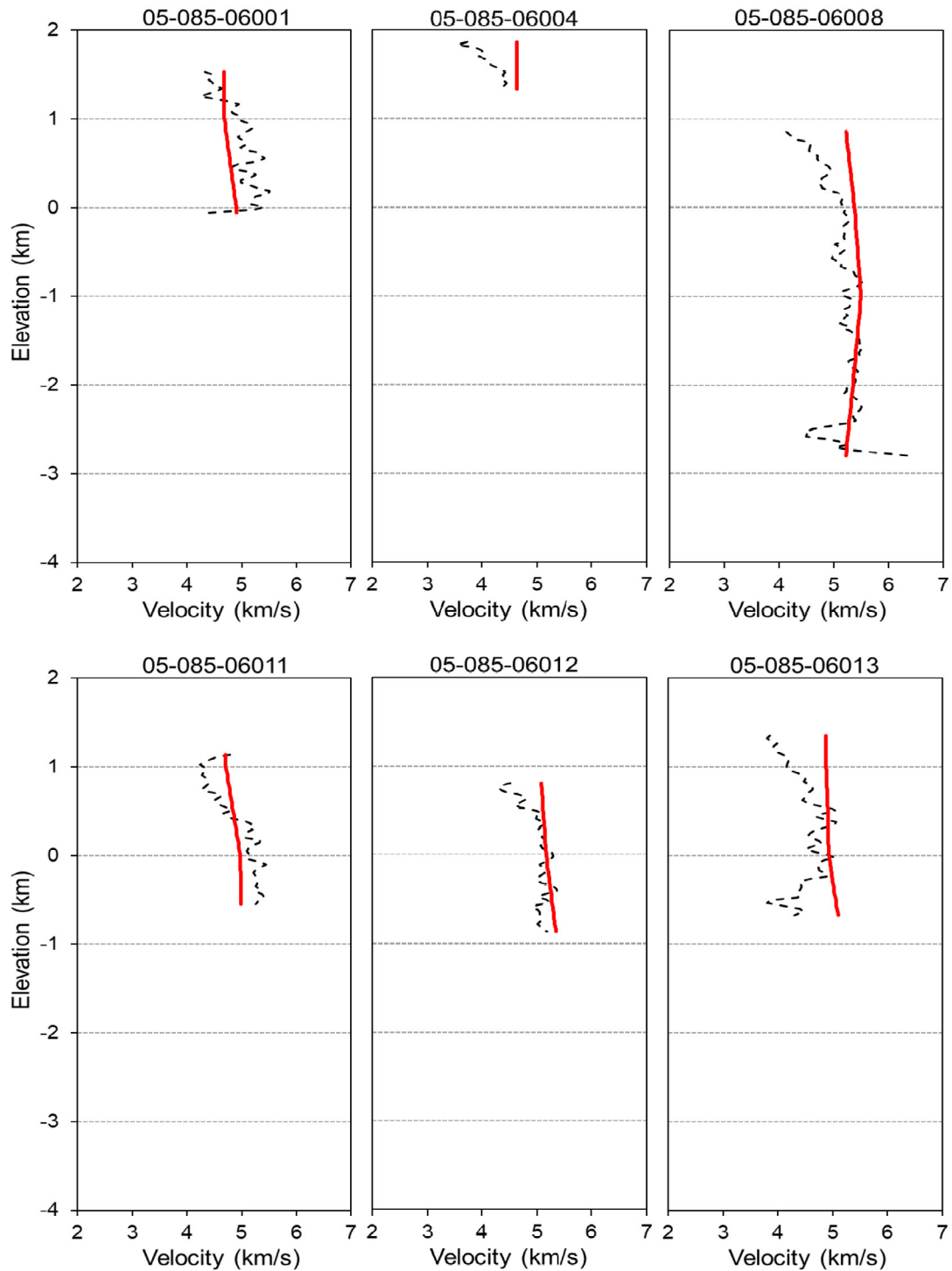


Figure 3-15, continued.

Technical Memorandum 86-68330-2024-7  
Development of a New Velocity Model for the Paradox Valley Area

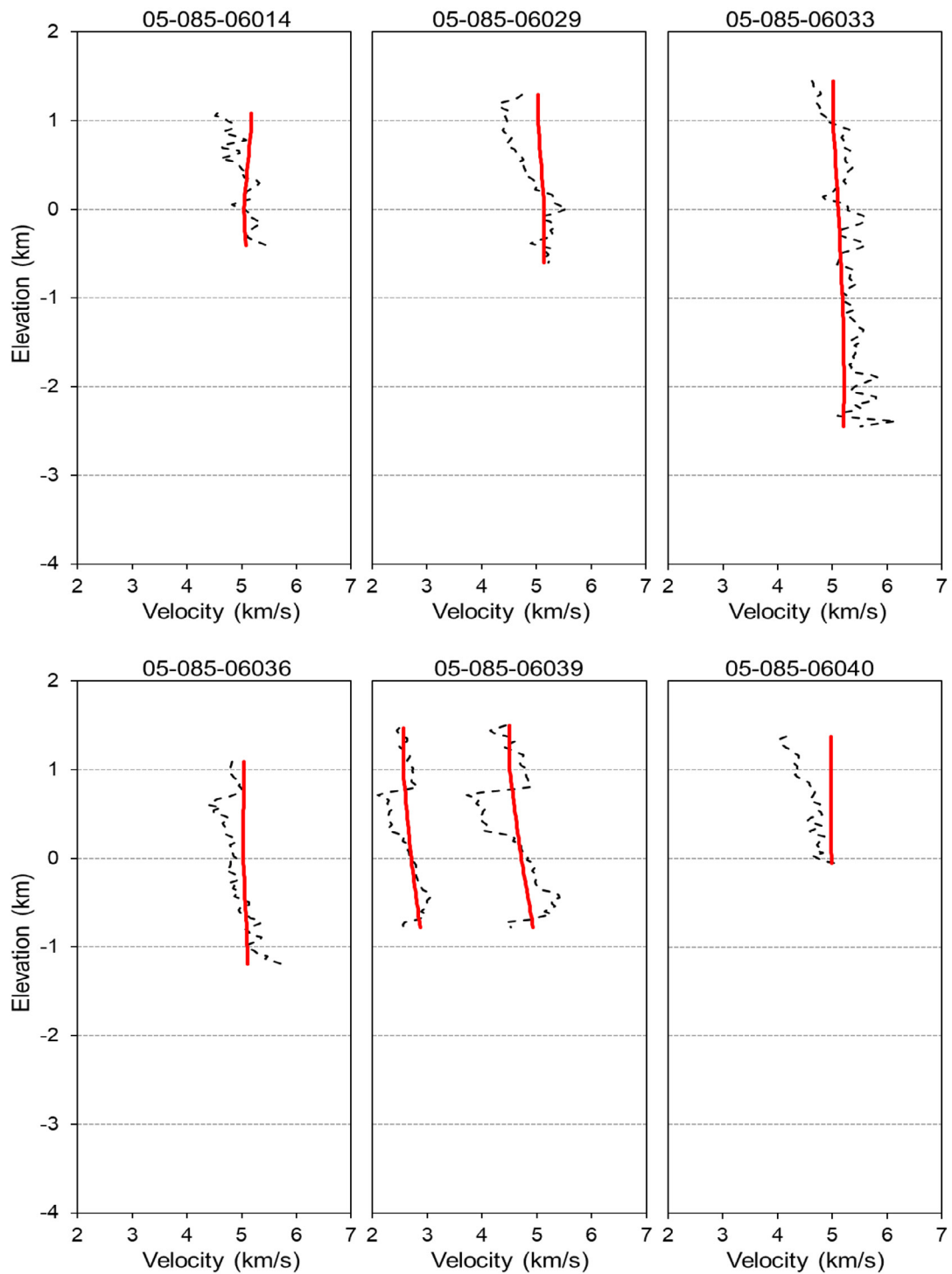


Figure 3-15, continued.

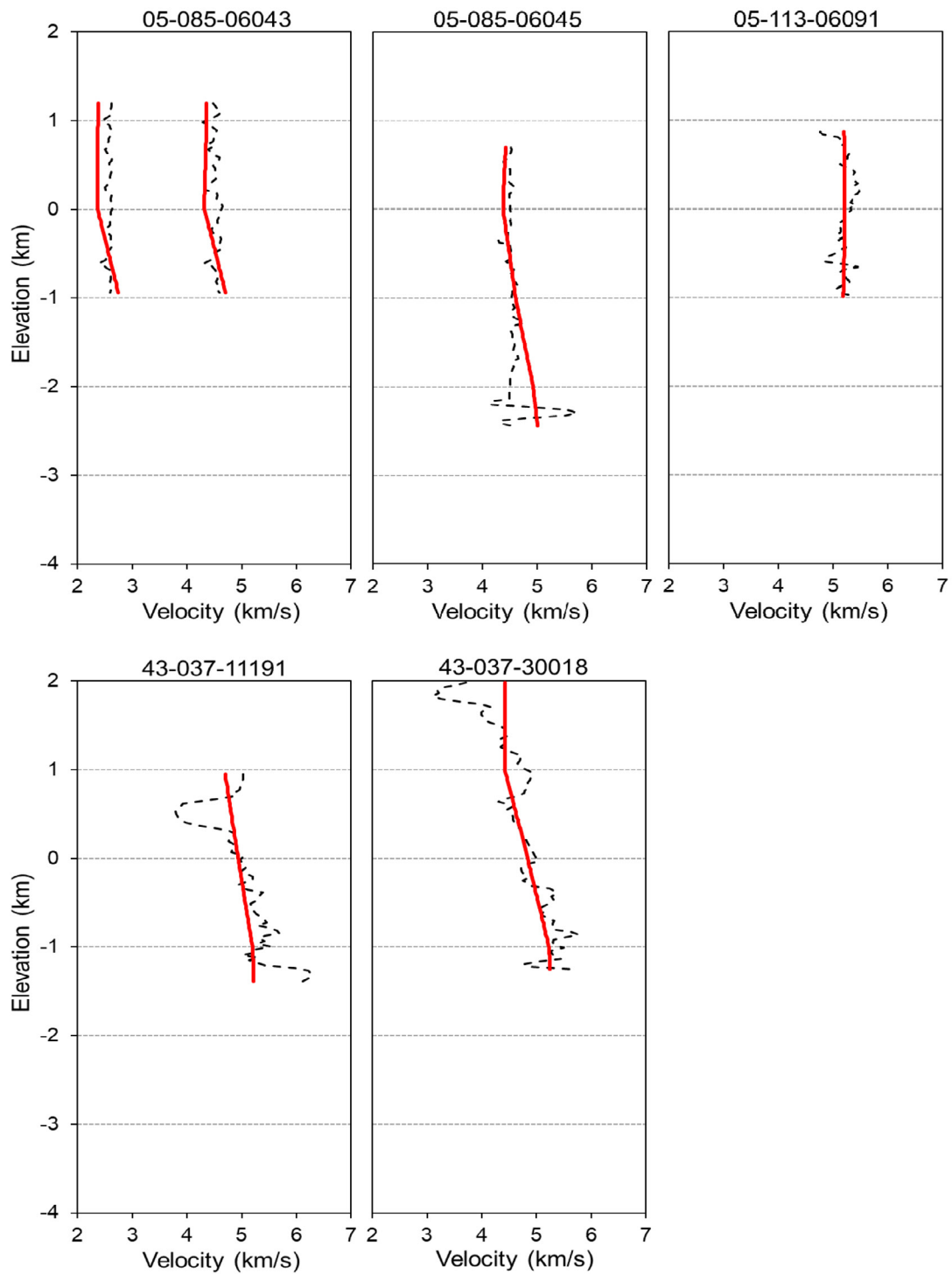


Figure 3-15, continued.

small). The maximum gaps in vertical angular ray coverage are generally greater than  $90^\circ$ , indicating that nearly all ray paths are up-going.

### 3.5 Event Locations

Event hypocenters shift systematically, both horizontally and vertically, between the final 1-D and 3-D velocity models. The sets of earthquake and explosion hypocenters from the final 1-D and 3-D hypocenter-velocity inversions are compared on the map in Figure 3-16. The open red circles and open dark blue squares are the earthquake and explosion hypocenters, respectively, located in the final 1-D velocity model, and the filled white circles and filled light blue squares are the hypocenters located in the final 3-D velocity model. The earthquake hypocenters are also compared on the cross sections in Figure 3-17; explosions are not included in the cross sections because they are constrained to be at the ground surface. Clusters of earthquake and explosion hypocenters shift by up to roughly 2 km horizontally, between the 1-D and 3-D models (Figure 3-16). Clusters of earthquake hypocenters also shift by up to about 3 km vertically (Figure 3-17). Near the PVU injection well, the differences between the earthquake hypocenters from the 1-D and 3-D models are small, because of the weighted constraint on the hypocenters of the earthquakes from the first PVU injection test that was applied during the inversions (section 2.3.2). Farther from the injection well, this constraint influences the models less, and therefore earthquake hypocenters can move more freely. In general, both earthquake and explosion hypocenters move closer to Paradox Valley when going from the 1-D model to the 3-D model (Figure 3-16). The earthquake hypocenters also tend to move deeper (Figure 3-17).

Compared to the previous 3-D velocity model developed for PVSAN, which was computed in 2011, the earthquake hypocenters from the new 3-D model show some relatively small systematic horizontal shifts (Figure 3-18). These shifts are generally less than 1 km, although a couple of the more distant clusters move horizontally by about 2 km. There is little systematic vertical shift in hypocenters computed with the old and new 3-D velocity models (Figure 3-19). Some of the hypocenter clusters appear to become a little more compact with the new velocity model, which can be seen on both the map and cross sections.



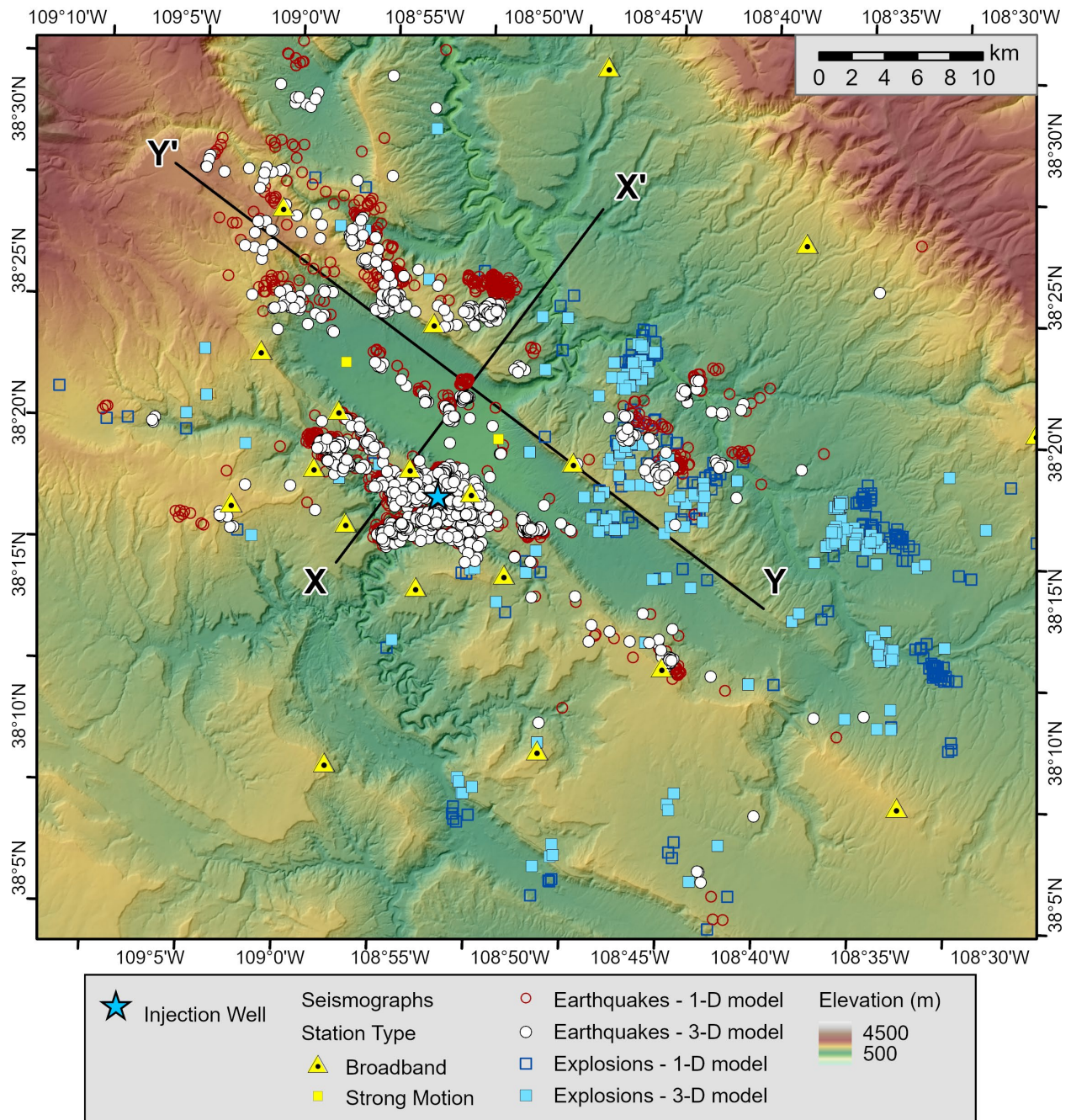
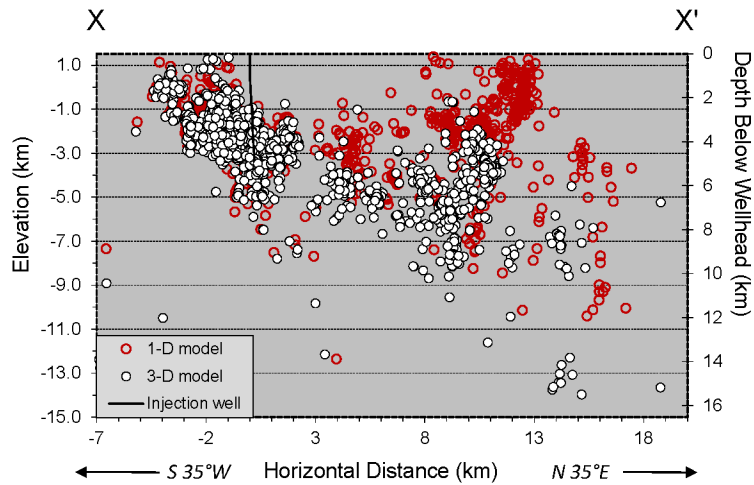


**Figure 3-16: Epicenters of earthquakes and explosions located in the final 1-D velocity model (open red circles and open dark blue squares, respectively) and in the final 3-D velocity model (filled white circles and filled light blue squares). Only the events used in the hypocenter-velocity inversions are included. Vertical cross sections indicated by lines X-X' and Y-Y' are shown in Figure 3-17.**

Technical Memorandum 86-68330-2024-7  
Development of a New Velocity Model for the Paradox Valley Area

(a) Section perpendicular to Paradox Valley, looking to the northwest



(b) Section parallel to Paradox Valley, looking to the southwest

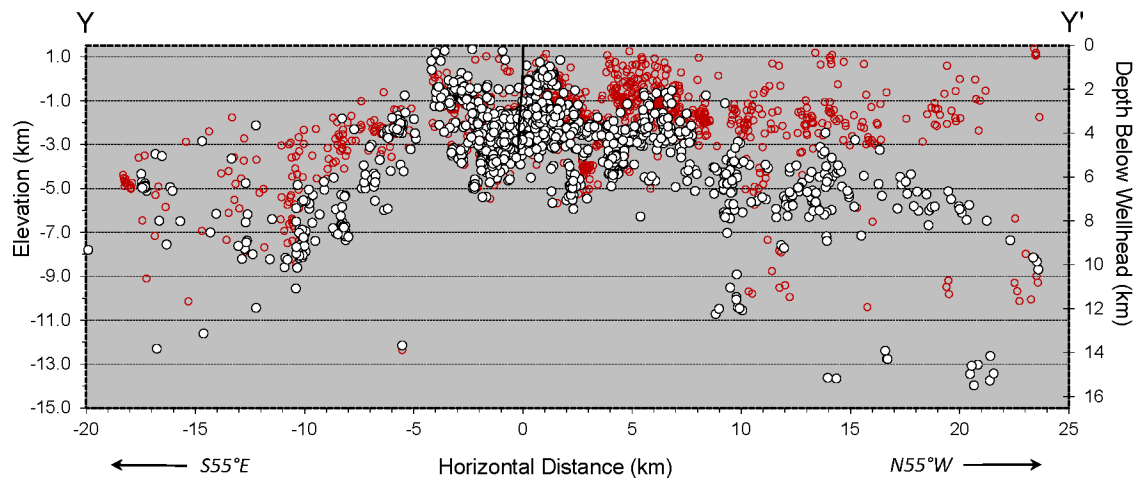


**Figure 3-17: Vertical cross sections of earthquakes located in the final 1-D velocity model (open red circles) and in the final 3-D velocity model (filled white circles). Earthquakes used in the hypocenter-velocity inversions (at all distances from the section lines) are projected onto these cross sections; explosions are excluded. Orientations of these cross sections are shown in Figure 3-16.**



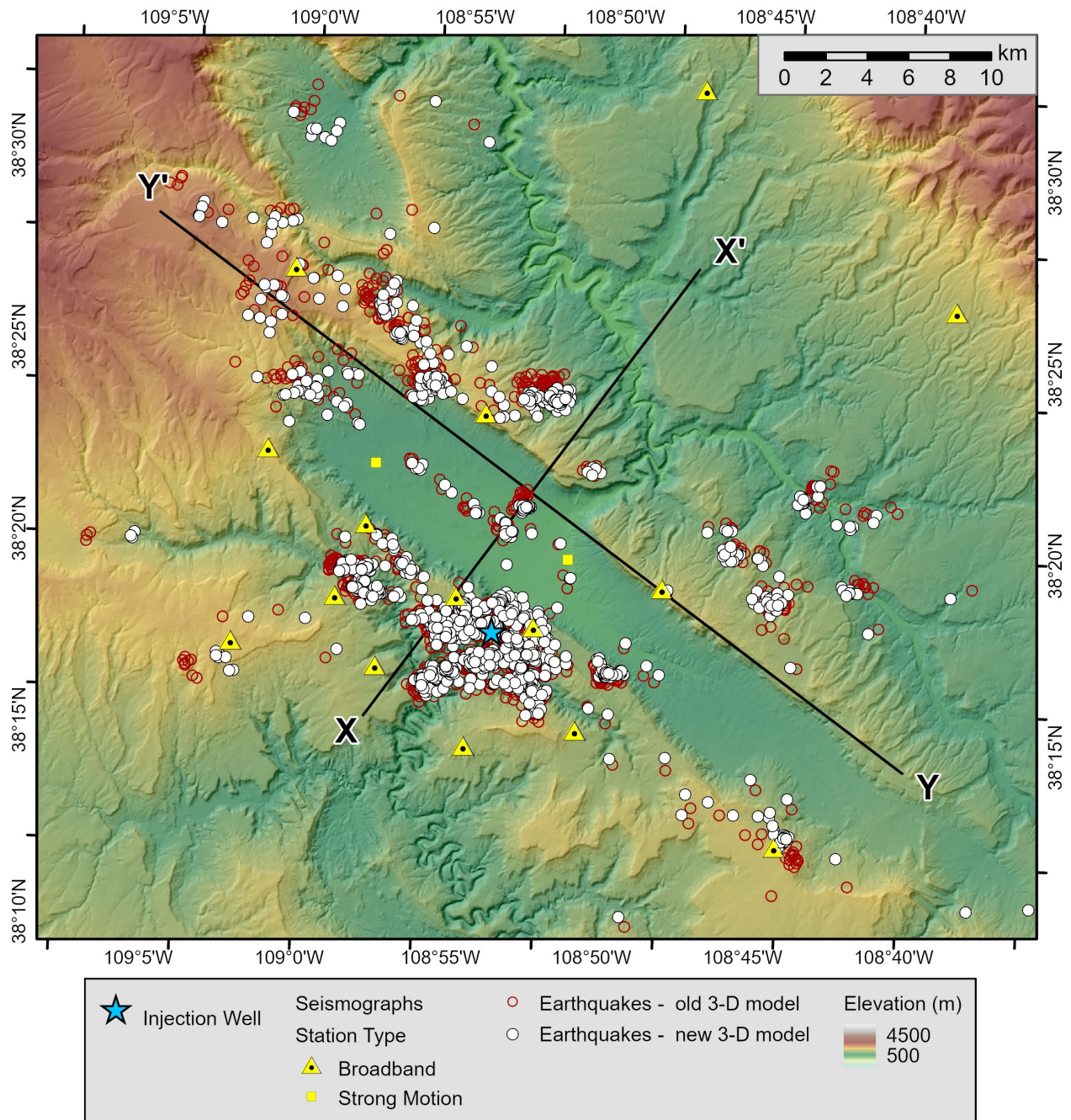
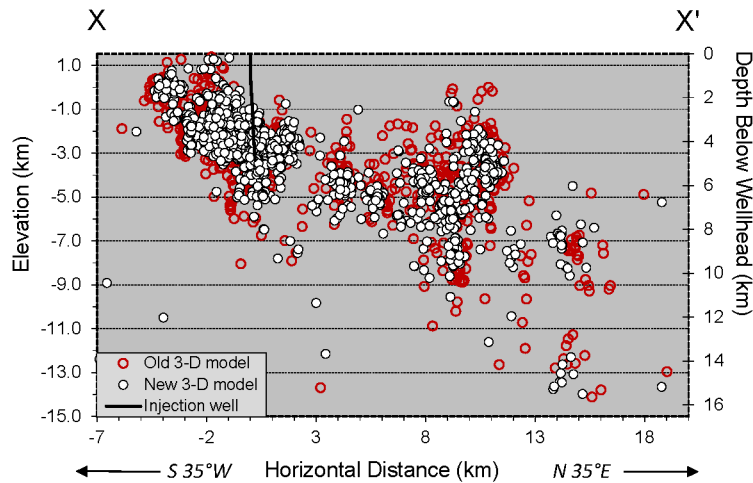


**Figure 3-18: Epicenters of earthquakes located in the previous 3-D velocity model from 2011 (open red circles) and in the new 3-D velocity model (filled white circles). Only the earthquakes used in the recent hypocenter-velocity inversions are included. Vertical cross sections indicated by lines X-X' and Y-Y' are shown in Figure 3-19.**

Technical Memorandum 86-68330-2024-7  
Development of a New Velocity Model for the Paradox Valley Area

(a) Section perpendicular to Paradox Valley, looking to the northwest



(b) Section parallel to Paradox Valley, looking to the southwest

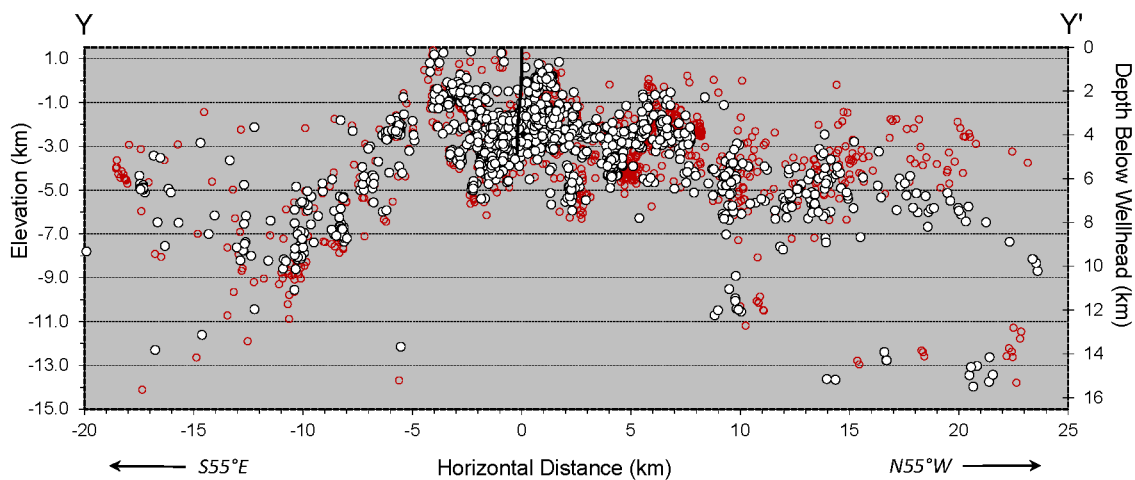


**Figure 3-19: Vertical cross sections of earthquakes located in the previous 3-D velocity model from 2011 (open red circles) and in the new 3-D velocity model (filled white circles). Earthquakes used in the recent hypocenter-velocity inversions (at all distances from the section lines) are projected onto these cross sections. Orientations of these cross sections are shown in Figure 3-18.**

## 4.0 Conclusions

A new velocity model for the Paradox Valley area of western Colorado was developed by performing a series of hypocenter-velocity inversions of arrival times from 1,549 local earthquakes and explosions recorded by the Paradox Valley Seismic Network. Most of the earthquakes used were induced by Reclamation's Paradox Valley Unit deep injection well. These earthquakes are generally less than ~12 km deep, and the majority are less than 6 km deep. A few naturally occurring deeper earthquakes supplemented the dataset. The primary purpose of developing this new velocity model is for use in hypocenter calculations of historical and future PVU-induced seismicity.

Progressive hypocenter-velocity inversions were performed, starting with published regional 1-D velocity models, then determining the best-fitting local 1-D velocity model, and finally computing local 3-D velocity models with gradually increasing variability. P-wave and S-wave arrival times were used in the inversions, and 3-D P-wave and S-wave velocity models were computed simultaneously. These velocity models are independent, other than indirect coupling through the earthquake hypocenters. Station corrections for all PVSN seismic stations were also computed during the inversions. Several constraints were applied to reduce the non-uniqueness of the inversions, including fixing explosion elevations at the local ground surface, using velocity regularization to require smooth models, weighting the earthquakes induced during PVU's first injection test to locate near the injection wellbore, and incorporating velocities from well logs as weighted constraints on the velocity structures.

The mean absolute P-wave and S-wave residuals of the final 3-D model decrease ~20% and ~30%, respectively, compared to the best-fitting local 1-D model. The most prominent feature of the 3-D velocity model is a low-velocity anomaly beneath Paradox Valley. This anomaly is present in both the P-wave and S-wave velocity structures and corresponds to a 4- to 4.5-km-thick salt anticline underlying the valley. Velocities decrease by roughly 15% to 25% within the salt anticline compared to the surrounding areas. Little lateral velocity variation was resolved below an elevation of about -3 to -4 km. Earthquake hypocenters move up to ~2 km laterally and ~3 km vertically for the final 3-D model compared to the best-fitting local 1-D model. Hence, use of a 3-D model to take into account the lateral velocity variations above ~ -3 km elevation is essential for computing accurate hypocenters for the relatively shallow earthquakes induced by PVU injection.

The final 3-D velocity model developed here is included as an electronic attachment to this report, which is described in Appendix C.



## 5.0 References

- Ake, J., Mahrer, K., O'Connell, D., and Block, L., 2005, Deep-Injection and Closely Monitored Induced Seismicity at Paradox Valley, Colorado: *Bulletin of the Seismological Society of America*, v. 95, no. 2, p. 664-683.
- Anooshehpour, R., 2013, *Database of Central and Eastern North American (CENA) Seismic Velocity Structure (Task 2 of USGS-NRC Work Agreement 2011 - 2014)*, United States Nuclear Regulatory Commission, 231 pp.
- Block, L., Wood, C. K., Schwarzer, J., Kang, J. B., Besana-Ostman, G., and Ball, J., 2024, *2023 Annual Report, Paradox Valley Seismic Network, Paradox Valley Unit, Colorado*: Technical Memorandum No. 86-68330-2024-3, Bureau of Reclamation, Denver, Colorado, 88 pp.
- Block, L. V., 2020, *Analysis of the March 4th, 2019 Mw 4.5 Earthquake and Its Aftershocks, Paradox Valley Unit, Colorado*, Technical Memorandum No. 86-68330-2020-07: Technical Memorandum No. 86-68330-2020-07, Bureau of Reclamation, Denver, Colorado, 149 pp.
- Block, L. V., Wood, C. K., Yeck, W. L., and King, V. M., 2015, Induced seismicity constraints on subsurface geological structure, Paradox Valley, Colorado: *Geophysical Journal International*, v. 200, p. 1172-1195.
- Bremkamp, W., and Harr, C. L., 1988, *Area of Least Resistance to Fluid Movement and Pressure Rise*: Report to the Bureau of Reclamation, 49 pp.
- Chulick, G. S., and Mooney, W. D., 2002, Seismic structure of the crust and uppermost mantle of North America and adjacent oceanic basins: a synthesis: *Geophysical Journal International*, v. 92, no. 6, p. 2478-2492.
- Envirocorp Services and Technology Inc., 1995, *Report of Evaluation of Injection Testing for Paradox Valley Injection Test No. 1*, Report to the Bureau of Reclamation, 67 pp.
- Golos, E. M., Fang, H., and Hilst, R. D. v. d., 2020, Variations in seismic wave speed and Vp/Vs ratio in the North American Lithosphere: *Journal of Geophysical Research*, v. 125, no. 12, p. 1-22.
- Harr, C. L., 1988, *Final geological well report, Bureau of Reclamation Injection Test Well No. 1, Paradox Valley, 30-47N-18W, Montrose County, Colorado*, Report to the Bureau of Reclamation, 141 pp.
- Huntoon, P. W., 1988, Late Cenozoic gravity tectonic deformation related to the Paradox salts in the Canyonlands area of Utah, in *Salt Deformation in the Paradox Region*, Utah Geol. Mineral Surv. Bull. 122: Utah Geological and Mineral Survey, Salt Lake City, Utah, p. 79-93.
- Kennett, B. L. N., Engdahl, E. R., and Buland, R., 1995, Constraints on seismic velocities in the Earth from traveltimes: *Geophysical Journal International*, v. 122, no. 1, p. 108-124.
- King, V. M., 2017, *Compilation of Well Data in the Vicinity of Paradox Valley, CO*, Technical Memorandum 85-833000-2017-14, U.S. Department of the Interior, Bureau of Reclamation, Denver, Colorado, 155 pp.
- King, V. M., Block, L. V., Yeck, W. L., Wood, C. K., and Derouin, S. A., 2014, Geological structure of the Paradox Valley Region, Colorado, and relationship to seismicity induced by deep well injection: *J. geophys. Res.: Solid Earth*, v. 119, p. 4955--4978.

- Kluth, C. F., and DuChene, H. R., 2009, Late Pennsylvanian and early Permian structural geology and tectonic history of the Paradox Basin and Uncompahgre Uplift, Colorado and Utah, in *The Paradox Basin Revisited - New Developments in Petroleum Systems and Basin Analysis: Rocky Mountain Association of Geologists Special Publication*, p. 178-197.
- Mooney, W. D., and Boyd, O. S., 2021, Database of Central and Eastern North American Seismic Velocity Structure, U.S. Geological Survey data release, <https://doi.org/10.5066/P91620O4>.
- Pollitz, F. F., and Snoke, J. A., 2010, Rayleigh-wave phase-velocity maps and three-dimensional shear velocity structure of the western US from local non-plane surface wave tomography: *Geophysical Journal International*, v. 180, p. 1153-1169.
- Porritt, R. W., Allen, R. M., and Pollitz, F. F., 2014, Seismic imaging east of the Rocky Mountains with USArray: *Earth and Planetary Science Letters*, v. 402, p. 16-25.
- Rodgers, A., Krischer, L., Afanasiev, M., Boehm, C., Doody, C., Chiang, A., and Simmons, N., 2022, WUS256: An adjoint waveform tomography model of the crust and upper mantle of the western United States for improved waveform simulations: *Journal of Geophysical Research*, v. 127, no. 7, p. 1-30.
- Trudgill, B. D., and Paz, M., 2009, Restoration of mountain front and salt structures in the northern Paradox Basin, SE Utah, in *The Paradox Basin Revisited - New Developments in Petroleum Systems and Basin Analysis: Rocky Mountain Association of Geologists Special Publication*, p. 132-177.

## **Appendix A**

### Mathematical Description of the Hypocenter-Velocity Inversion





The nonlinear hypocenter-velocity inversion is implemented by iteratively solving the linearized problem. The separation-of-parameters technique is used to separate the velocity and station correction matrix inversion from the hypocenter matrix inversions. Constraints are incorporated into the inversions to reduce the non-uniqueness of the problem and to incorporate additional information. The inverse problem is formulated mathematically as a least squares inversion, but residual weighting is used to approximate an L1-norm optimization. The mathematical description of this procedure is provided below. The description is generalized for three-dimensional velocity models. For inversions performed with one-dimensional velocity models, the formulation is the same but the velocities only vary in the vertical direction.

## The Forward Problem

The P-wave and S-wave velocity structures are represented by a 3-D rectangular grid of nodes, with linear interpolation of the velocities between nodes. The velocity  $V$  at any point  $(X, Y, Z)$  is computed from the velocities at the eight nodes surrounding it:

$$V(X, Y, Z) = \sum_{i=1}^8 v_i \left(1 - \frac{|X-x_i|}{dx}\right) \left(1 - \frac{|Y-y_i|}{dy}\right) \left(1 - \frac{|Z-z_i|}{dz}\right), \quad (A-1)$$

where  $(x_i, y_i, z_i)$  are the coordinates of the  $i^{\text{th}}$  node, and  $v_i$  is its velocity. The parameters  $dx$ ,  $dy$ , and  $dz$  are the distances in the  $x$ ,  $y$ , and  $z$  directions between the velocity nodes surrounding the point  $(X, Y, Z)$ .

The ray bending method of Um and Thurber (1987), as modified by Block (1991), is used to compute ray paths and travel times. This method starts with a straight ray path defined by two endpoints at the seismic source (earthquake or explosion) and receiver (seismic station) and one midpoint (i.e., the ray path is broken into two equal segments). The midpoint of the ray path is iteratively perturbed until the travel time is minimized. Each of the two segments is then divided in half. Each of the points along the ray path (excluding the endpoints) are then iteratively perturbed until the travel time is minimized. The process of dividing ray path segments and iteratively perturbing the ray path points is repeated until convergence of the computed travel time is achieved.

Station corrections,  $sc$ , are incorporated as constant values added to the travel times computed by the ray tracing from source to receiver ( $t_{\text{travel}}$ ). A separate P-wave and S-wave correction is included for each seismic station.

## The Inverse Problem

Let  $t_{\text{obs}}$  = an observed arrival time (either P or S);  $t_{\text{calc}}$  = the corresponding calculated arrival time based on the current model ( $t_{\text{calc}}$  = hypocenter origin time,  $t_0$ , +  $t_{\text{travel}}$  +  $sc$ ), and  $r$  = the residual =  $t_{\text{obs}} - t_{\text{calc}}$ . The goal is to change the model parameters so that the change in calculated

arrival time,  $\Delta t_{calc}$ , is equal to the residual  $r$ . Expanding  $\Delta t_{calc}$  in terms of changes in the model parameters and keeping only the first-order terms gives:

$$\Delta t_0 + \frac{\partial t}{\partial x} \Delta x + \frac{\partial t}{\partial y} \Delta y + \frac{\partial t}{\partial z} \Delta z + \sum_{j=1}^{nnodes} \frac{\partial t}{\partial v_j} \Delta v_j + \Delta sc = r, \quad (A-2)$$

where  $t_0$ ,  $x$ ,  $y$ , and  $z$  are the hypocenter parameters,  $v_j$  is the P-wave or S-wave velocity of the  $j^{th}$  node,  $sc$  is the P-wave or S-wave station correction, and  $nnodes$  is the number of nodes in the velocity grid.

The partial derivatives are computed analytically. The partial derivatives with respect to the hypocenter parameters are given by:

$$\frac{\partial t}{\partial x} = \frac{-1}{v(x,y,z)} \frac{dx}{ds}, \quad \frac{\partial t}{\partial y} = \frac{-1}{v(x,y,z)} \frac{dy}{ds}, \quad \text{and} \quad \frac{\partial t}{\partial z} = \frac{-1}{v(x,y,z)} \frac{dz}{ds}, \quad (A-3)$$

where  $dx/ds$ ,  $dy/ds$ , and  $dz/ds$  are the direction cosines of the ray path at the hypocenter, and  $v(x,y,z)$  is the velocity at the hypocenter. The partial derivatives with respect to the velocity nodes are computed by summing the contributions from all ray path segments. Given a ray path of  $n$  segments, each of length  $\Delta s$ , the partial derivative of the travel time with respect to the velocity at the  $j^{th}$  node is given by:

$$\frac{\partial t}{\partial v_j} = \sum_{l=1}^n \frac{-\Delta s}{v(x_l, y_l, z_l)^2} \frac{\partial v(x_l, y_l, z_l)}{\partial v_j}, \quad (A-4)$$

where  $v(x_l, y_l, z_l)$  is the velocity at the center of the  $l^{th}$  ray path segment. For each ray path segment,  $\partial v(x_l, y_l, z_l) / \partial v_j$  is only nonzero for the eight velocity nodes surrounding it and is found by differentiating equation A-1:

$$\frac{\partial v(x_l, y_l, z_l)}{\partial v_j} = \left(1 - \frac{|x_l - x_j|}{dx}\right) \left(1 - \frac{|y_l - y_j|}{dy}\right) \left(1 - \frac{|z_l - z_j|}{dz}\right). \quad (A-5)$$

Equation A-5 is used to compute partial derivatives of P-wave travel times with respect to P-wave velocities and partial derivatives of S-wave travel times with respect to S-wave velocities.

Equation A-2 is constructed for each observed P-wave or S-wave arrival time and is weighted according to the quality of the arrival time pick. (In addition, a residual cut-off is employed to discard extreme outliers.) For an approximate L1-norm optimization, both sides of equation A-2 are divided by  $(|r|)^{1/2}$  (Scales et. al., 1988). If the absolute value of the residual is less than a specified threshold, this L1 weighting is not applied. This prevents creating extremely large weighted residuals and also allows for a transition from the L2 norm to the L1 norm. For this study, P-wave and S-wave L1 weighting thresholds of 0.05 s were used for initial L1-norm inversions and P-wave and S-wave thresholds of 0.01 s and 0.03 s, respectively, were used for the final inversions.

All of the arrival times for the  $i^{\text{th}}$  event yield a set of equations that can be put into matrix form:

$$\mathbf{H}_i \Delta \mathbf{h}_i + \mathbf{M}_i \Delta \mathbf{m}_i = \mathbf{r}_i. \quad (\text{A-6})$$

The matrix  $\mathbf{H}_i$  contains the weighted hypocenter partial derivatives, the matrix  $\mathbf{M}_i$  contains the weighted velocity and station correction partial derivatives, and the vector  $\mathbf{r}_i$  contains the weighted residuals. (The station correction partial derivatives are simply *ones* in the appropriate columns.) The vectors  $\Delta \mathbf{h}_i$  and  $\Delta \mathbf{m}_i$  contain the hypocenter perturbations for the  $i^{\text{th}}$  event and velocity and station correction perturbations, respectively.

If there are more than four arrival times, there exists a matrix  $\mathbf{T}_i$  such that  $\mathbf{T}_i^T \mathbf{H}_i = 0$  (Pavlis and Booker, 1980, Roecker, 1982). The matrix  $\mathbf{T}_i$  is computed by QR factorization of  $\mathbf{H}_i$  (Block, 1991). Multiplying both sides of equation A-6 by  $\mathbf{T}_i^T$  yields

$$\mathbf{M}_i' \Delta \mathbf{m}_i = \mathbf{r}_i'. \quad (\text{A-7})$$

where  $\mathbf{M}_i' = \mathbf{T}_i^T \mathbf{M}_i$  and  $\mathbf{r}_i' = \mathbf{T}_i^T \mathbf{r}_i$ . The arrival times for each seismic event are processed in this way, and the results from all events are combined into one matrix equation:

$$\mathbf{M}' \Delta \mathbf{m} = \mathbf{r}'. \quad (\text{A-8})$$

Equation A-8 represents a velocity-station correction inversion, where the corresponding changes to the hypocenter parameters are also considered.

## Constraints

### Locations of First Induced Earthquakes

The 22 earthquakes induced near the PVU injection well during the first injection test in July 1991 are constrained to be near the PVU wellbore, at the mid-depth of the perforations in the primary target injection formation, the Leadville. (The reasons for incorporating this constraint are discussed in the main body of the report.) Let  $(x_0, y_0, z_0)$  be the desired location of these earthquakes, and let  $(x, y, z)$  represent the current location of one of these events. This constraint requires:

$$\begin{aligned} x + \Delta x &= x_0 & \text{or} & & \Delta x &= x_0 - x, \\ y + \Delta y &= y_0 & \text{or} & & \Delta y &= y_0 - y, \\ z + \Delta z &= z_0 & \text{or} & & \Delta z &= z_0 - z. \end{aligned}$$

Therefore, when matrix equation A-6 is constructed for each of these earthquakes (prior to implementation of the separation-of-parameters), three additional rows are added. These rows contain *ones* in the appropriate columns of  $\mathbf{H}_i$  (corresponding to the parameters  $\Delta x$ ,  $\Delta y$ , and  $\Delta z$  in the vector  $\Delta \mathbf{h}_i$ ) and the location residuals  $(x_0 - x, y_0 - y, z_0 - z)$  in the corresponding elements of the vector  $\mathbf{r}_i$ . These rows are multiplied by a constant factor that weights this constraint relative to satisfying the arrival time residuals for these earthquakes. In addition, the rows of matrix

equation A-6 for the arrival time residuals may also be multiplied by a constant factor that weights the importance of the data for these earthquakes in the inversion.

### P-wave Station Correction Sum

When all earthquake hypocenters and all station corrections vary simultaneously, there is a trade-off between the station corrections and earthquake origin times. All earthquake origin times and all station corrections for one phase (either P-wave or S-wave) could shift by the same amount, and the arrival time residuals would be unchanged. To compensate for this trade-off, a constraint is added that requires the sum of the P-wave station corrections ( $sc_p$ ) to be zero:

$$\sum_{j=1}^{n_{stations}} (sc_{pj} + \Delta sc_{pj}) = 0,$$

or

$$\sum_{j=1}^{n_{stations}} \Delta sc_{pj} = - \sum_{j=1}^{n_{stations}} sc_{pj}.$$

This equation may be represented in matrix form involving the model solution vector  $\Delta m$ :

$$\mathbf{S} \Delta m = -s. \quad (A-9)$$

The vector  $s$  contains the P-wave station correction sum based on the current model, and the matrix  $\mathbf{S}$  contains *ones* in the columns that correspond to the P-wave station correction changes ( $\Delta sc_{pj}$ ,  $j = 1, n_{stations}$ ) in the vector  $\Delta m$ . This constraint is added as an additional row to matrix equation A-8 (after all events have been processed by the separation-of-parameters technique). Because this constraint compensates for a trade-off in the inversion, it does not need to be weighted.

### Velocity Regularization

To prevent extreme fluctuations of the velocity structures at poorly resolved nodes, velocity regularization is included in the velocity-station correction inversion. The regularization is implemented by minimizing the first-order spatial velocity derivatives. Equations are formed which set the numerical velocity derivatives for consecutive pairs of velocity nodes to zero. This is represented by:

$$[(v_i + \Delta v_i) - (v_{i-1} + \Delta v_{i-1})] / d = 0,$$

where  $v_i$  and  $v_{i-1}$  are the velocities of two consecutive nodes in one coordinate direction, and  $d$  is the distance between the nodes. Equations for all consecutive nodes in the  $x$ ,  $y$ , and  $z$  directions are constructed. Rearranging the terms, the equations may be expressed as a matrix equation involving the model solution vector  $\Delta m$ :

$$\mathbf{V} \Delta m = -v. \quad (A-10)$$

The vector  $v$  contains the numerical spatial velocity derivatives based on the current model, and the matrix  $\mathbf{V}$  contains the numerical derivative coefficients ( $1/d$ ,  $-1/d$ ). These equations are added

as additional rows to matrix equation A-8. All rows are multiplied by a constant factor,  $\lambda$ , to weight this constraint relative to satisfying the arrival time residuals and the other constraints. In addition, different weighting factors may be used for the P-wave and S-wave velocity structures, and different weighting may be used for the horizontal and vertical spatial derivatives.

## Velocity Data Points

Velocities from other data sources, such as geophysical borehole logs, can be incorporated into the inversion as constraints. Each velocity data point  $V$  at coordinates  $(X, Y, Z)$  adds constraints to the eight velocity nodes surrounding it:

$$\sum_{i=1}^8 \left(1 - \frac{|X-x_i|}{dx}\right) \left(1 - \frac{|Y-y_i|}{dy}\right) \left(1 - \frac{|Z-z_i|}{dz}\right) (v_i + \Delta v_i) = V,$$

where  $(x_i, y_i, z_i)$  are coordinates of the  $i^{\text{th}}$  node and  $v_i$  is its velocity value. The equations for all velocity data points are given in matrix form by:

$$\mathbf{D} \Delta \mathbf{m} = \mathbf{d}. \quad (\text{A-11})$$

The matrix  $\mathbf{D}$  contains the node interpolation coefficients, and the vector  $\mathbf{d}$  contains the velocity data point residuals, i.e., the velocities from the geophysical survey minus the corresponding calculated velocities based on the current model. These equations are added as additional rows to matrix equation A-8. All rows are multiplied by a constant factor,  $\alpha$ , to weight this constraint relative to satisfying the arrival time residuals and the other constraints.

## Solution

Adding the constraints for the P-wave station correction sum, the velocity regularization, and the velocity data points to equation A-8 gives:

$$\mathbf{A} \Delta \mathbf{m} = \begin{bmatrix} \mathbf{M}' \\ \mathbf{S} \\ \lambda \mathbf{V} \\ \alpha \mathbf{D} \end{bmatrix} \Delta \mathbf{m} = \begin{bmatrix} \mathbf{r}' \\ -\mathbf{s} \\ -\lambda \mathbf{v} \\ \alpha \mathbf{d} \end{bmatrix} = \mathbf{b}. \quad (\text{A-12})$$

The columns of matrix  $\mathbf{A}$  are normalized, equation A-12 is solved using a least squares conjugate gradient algorithm, and the solution vector  $\mathbf{b}$  is then corrected for the column normalization. If the maximum absolute change in P-wave velocity ( $dv_{\text{max}}$ ) is greater than a specified threshold ( $chg_{\text{max}}$ , 0.2 km/s for this study), then the solution vector is scaled by  $chg_{\text{max}}/dv_{\text{max}}$ . This scaling is applied to prevent the model from changing too much during one iteration of the linearized implementation of the nonlinear problem.

After velocities and station corrections are updated, the hypocenters are subsequently individually relocated with an iterative, approximate L1-norm (residual-weighted least squares) inversion. An undamped inversion is tried first. If the event location does not converge within 50

iterations, damping is added and the event quality factor is changed. Most events used in the hypocenter-velocity inversion are constrained well enough for the undamped relocation algorithm to converge. The hypocenter convergence criteria used for this study were 0.05 km for x and y, 0.01 km for z, and 0.005 s for  $t_0$ . A progressive relocation approach is used, as in Roecker (1982). The horizontal hypocenter coordinates are recomputed first, then all four hypocenter coordinates are allowed to vary. The hypocenters for the induced earthquakes recorded during the first injection test are constrained to be near the PVU injection wellbore at the depth of the Leadville formation, as described previously. The z coordinates of explosions are fixed during the hypocenter relocation. Once new x and y coordinates and a new origin time are computed for an explosion, its z coordinate is set to the elevation of the local ground elevation.

The entire hypocenter-velocity-station correction inversion procedure is iteratively repeated until convergence of the arrival times residuals is achieved. Convergence is determined subjectively, by evaluating the improvement in residuals versus the increased variability of the velocity model.

## References

- Block., L. V., 1991, Joint hypocenter-velocity inversion of local earthquake arrival time data in two geothermal regions, *Sc. D. Thesis*, Mass. Inst. Tech., 448 pp.
- Pavlis, G. L., and J. R. Booker, 1980, The mixed discrete-continuous inverse problem: application to the simultaneous determination of earthquake hypocenters and velocity structure, *J. Geophys. Res.*, **85**, 4801-4810.
- Roecker, S. W., 1982, Velocity structure of the Pamir-Hindi Kush region: Possible evidence of subducted crust, *J. Geophys. Res.*, **87**, 945-959.
- Scales, J. A., A. Gersztenkorn, and S. Treitel, 1988, Fast solution of large, sparse, linear systems: Application to seismic traveltime tomography, *J. Comp. Phys.*, **75**, 314-333.
- Um, J., and C. Thurber, 1987, A fast algorithm for two-point seismic ray tracing, *Bull. Seis. Soc. Am.*, **77**, 972-98

## **Appendix B**

### Ray Coverage Plots





Ray coverage parameters were computed using the velocities and hypocenters from the final 3-D hypocenter-velocity inversion. These parameters were computed on a 3-D grid with a uniform node spacing of 2.5 km. The grid used for these computations extends beyond the area where velocities varied during the inversions, to incorporate all source-receiver ray paths. For each node in the grid, the following parameters were computed: the number of seismic rays, or "hits"; the maximum gap in horizontal angular (azimuthal) ray coverage (degrees); and the maximum gap in vertical angular ray coverage (degrees). These parameters were computed separately for P waves and S waves.

Horizontal and vertical sections through the 3-D grid of ray coverage parameters are included in this appendix. For the sections of the number of rays, the scales for most plots range from 0 to 500, and numbers above 500 are clipped. The exceptions are the horizontal sections at elevations of -10 km and -15 km. The scales for these plots range from 0 to 100. For all sections of the maximum gap in horizontal or vertical angular ray coverage, the scales range from 0° to 180°.

Figure	Page
Figure B-1: Horizontal section of the number of seismic rays (hits) for the final 3-D hypocenter-velocity inversion at an elevation of 1 km: (a) P waves (b) S waves .....	B-5
Figure B-2: Horizontal section of the number of seismic rays (hits) for the final 3-D hypocenter-velocity inversion at an elevation of 0 km: (a) P waves (b) S waves .....	B-6
Figure B-3: Horizontal section of the number of seismic rays (hits) for the final 3-D hypocenter-velocity inversion at an elevation of -1 km: (a) P waves (b) S waves .....	B-7
Figure B-4: Horizontal section of the number of seismic rays (hits) for the final 3-D hypocenter-velocity inversion at an elevation of -2 km: (a) P waves (b) S waves .....	B-8
Figure B-5: Horizontal section of the number of seismic rays (hits) for the final 3-D hypocenter-velocity inversion at an elevation of -3 km: (a) P waves (b) S waves .....	B-9
Figure B-6: Horizontal section of the number of seismic rays (hits) for the final 3-D hypocenter-velocity inversion at an elevation of -4 km: (a) P waves (b) S waves .....	B-10
Figure B-7: Horizontal section of the number of seismic rays (hits) for the final 3-D hypocenter-velocity inversion at an elevation of -5 km: (a) P waves (b) S waves .....	B-11
Figure B-8: Horizontal section of the number of seismic rays (hits) for the final 3-D hypocenter-velocity inversion at an elevation of -10 km: (a) P waves (b) S waves .....	B-12
Figure B-9: Horizontal section of the number of seismic rays (hits) for the final 3-D hypocenter-velocity inversion at an elevation of -15 km: (a) P waves (b) S waves .....	B-13

Figure B-10: Vertical sections perpendicular to Paradox Valley of the number of P-wave rays (hits) for the final 3-D hypocenter-velocity inversion .....	B-14
Figure B-11: Vertical sections perpendicular to Paradox Valley of the number of S-wave rays (hits) for the final 3-D hypocenter-velocity inversion .....	B-15
Figure B-12: Vertical sections parallel to Paradox Valley of the number of P-wave rays (hits) for the final 3-D hypocenter-velocity inversion .....	B-16
Figure B-13: Vertical sections parallel to Paradox Valley of the number of S-wave rays (hits) for the final 3-D hypocenter-velocity inversion .....	B-17
Figure B-14: Horizontal section of the maximum gap in horizontal angular ray coverage (deg.) for the final 3-D hypocenter-velocity inversion at an elevation of 1 km: (a) P waves (b) S waves .....	B-18
Figure B-15: Horizontal section of the maximum gap in horizontal angular ray coverage (deg.) for the final 3-D hypocenter-velocity inversion at an elevation of 0 km: (a) P waves (b) S waves .....	B-19
Figure B-16: Horizontal section of the maximum gap in horizontal angular ray coverage (deg.) for the final 3-D hypocenter-velocity inversion at an elevation of -1 km: (a) P waves (b) S waves .....	B-20
Figure B-17: Horizontal section of the maximum gap in horizontal angular ray coverage (deg.) for the final 3-D hypocenter-velocity inversion at an elevation of -2 km: (a) P waves (b) S waves .....	B-21
Figure B-18: Horizontal section of the maximum gap in horizontal angular ray coverage (deg.) for the final 3-D hypocenter-velocity inversion at an elevation of -3 km: (a) P waves (b) S waves .....	B-22
Figure B-19: Horizontal section of the maximum gap in horizontal angular ray coverage (deg.) for the final 3-D hypocenter-velocity inversion at an elevation of -4 km: (a) P waves (b) S waves .....	B-23
Figure B-20: Horizontal section of the maximum gap in horizontal angular ray coverage (deg.) for the final 3-D hypocenter-velocity inversion at an elevation of -5 km: (a) P waves (b) S waves .....	B-24
Figure B-21: Horizontal section of the maximum gap in horizontal angular ray coverage (deg.) for the final 3-D hypocenter-velocity inversion at an elevation of -10 km: (a) P waves (b) S waves.....	B-25

Figure B-22: Horizontal section of the maximum gap in horizontal angular ray coverage (deg.) for the final 3-D hypocenter-velocity inversion at an elevation of -15 km: (a) P waves (b) S waves.....	B-26
Figure B-23: Vertical sections perpendicular to Paradox Valley of the maximum gap in P-wave horizontal angular ray coverage (deg.) for the final 3-D hypocenter-velocity inversion .....	B-27
Figure B-24: Vertical sections perpendicular to Paradox Valley of the maximum gap in S-wave horizontal angular ray coverage (deg.) for the final 3-D hypocenter-velocity inversion .....	B-28
Figure B-25: Vertical sections parallel to Paradox Valley of the maximum gap in P-wave horizontal angular ray coverage (deg.) for the final 3-D hypocenter-velocity inversion. ....	B-29
Figure B-26: Vertical sections parallel to Paradox Valley of the maximum gap in S-wave horizontal angular ray coverage (deg.) for the final 3-D hypocenter-velocity inversion. ....	B-30
Figure B-27: Horizontal section of the maximum gap in vertical angular ray coverage (deg.) for the final 3-D hypocenter-velocity inversion at an elevation of 1 km: (a) P waves (b) S waves.....	B-31
Figure B-28: Horizontal section of the maximum gap in vertical angular ray coverage (deg.) for the final 3-D hypocenter-velocity inversion at an elevation of 0 km: (a) P waves (b) S waves.....	B-32
Figure B-29: Horizontal section of the maximum gap in vertical angular ray coverage (deg.) for the final 3-D hypocenter-velocity inversion at an elevation of -1 km: (a) P waves (b) S wave .....	B-33
Figure B-30: Horizontal section of the maximum gap in vertical angular ray coverage (deg.) for the final 3-D hypocenter-velocity inversion at an elevation of -2 km: (a) P waves (b) S waves .....	B-34
Figure B-31: Horizontal section of the maximum gap in vertical angular ray coverage (deg.) for the final 3-D hypocenter-velocity inversion at an elevation of -3 km: (a) P waves (b) S waves .....	B-35
Figure B-32: Horizontal section of the maximum gap in vertical angular ray coverage (deg.) for the final 3-D hypocenter-velocity inversion at an elevation of -4 km: (a) P waves (b) S waves .....	B-36
Figure B-33: Horizontal section of the maximum gap in vertical angular ray coverage (deg.) for the final 3-D hypocenter-velocity inversion at an elevation of -5 km: (a) P waves (b) S waves .....	B-37

Figure B-34: Horizontal section of the maximum gap in vertical angular ray coverage (deg.) for the final 3-D hypocenter-velocity inversion at an elevation of -10 km: (a) P waves (b) S waves ...  
..... B-38

Figure B-35: Horizontal section of the maximum gap in vertical angular ray coverage (deg.) for the final 3-D hypocenter-velocity inversion at an elevation of -15 km: (a) P waves (b) S waves ...  
..... B-39

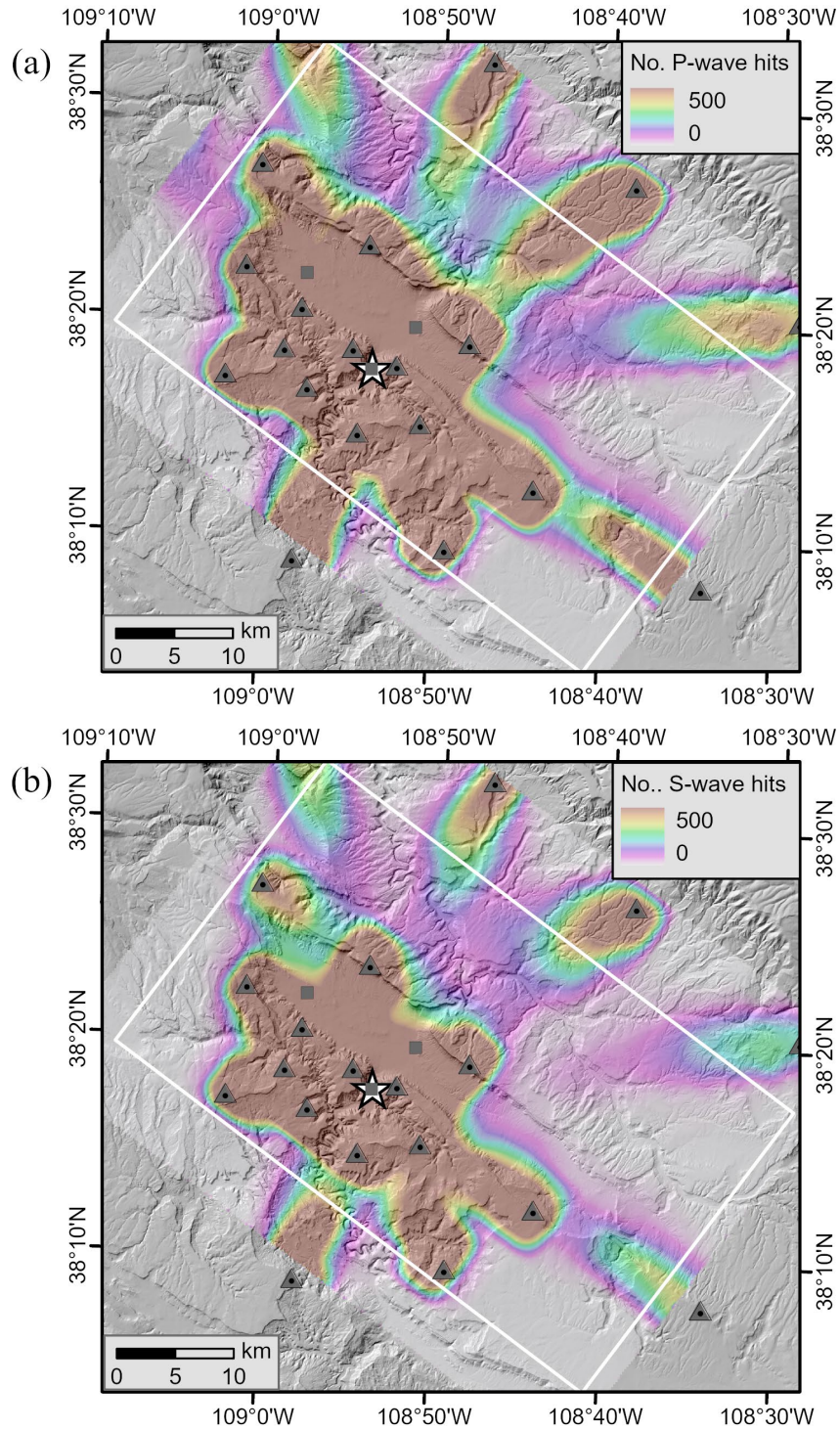
Figure B-36: Vertical sections perpendicular to Paradox Valley of the maximum gap in P-wave vertical angular ray coverage (deg.) for the final 3-D hypocenter-velocity inversion..... B-40

Figure B-37: Vertical sections perpendicular to Paradox Valley of the maximum gap in S-wave vertical angular ray coverage (deg.) for the final 3-D hypocenter-velocity inversion..... B-41

Figure B-38: Vertical sections parallel to Paradox Valley of the maximum gap in P-wave vertical angular ray coverage (deg.) for the final 3-D hypocenter-velocity inversion..... B-42

Figure B-39: Vertical sections parallel to Paradox Valley of the maximum gap in S-wave vertical angular ray coverage (deg.) for the final 3-D hypocenter-velocity inversion..... B-43

Technical Memorandum 86-68330-2024-7  
Development of a New Velocity Model for the Paradox Valley Area



**Figure B-1: Horizontal section of the number of seismic rays (hits) for the final 3-D hypocenter-velocity inversion at an elevation of 1 km: (a) P waves (b) S waves. The white star is the location of the PVU injection well. The gray triangles are the locations of the broadband seismic stations, and the gray squares are the locations of the strong motion stations. The white rectangle is the area where velocities varied during the initial inversions.**



Technical Memorandum 86-68330-2024-7  
Development of a New Velocity Model for the Paradox Valley Area

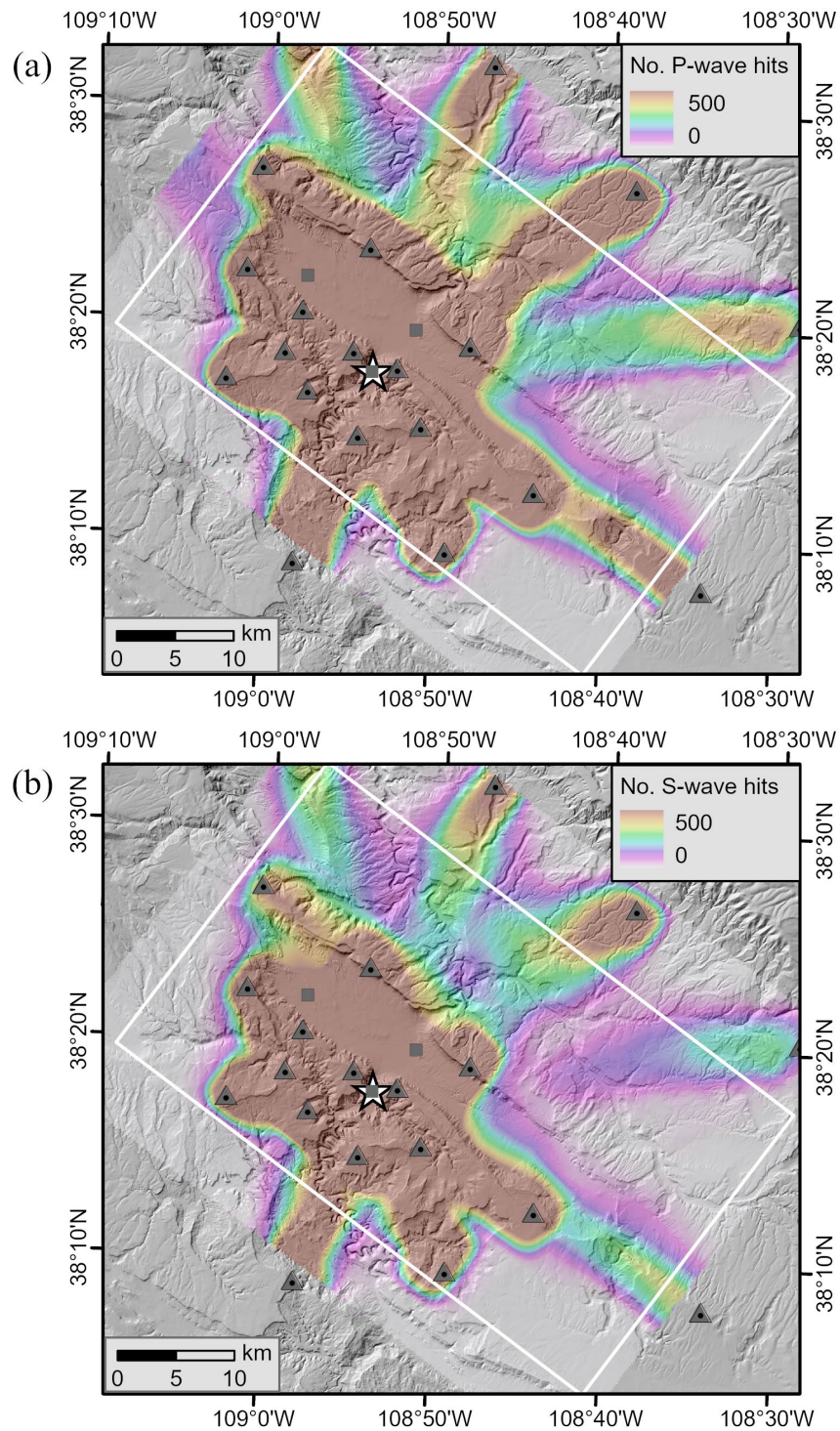


**Figure B-2: Horizontal section of the number of seismic rays (hits) for the final 3-D hypocenter-velocity inversion at an elevation of 0 km: (a) P waves (b) S waves. The white star is the location of the PVU injection well. The gray triangles are the locations of the broadband seismic stations, and the gray squares are the locations of the strong motion stations. The white rectangle is the area where velocities varied during the initial inversions.**



Technical Memorandum 86-68330-2024-7  
Development of a New Velocity Model for the Paradox Valley Area

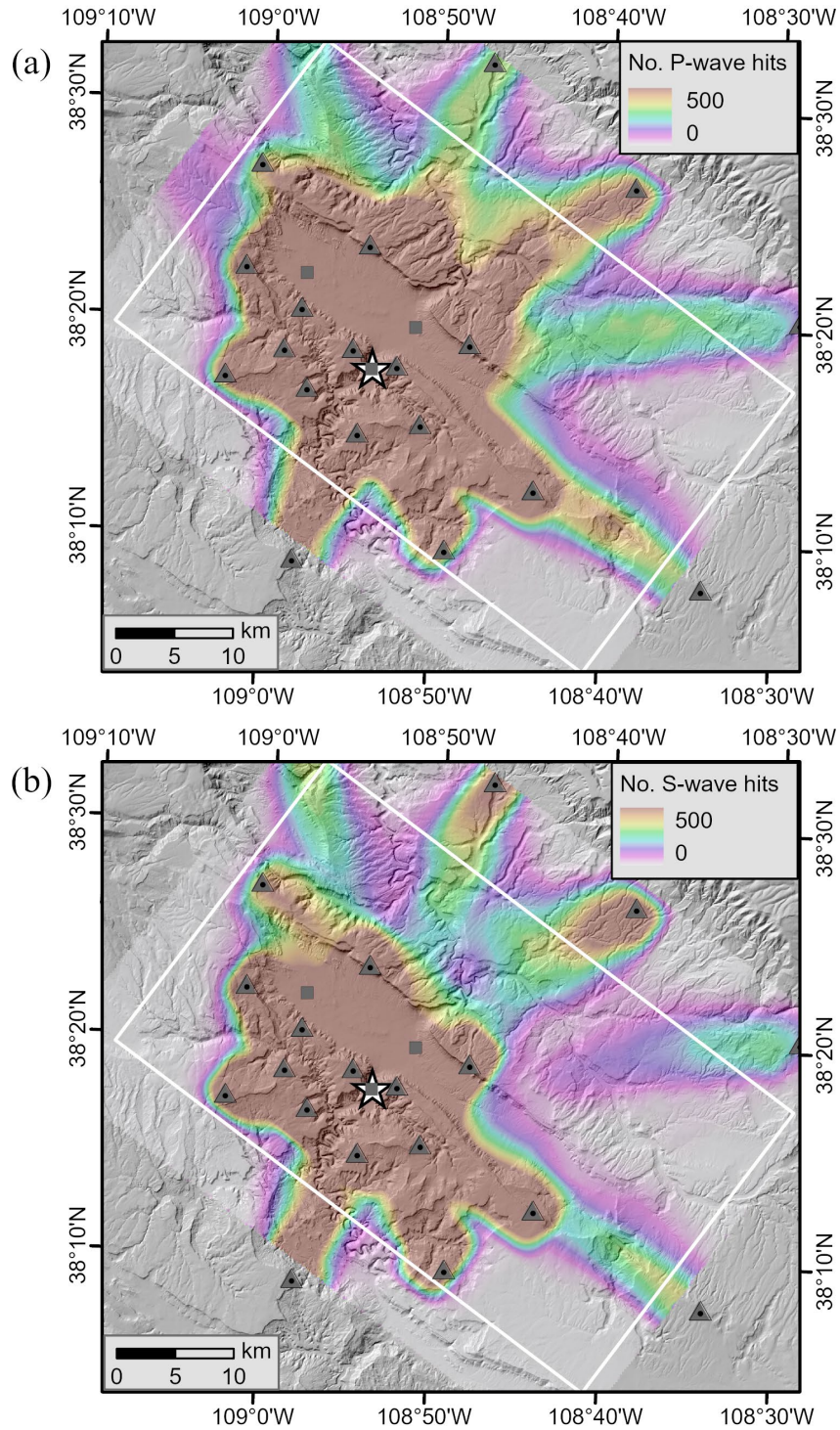


**Figure B-3: Horizontal section of the number of seismic rays (hits) for the final 3-D hypocenter-velocity inversion at an elevation of -1 km: (a) P waves (b) S waves. The white star is the location of the PVU injection well. The gray triangles are the locations of the broadband seismic stations, and the gray squares are the locations of the strong motion stations. The white rectangle is the area where velocities varied during the initial inversions.**

Technical Memorandum 86-68330-2024-7  
Development of a New Velocity Model for the Paradox Valley Area

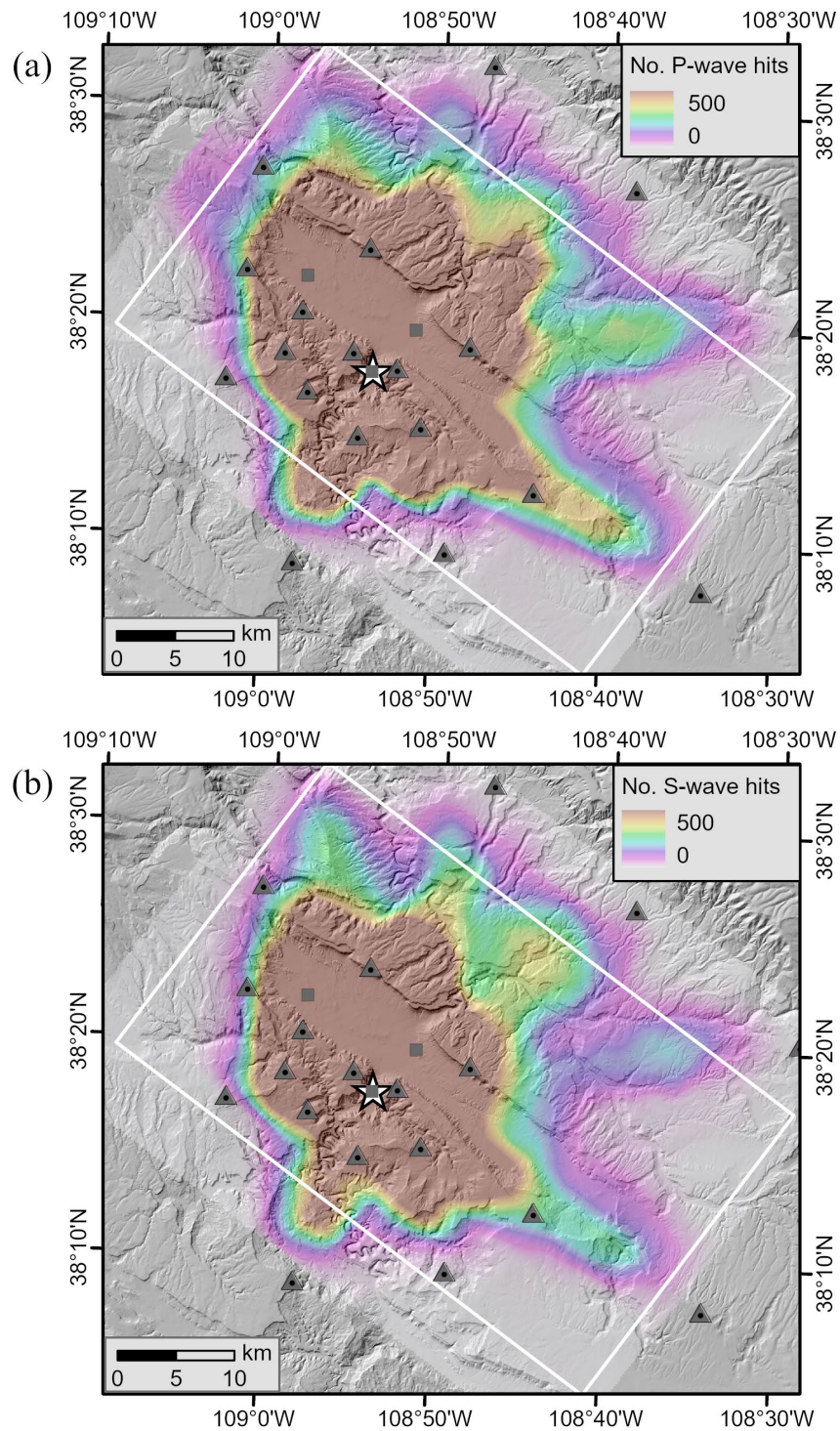


**Figure B-4: Horizontal section of the number of seismic rays (hits) for the final 3-D hypocenter-velocity inversion at an elevation of -2 km: (a) P waves (b) S waves. The white star is the location of the PVU injection well. The gray triangles are the locations of the broadband seismic stations, and the gray squares are the locations of the strong motion stations. The white rectangle is the area where velocities varied during the initial inversions.**



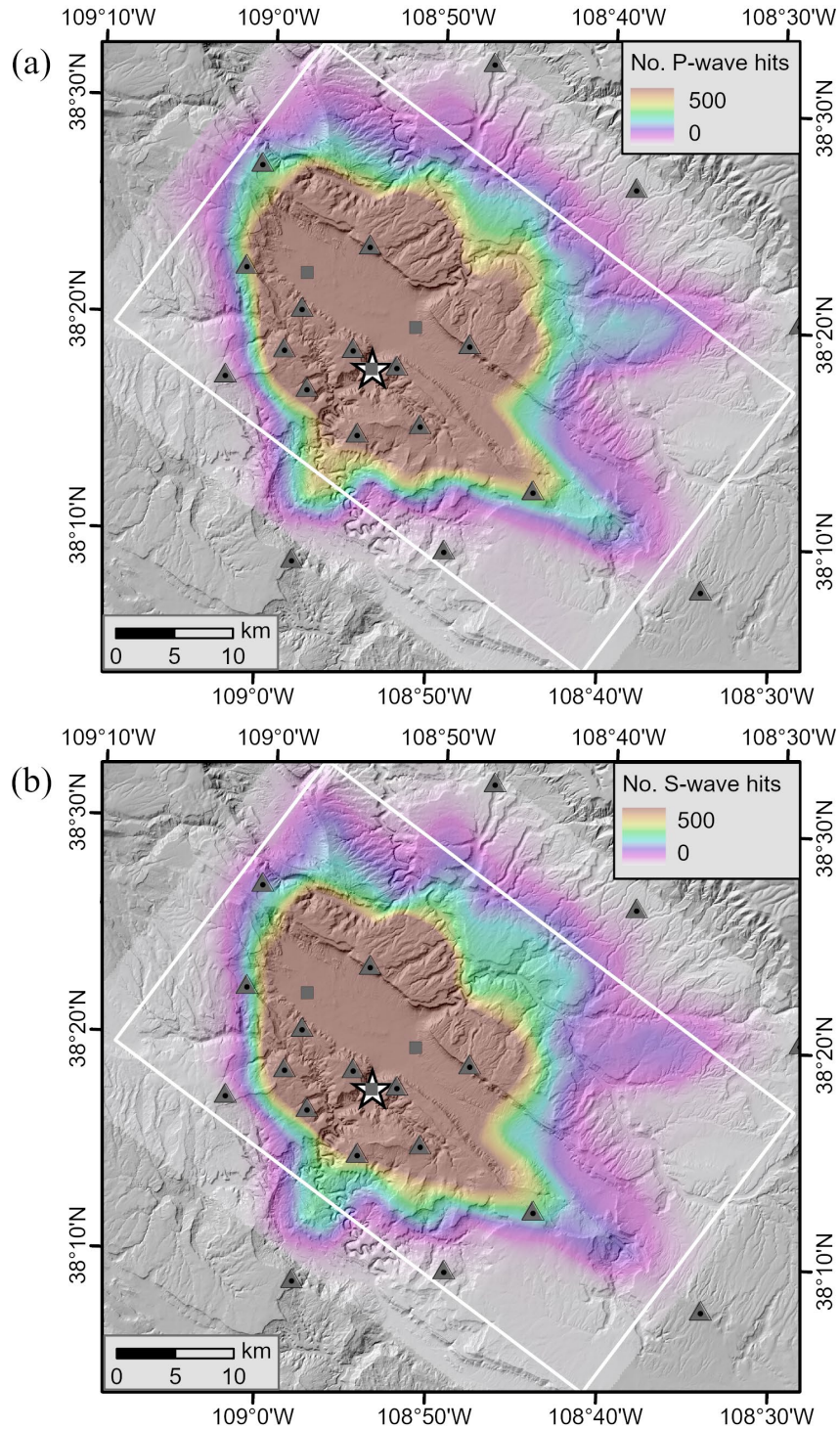


**Figure B-5: Horizontal section of the number of seismic rays (hits) for the final 3-D hypocenter-velocity inversion at an elevation of -3 km: (a) P waves (b) S waves. The white star is the location of the PVU injection well. The gray triangles are the locations of the broadband seismic stations, and the gray squares are the locations of the strong motion stations. The white rectangle is the area where velocities varied during the initial inversions.**

Technical Memorandum 86-68330-2024-7  
Development of a New Velocity Model for the Paradox Valley Area

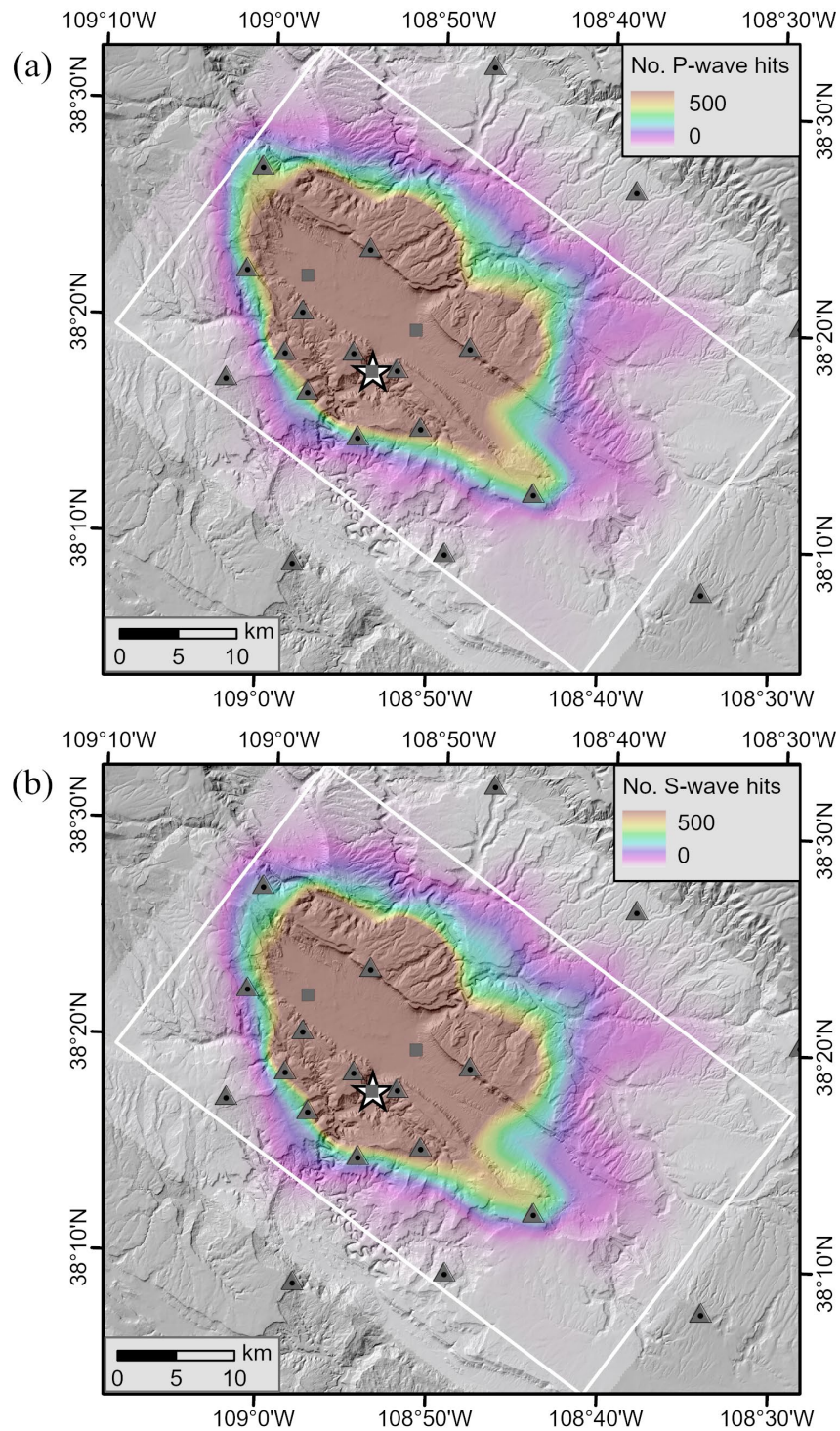


**Figure B-6: Horizontal section of the number of seismic rays (hits) for the final 3-D hypocenter-velocity inversion at an elevation of -4 km: (a) P waves (b) S waves. The white star is the location of the PVU injection well. The gray triangles are the locations of the broadband seismic stations, and the gray squares are the locations of the strong motion stations. The white rectangle is the area where velocities varied during the initial inversions.**



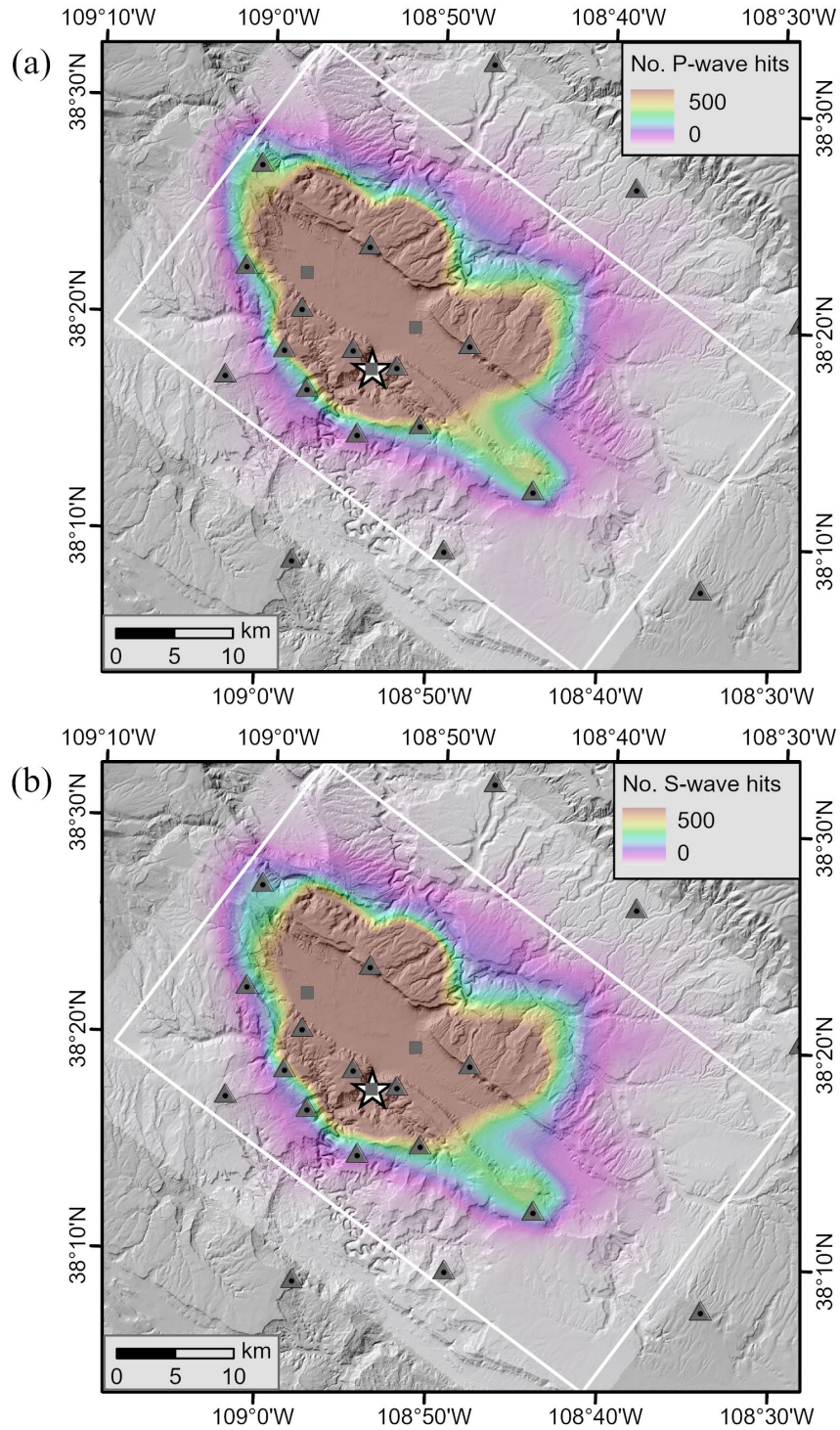


**Figure B-7: Horizontal section of the number of seismic rays (hits) for the final 3-D hypocenter-velocity inversion at an elevation of -5 km: (a) P waves (b) S waves. The white star is the location of the PVU injection well. The gray triangles are the locations of the broadband seismic stations, and the gray squares are the locations of the strong motion stations. The white rectangle is the area where velocities varied during the initial inversions.**

Technical Memorandum 86-68330-2024-7  
Development of a New Velocity Model for the Paradox Valley Area

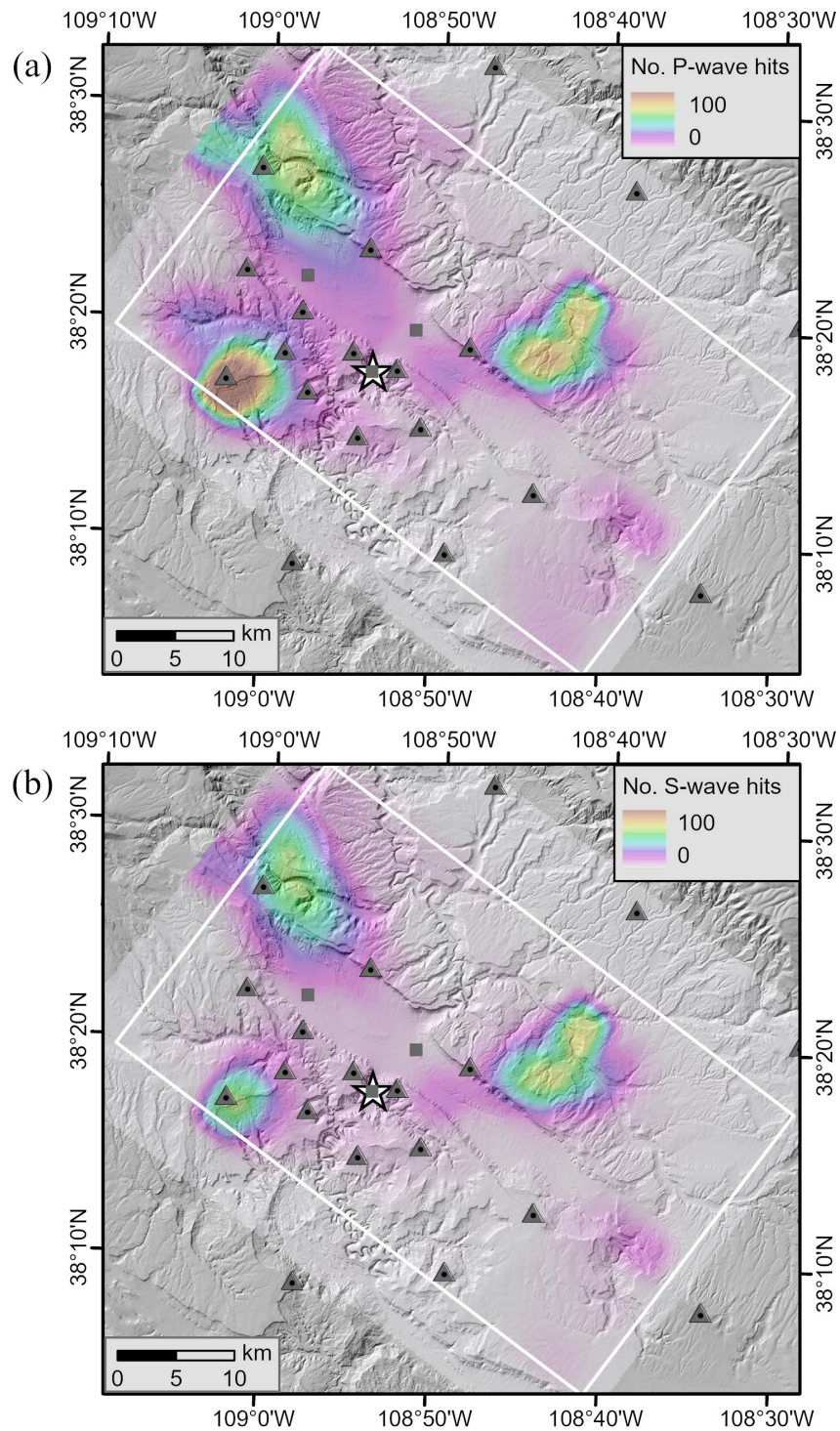


**Figure B-8: Horizontal section of the number of seismic rays (hits) for the final 3-D hypocenter-velocity inversion at an elevation of -10 km: (a) P waves (b) S waves. The white star is the location of the PVU injection well. The gray triangles are the locations of the broadband seismic stations, and the gray squares are the locations of the strong motion stations. The white rectangle is the area where velocities varied during the initial inversions.**



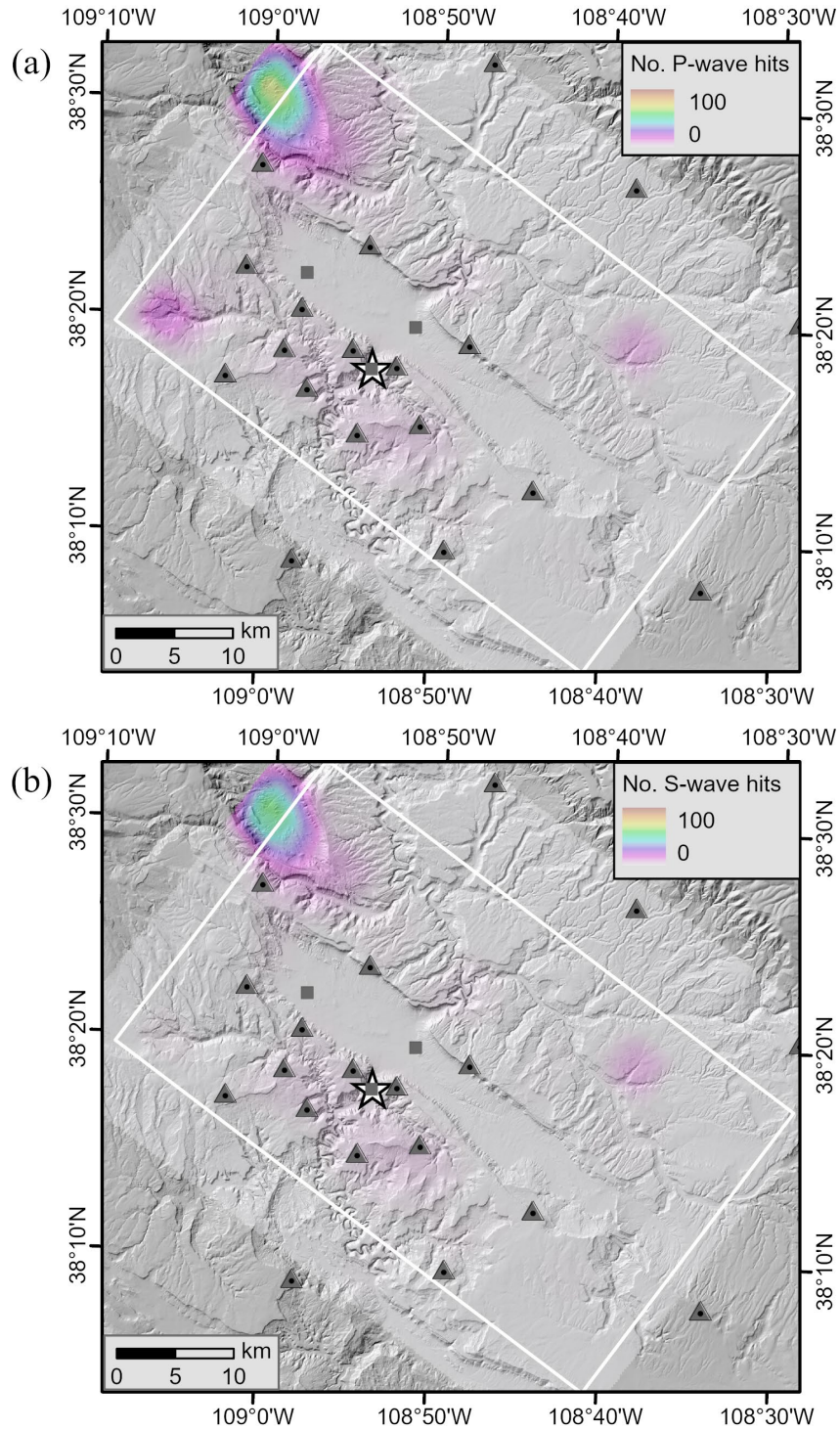


**Figure B-9: Horizontal section of the number of seismic rays (hits) for the final 3-D hypocenter-velocity inversion at an elevation of -15 km: (a) P waves (b) S waves. The white star is the location of the PVU injection well. The gray triangles are the locations of the broadband seismic stations, and the gray squares are the locations of the strong motion stations. The white rectangle is the area where velocities varied during the initial inversions.**



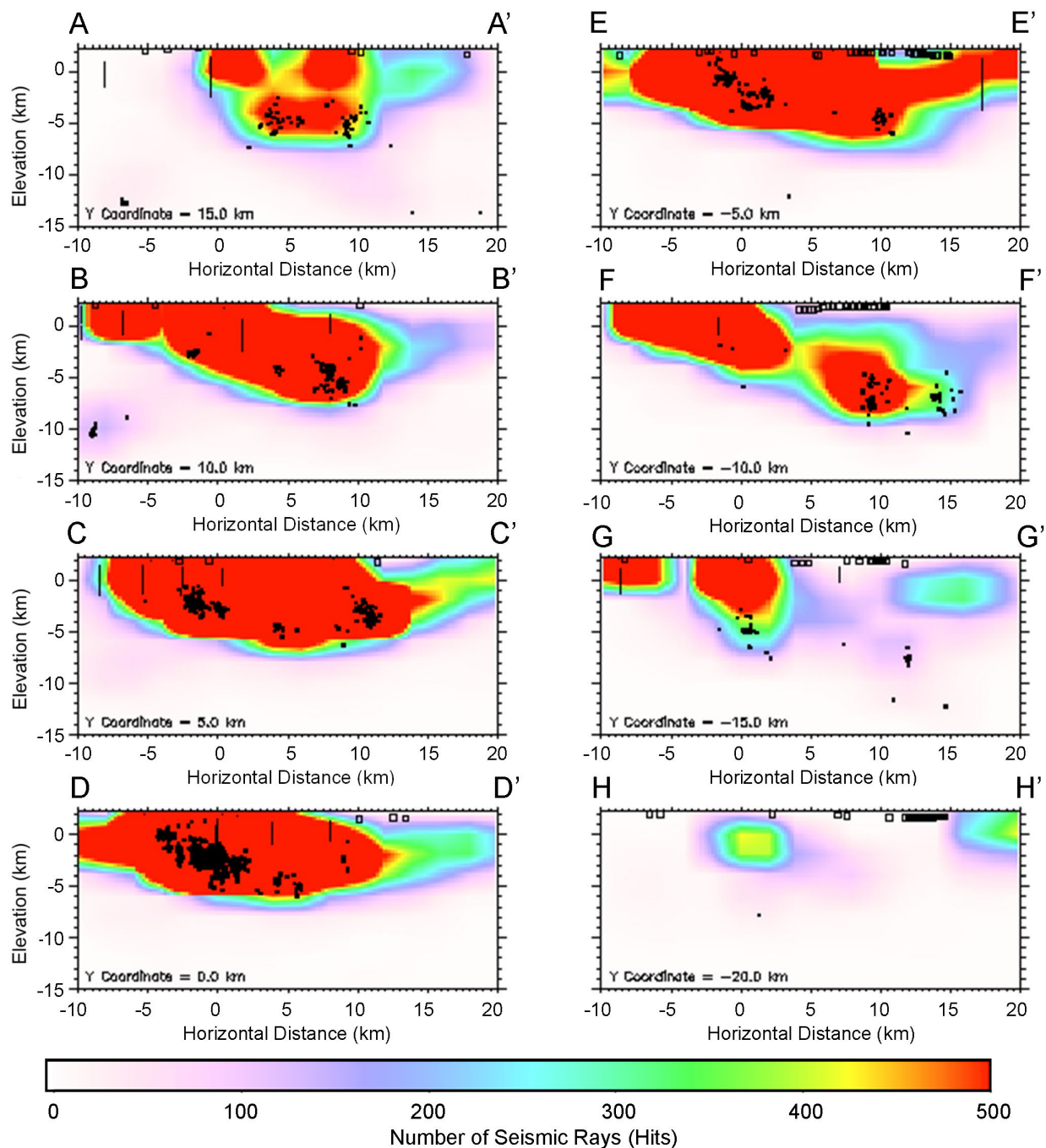


**Figure B-10: Vertical sections perpendicular to Paradox Valley of the number of P-wave rays (hits) for the final 3-D hypocenter-velocity inversion. The cross sections are spaced 5 km apart; their locations are shown in Figure 3-10 of the main report. The earthquakes (black dots), explosions (open black squares), and well log data points (black lines) within 2.5 km of each section are projected onto the sections.**

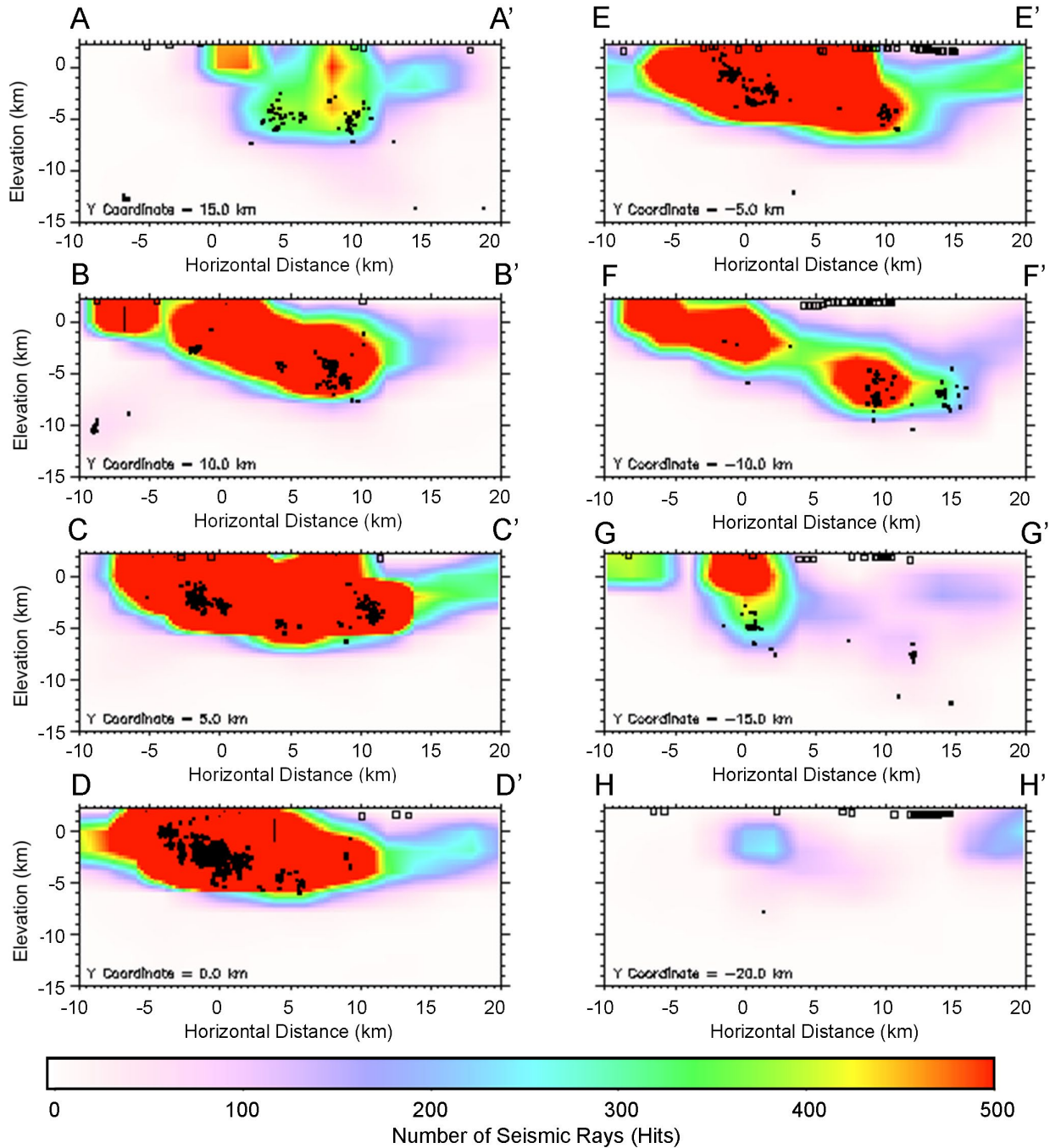


**Figure B-11: Vertical sections perpendicular to Paradox Valley of the number of S-wave rays (hits) for the final 3-D hypocenter-velocity inversion. The cross sections are spaced 5 km apart; their locations are shown in Figure 3-10 of the main report. The earthquakes (black dots), explosions (open black squares), and well log data points (black lines) within 2.5 km of each section are projected onto the sections.**

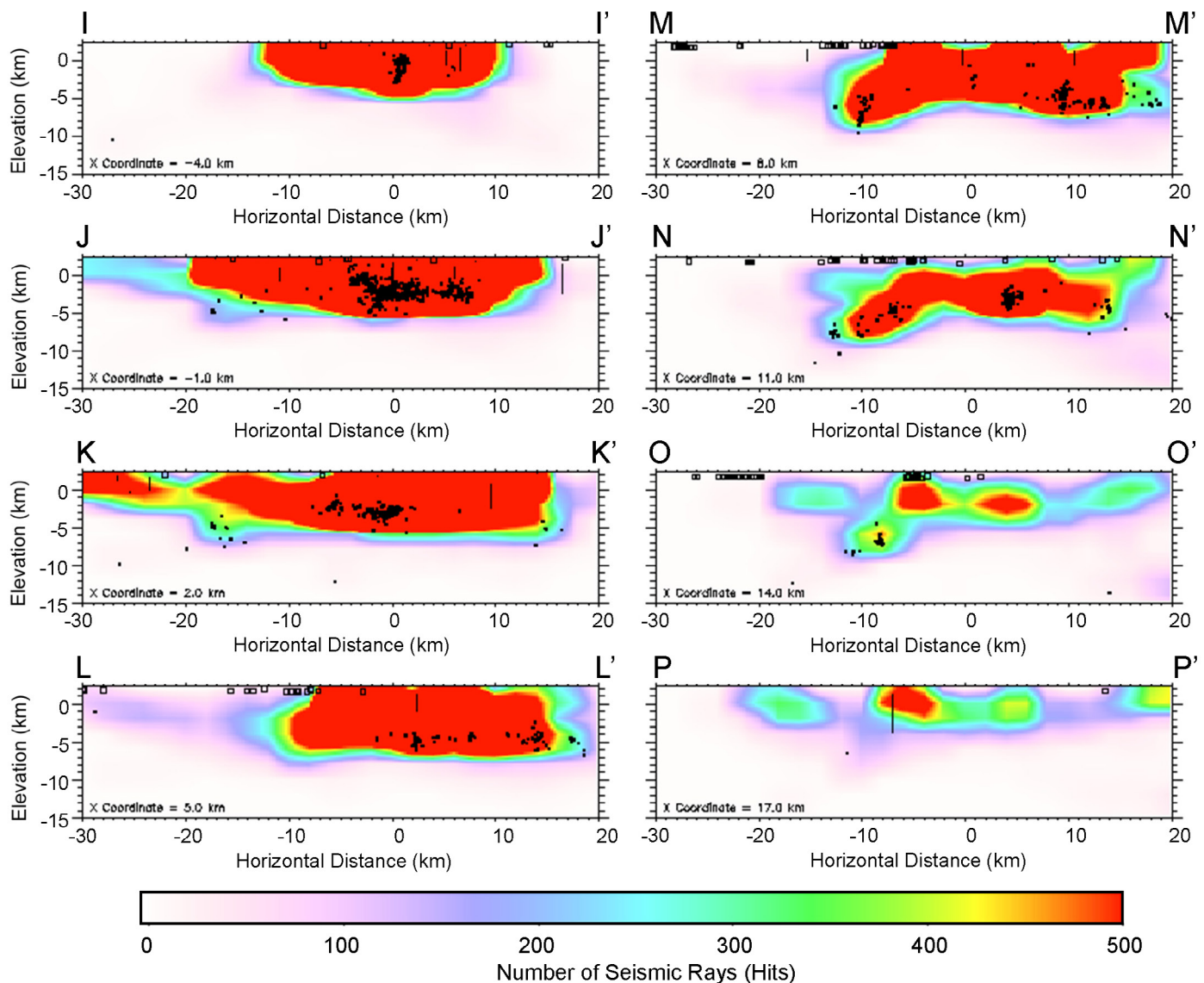


**Figure B-12: Vertical sections parallel to Paradox Valley of the number of P-wave rays (hits) for the final 3-D hypocenter-velocity inversion. The cross sections are spaced 3 km apart; their locations are shown in Figure 3-10 of the main report. The earthquakes (black dots), explosions (open black squares), and well log data points (black lines) within 1.5 km of each section are projected onto the sections.**

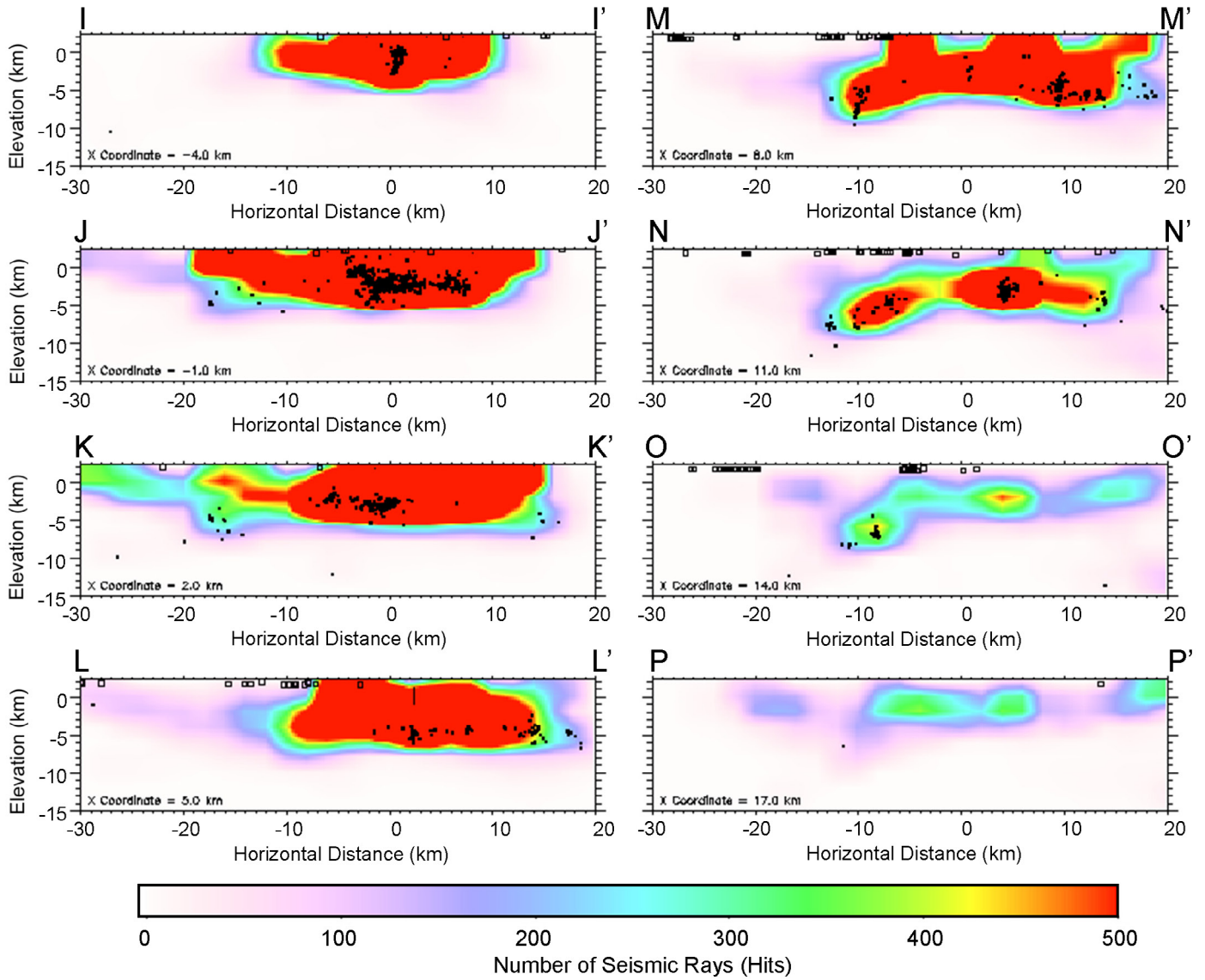


**Figure B-13: Vertical sections parallel to Paradox Valley of the number of S-wave rays (hits) for the final 3-D hypocenter-velocity inversion. The cross sections are spaced 3 km apart; their locations are shown in Figure 3-10 of the main report. The earthquakes (black dots), explosions (open black squares), and well log data points (black lines) within 1.5 km of each section are projected onto the sections.**



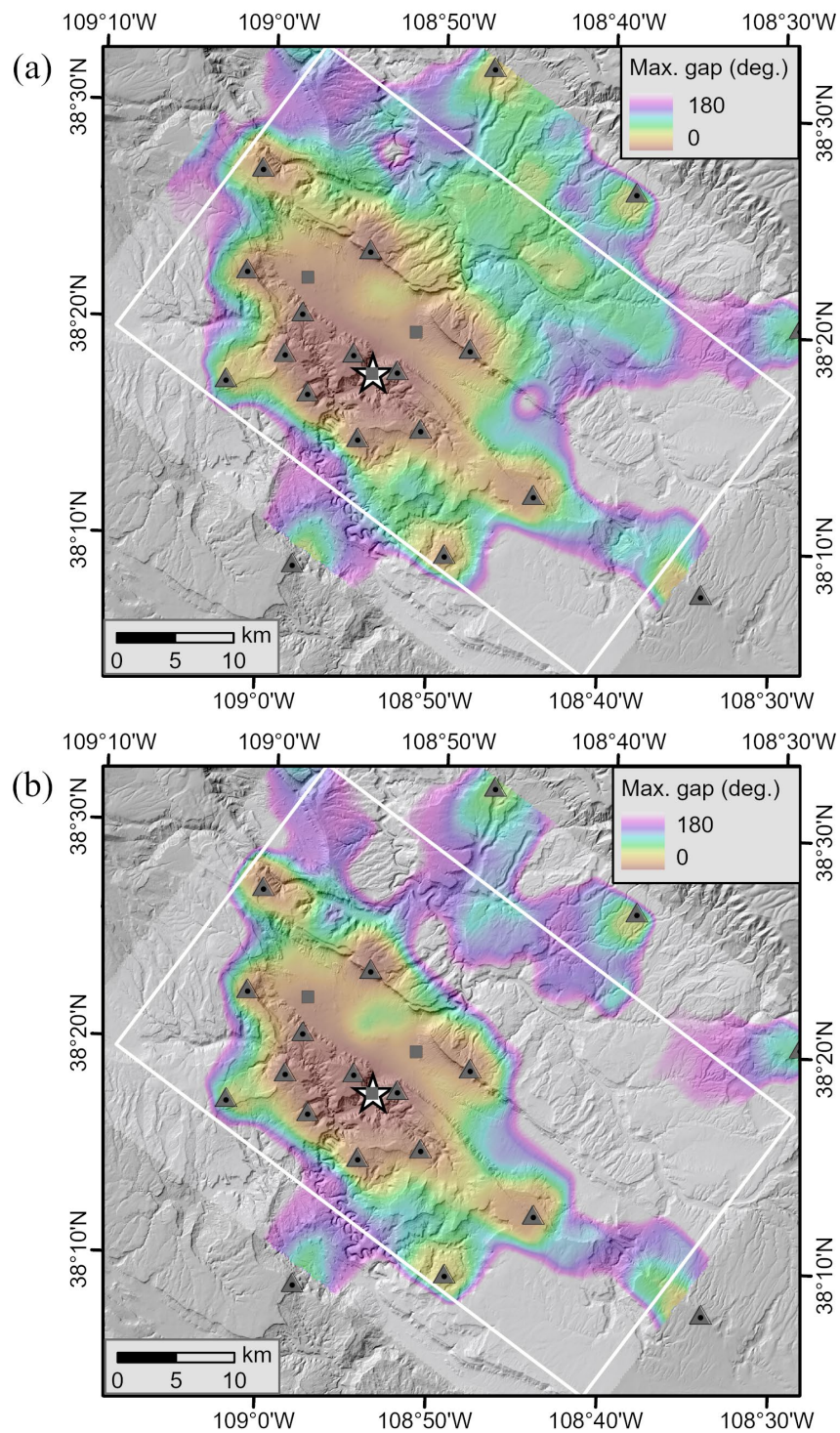


**Figure B-14: Horizontal section of the maximum gap in horizontal angular ray coverage (deg.) for the final 3-D hypocenter-velocity inversion at an elevation of 1 km: (a) P waves (b) S waves. The white star is the location of the PVU injection well. The gray triangles are the locations of the broadband seismic stations, and the gray squares are the locations of the strong motion stations. The white rectangle is the area where velocities varied during the initial inversions.**

Technical Memorandum 86-68330-2024-7  
Development of a New Velocity Model for the Paradox Valley Area

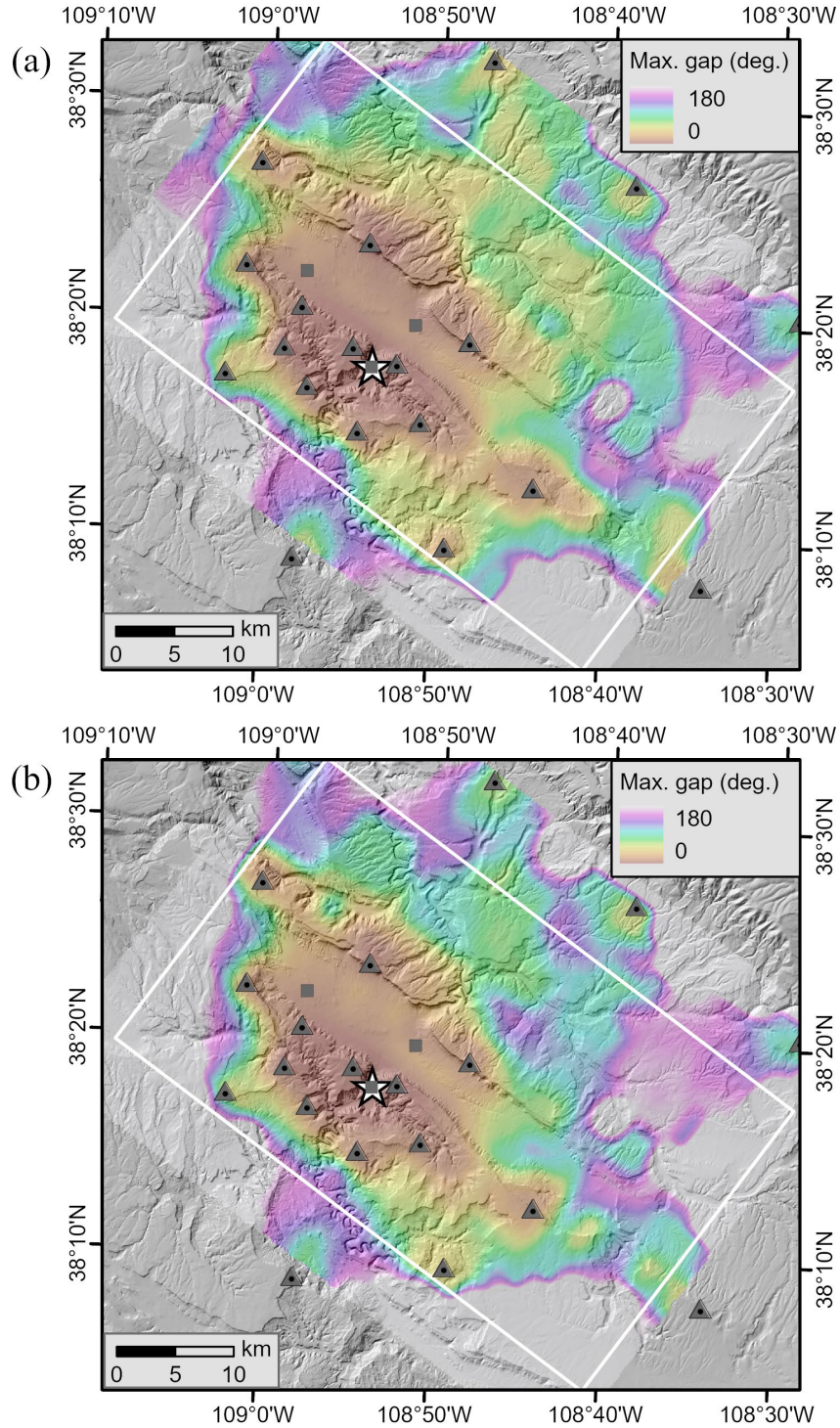


**Figure B-15: Horizontal section of the maximum gap in horizontal angular ray coverage (deg.) for the final 3-D hypocenter-velocity inversion at an elevation of 0 km: (a) P waves (b) S waves. The white star is the location of the PVU injection well. The gray triangles are the locations of the broadband seismic stations, and the gray squares are the locations of the strong motion stations. The white rectangle is the area where velocities varied during the initial inversions.**



Development of a New Velocity Model for the Paradox Valley Area

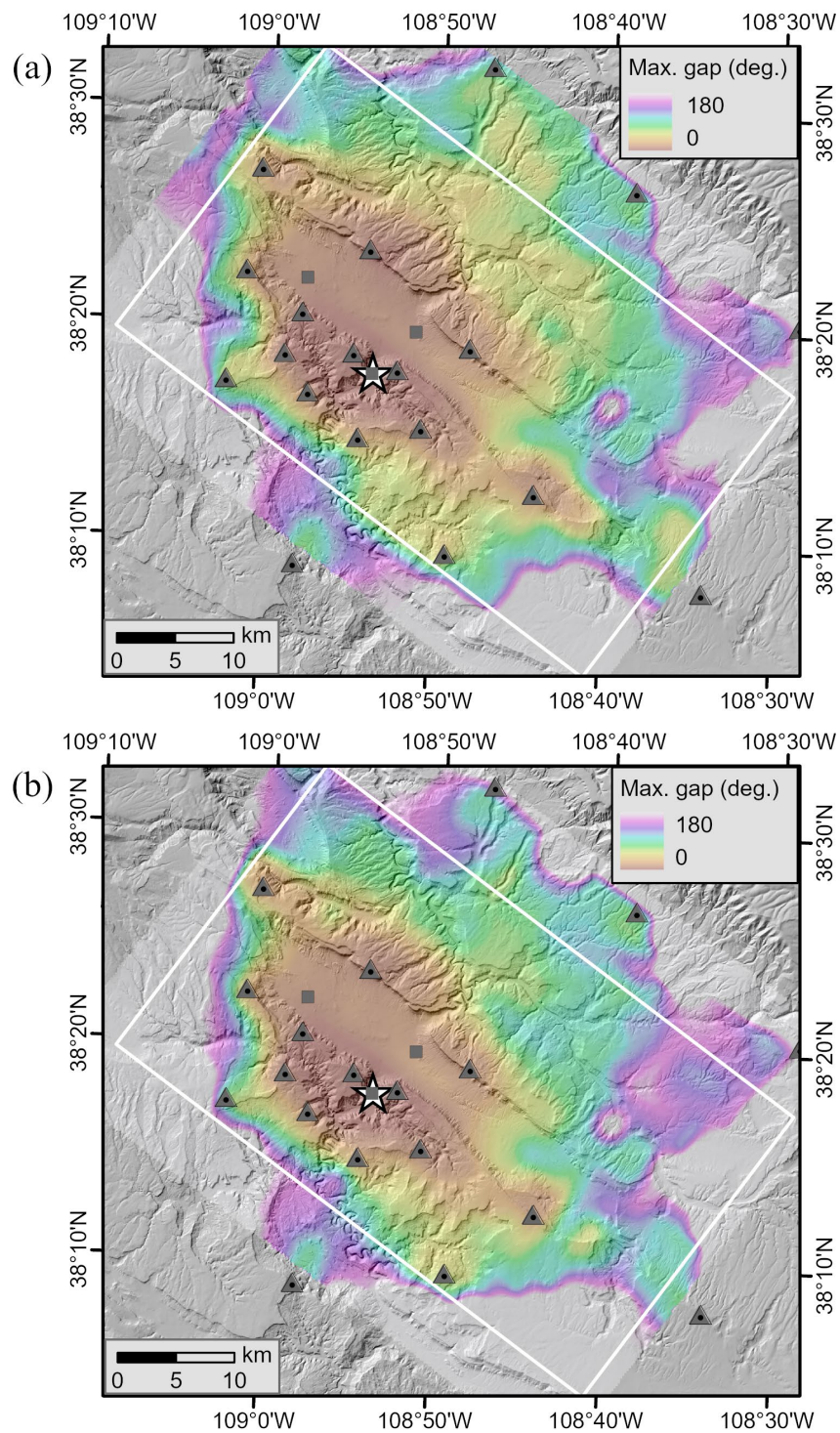


**Figure B-16: Horizontal section of the maximum gap in horizontal angular ray coverage (deg.) for the final 3-D hypocenter-velocity inversion at an elevation of -1 km: (a) P waves (b) S waves. The white star is the location of the PVU injection well. The gray triangles are the locations of the broadband seismic stations, and the gray squares are the locations of the strong motion stations. The white rectangle is the area where velocities varied during the initial inversions.**

Technical Memorandum 86-68330-2024-7  
Development of a New Velocity Model for the Paradox Valley Area

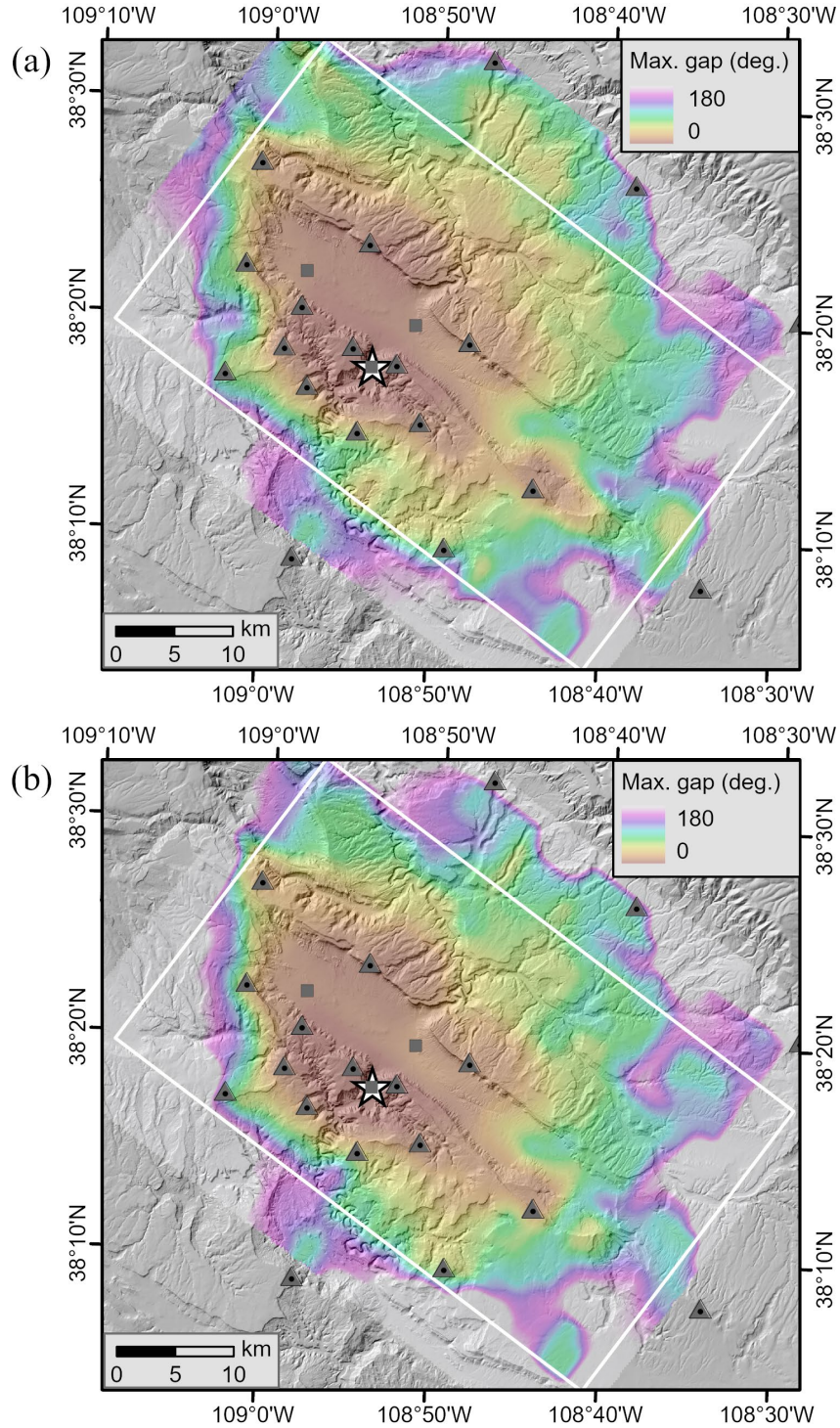


**Figure B-17: Horizontal section of the maximum gap in horizontal angular ray coverage (deg.) for the final 3-D hypocenter-velocity inversion at an elevation of -2 km: (a) P waves (b) S waves. The white star is the location of the PVU injection well. The gray triangles are the locations of the broadband seismic stations, and the gray squares are the locations of the strong motion stations. The white rectangle is the area where velocities varied during the initial inversions.**



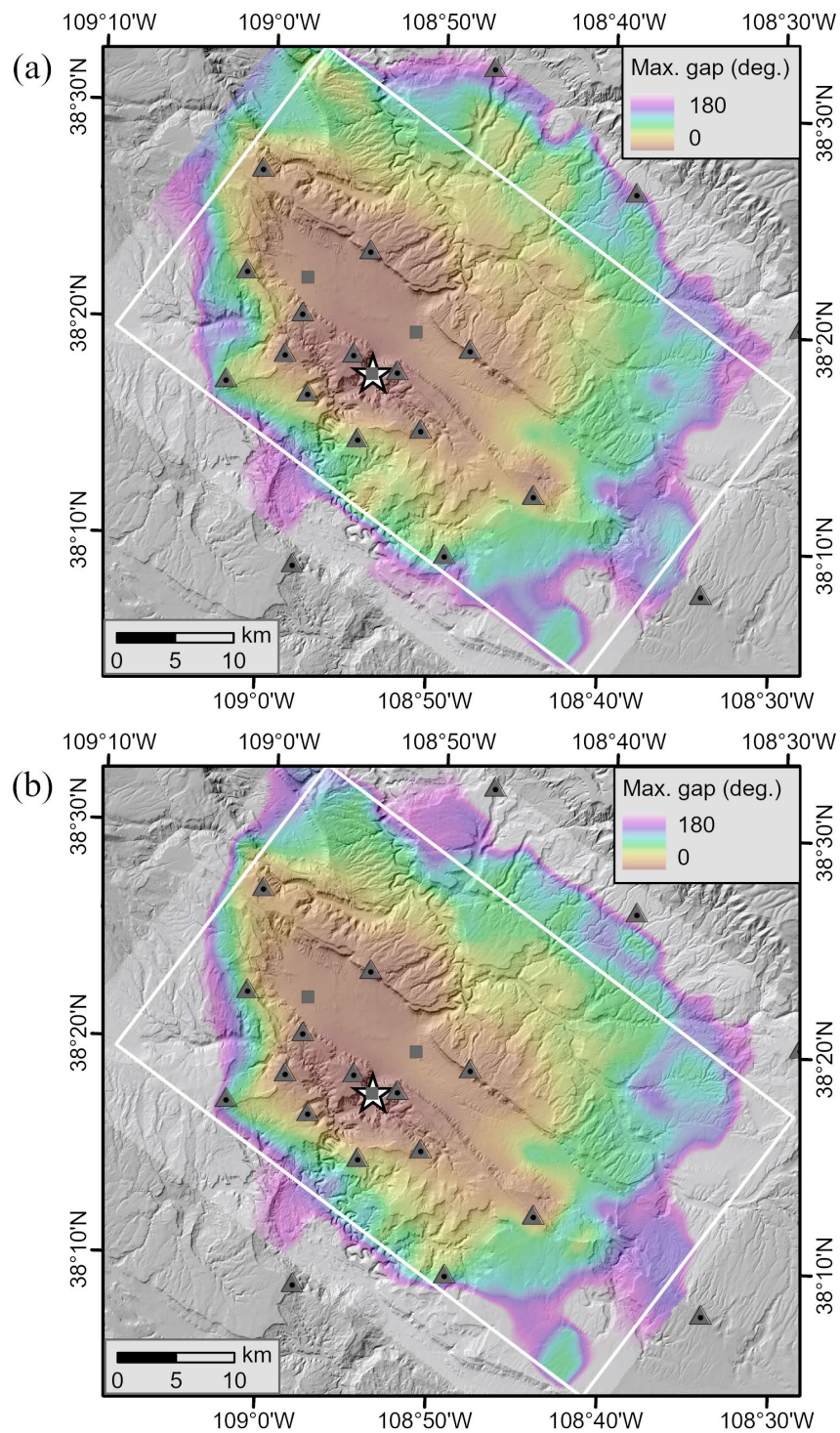


**Figure B-18: Horizontal section of the maximum gap in horizontal angular ray coverage (deg.) for the final 3-D hypocenter-velocity inversion at an elevation of -3 km: (a) P waves (b) S waves. The white star is the location of the PVU injection well. The gray triangles are the locations of the broadband seismic stations, and the gray squares are the locations of the strong motion stations. The white rectangle is the area where velocities varied during the initial inversions.**

Technical Memorandum 86-68330-2024-7  
Development of a New Velocity Model for the Paradox Valley Area

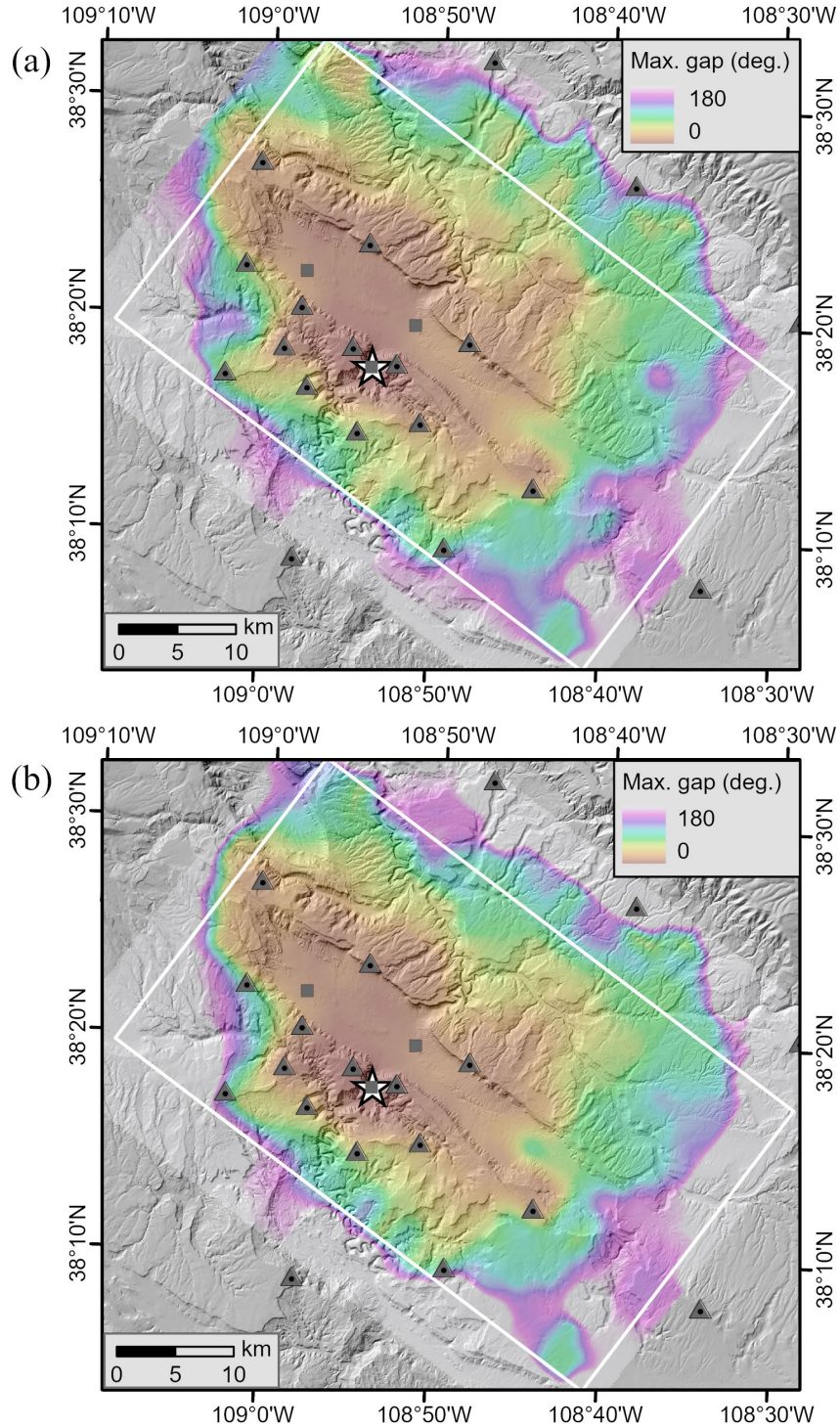


**Figure B-19: Horizontal section of the maximum gap in horizontal angular ray coverage (deg.) for the final 3-D hypocenter-velocity inversion at an elevation of -4 km: (a) P waves (b) S waves. The white star is the location of the PVU injection well. The gray triangles are the locations of the broadband seismic stations, and the gray squares are the locations of the strong motion stations. The white rectangle is the area where velocities varied during the initial inversions.**



Development of a New Velocity Model for the Paradox Valley Area

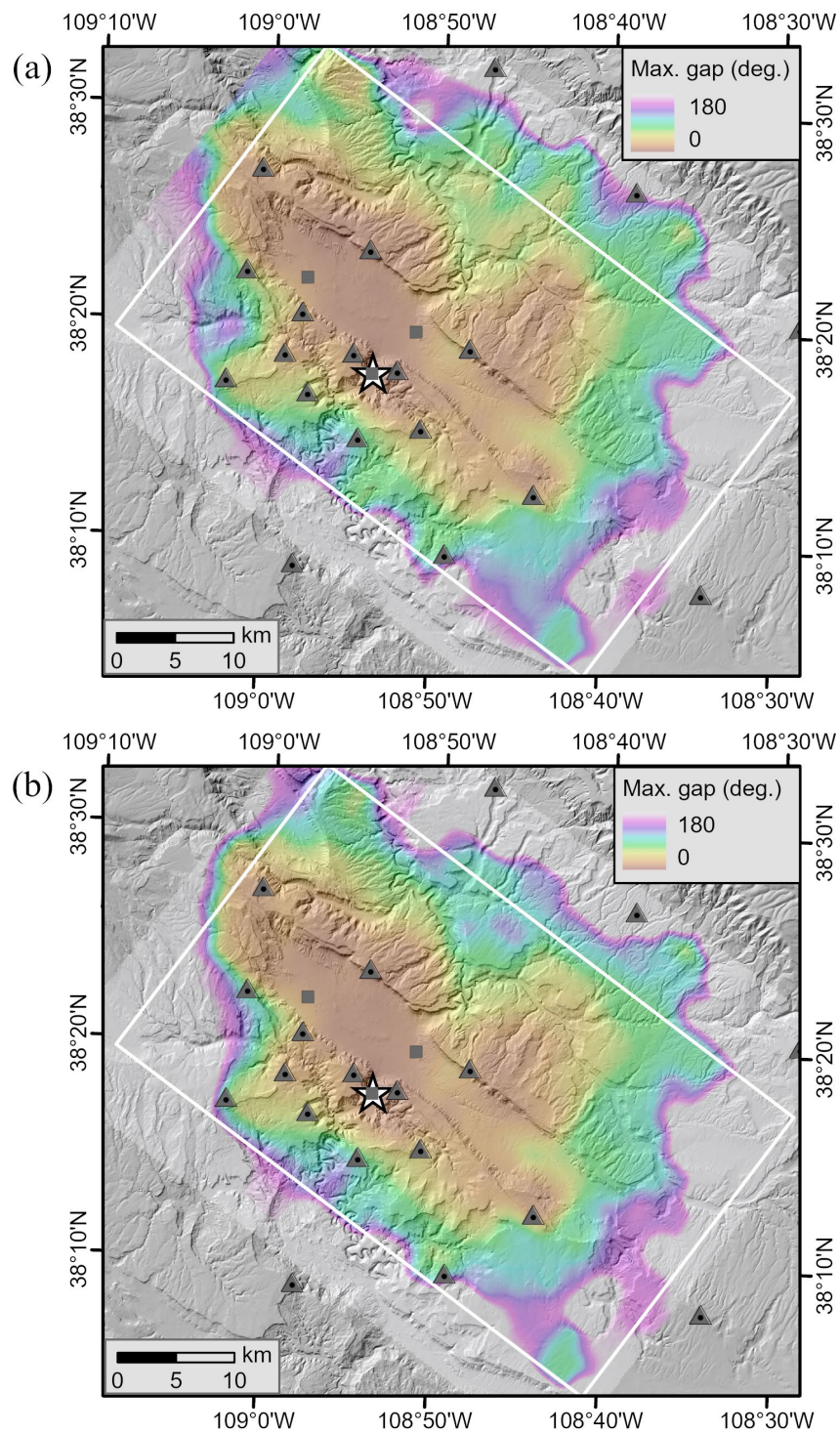


**Figure B-20: Horizontal section of the maximum gap in horizontal angular ray coverage (deg.) for the final 3-D hypocenter-velocity inversion at an elevation of -5 km: (a) P waves (b) S waves. The white star is the location of the PVU injection well. The gray triangles are the locations of the broadband seismic stations, and the gray squares are the locations of the strong motion stations. The white rectangle is the area where velocities varied during the initial inversions.**

Technical Memorandum 86-68330-2024-7  
Development of a New Velocity Model for the Paradox Valley Area

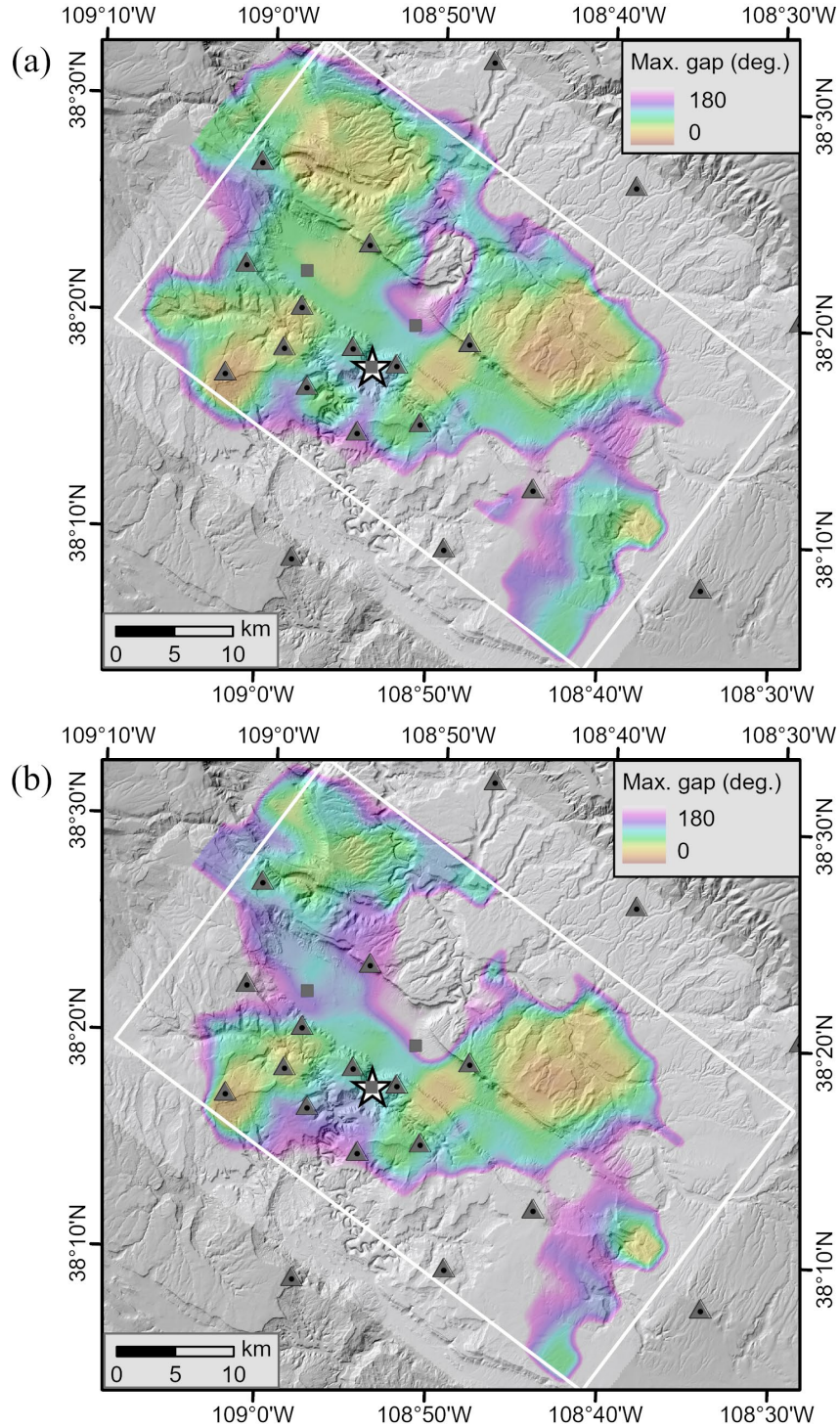


**Figure B-21: Horizontal section of the maximum gap in horizontal angular ray coverage (deg.) for the final 3-D hypocenter-velocity inversion at an elevation of -10 km: (a) P waves (b) S waves. The white star is the location of the PVU injection well. The gray triangles are the locations of the broadband seismic stations, and the gray squares are the locations of the strong motion stations. The white rectangle is the area where velocities varied during the initial inversions.**



Development of a New Velocity Model for the Paradox Valley Area

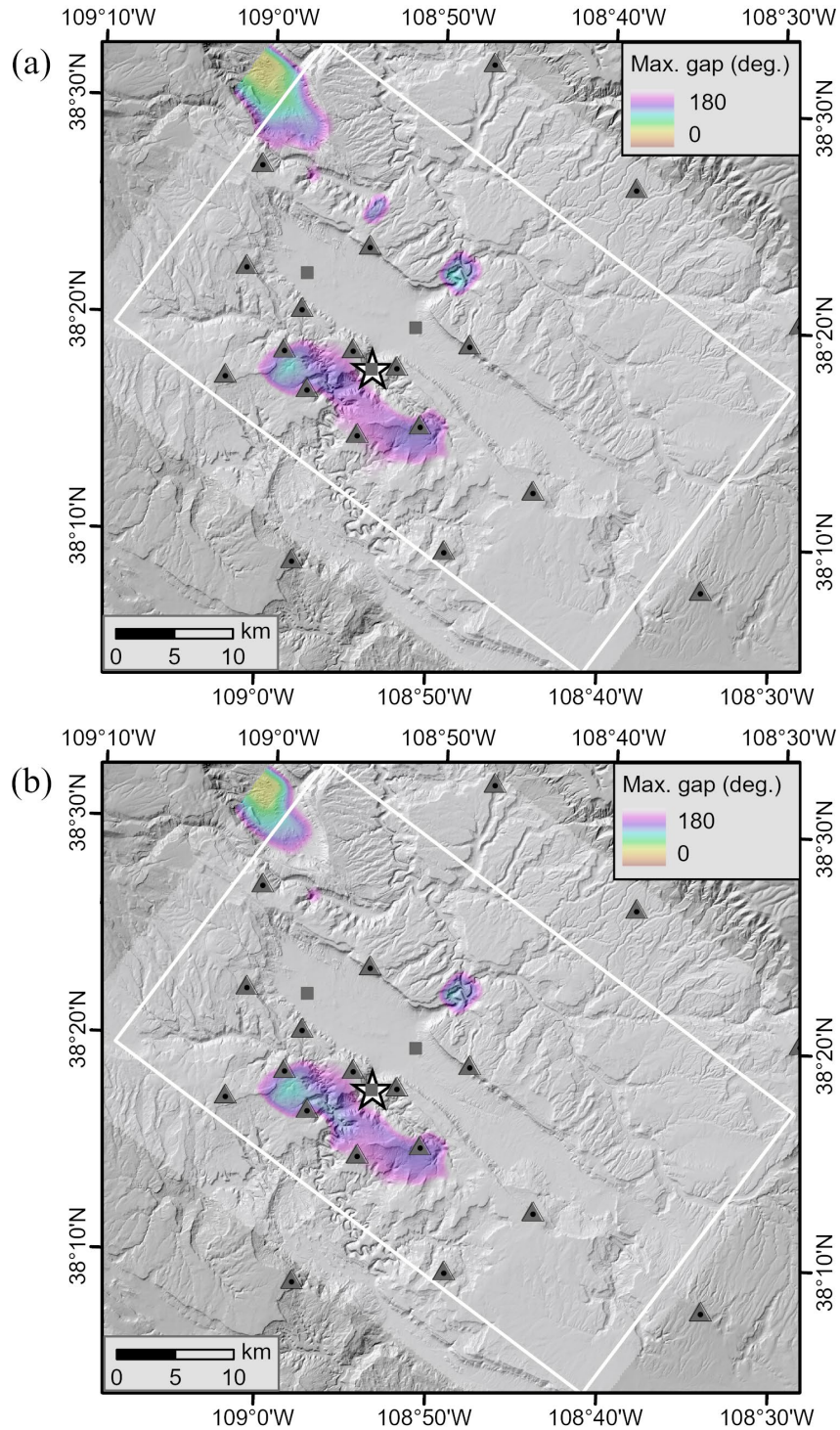


**Figure B-22: Horizontal section of the maximum gap in horizontal angular ray coverage (deg.) for the final 3-D hypocenter-velocity inversion at an elevation of -15 km: (a) P waves (b) S waves. The white star is the location of the PVU injection well. The gray triangles are the locations of the broadband seismic stations, and the gray squares are the locations of the strong motion stations. The white rectangle is the area where velocities varied during the initial inversions.**

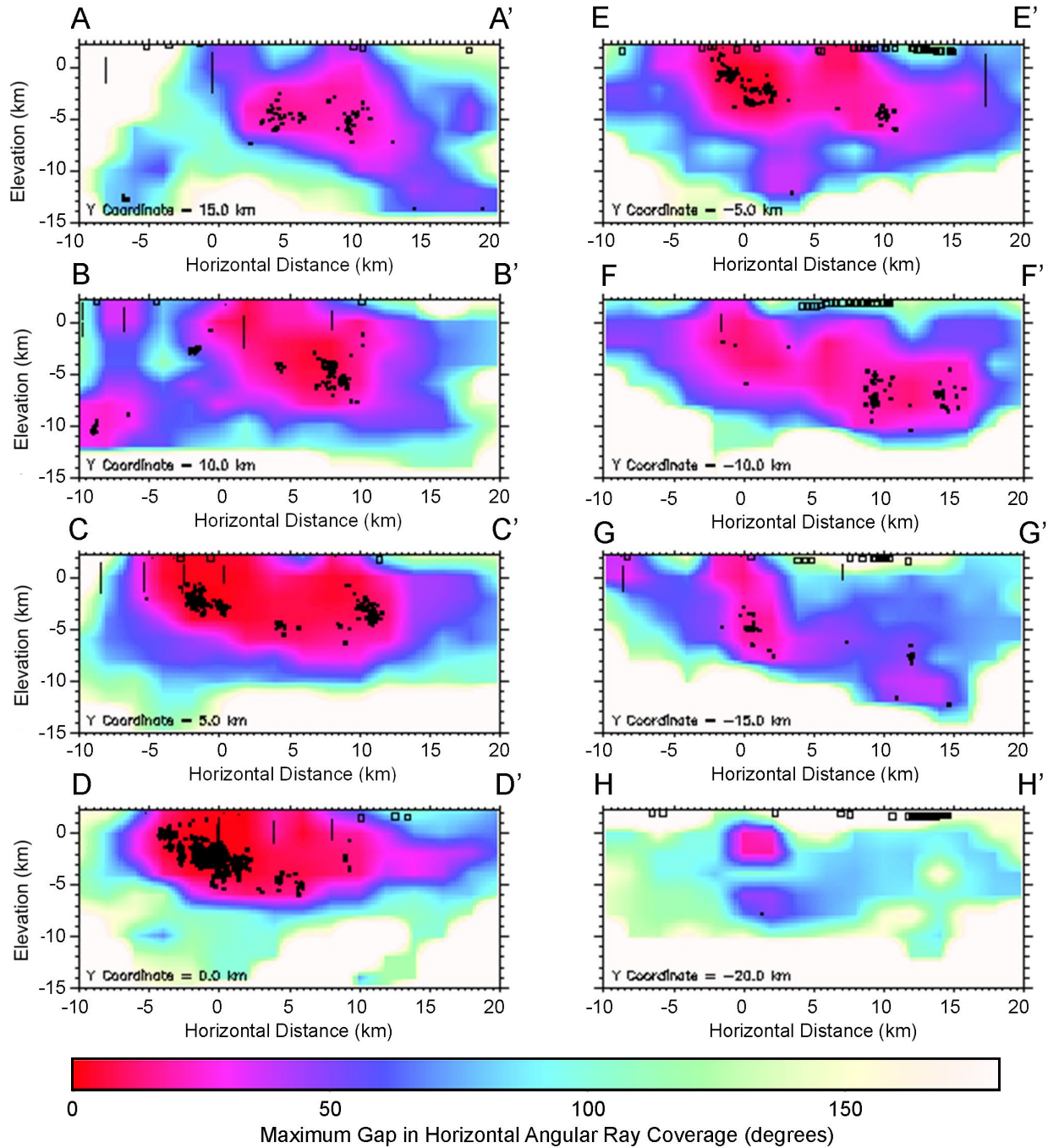


**Figure B-23: Vertical sections perpendicular to Paradox Valley of the maximum gap in P-wave horizontal angular ray coverage (deg.) for the final 3-D hypocenter-velocity inversion. The cross sections are spaced 5 km apart; their locations are shown in Figure 3-10 of the main report. The earthquakes (black dots), explosions (open black squares), and well log data points (black lines) within 2.5 km of each section are projected onto the sections.**



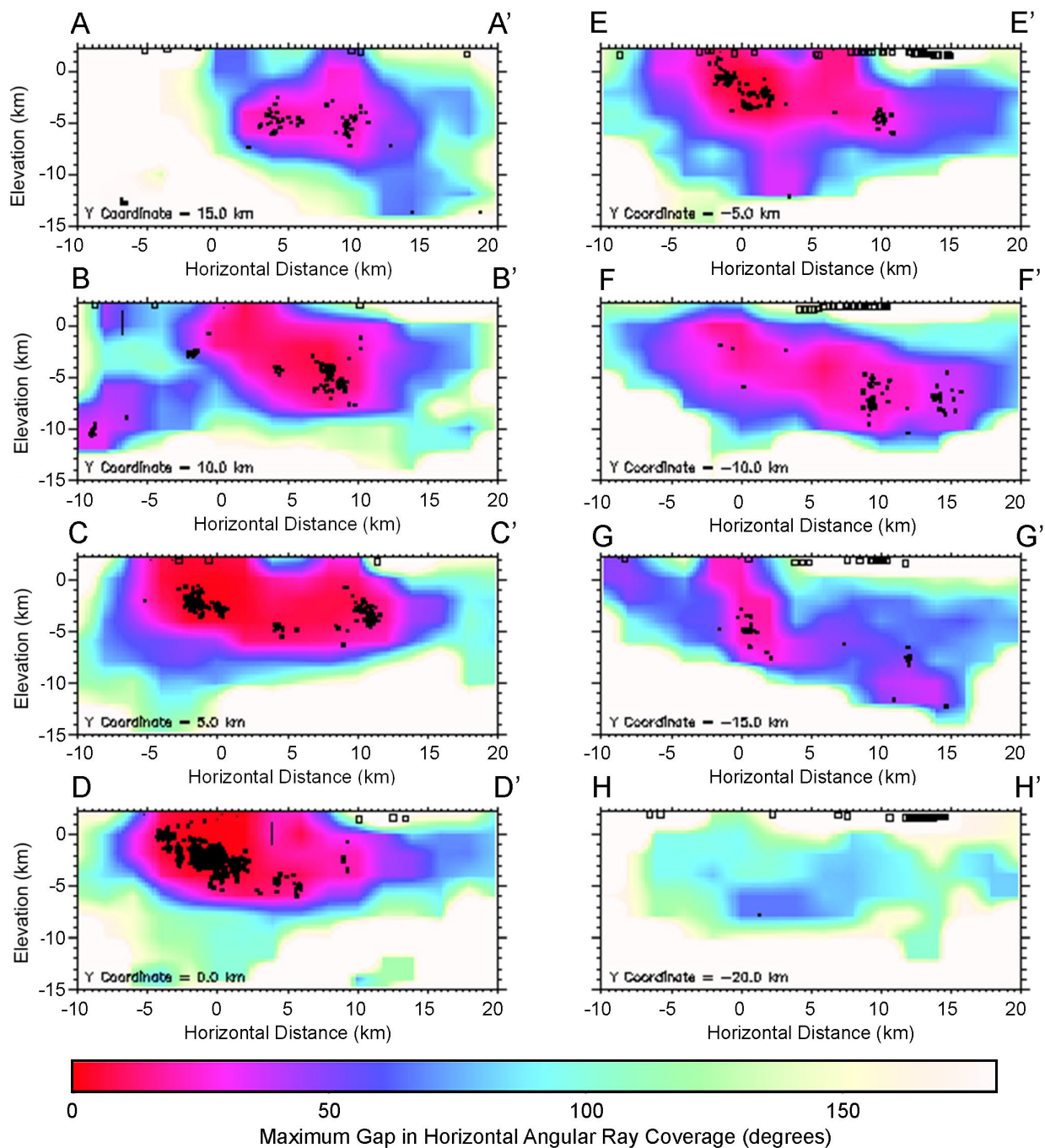


**Figure B-24: Vertical sections perpendicular to Paradox Valley of the maximum gap in S-wave horizontal angular ray coverage (deg.) for the final 3-D hypocenter-velocity inversion. The cross sections are spaced 5 km apart; their locations are shown in Figure 3-10 of the main report. The earthquakes (black dots), explosions (open black squares), and well log data points (black lines) within 2.5 km of each section are projected onto the sections.**

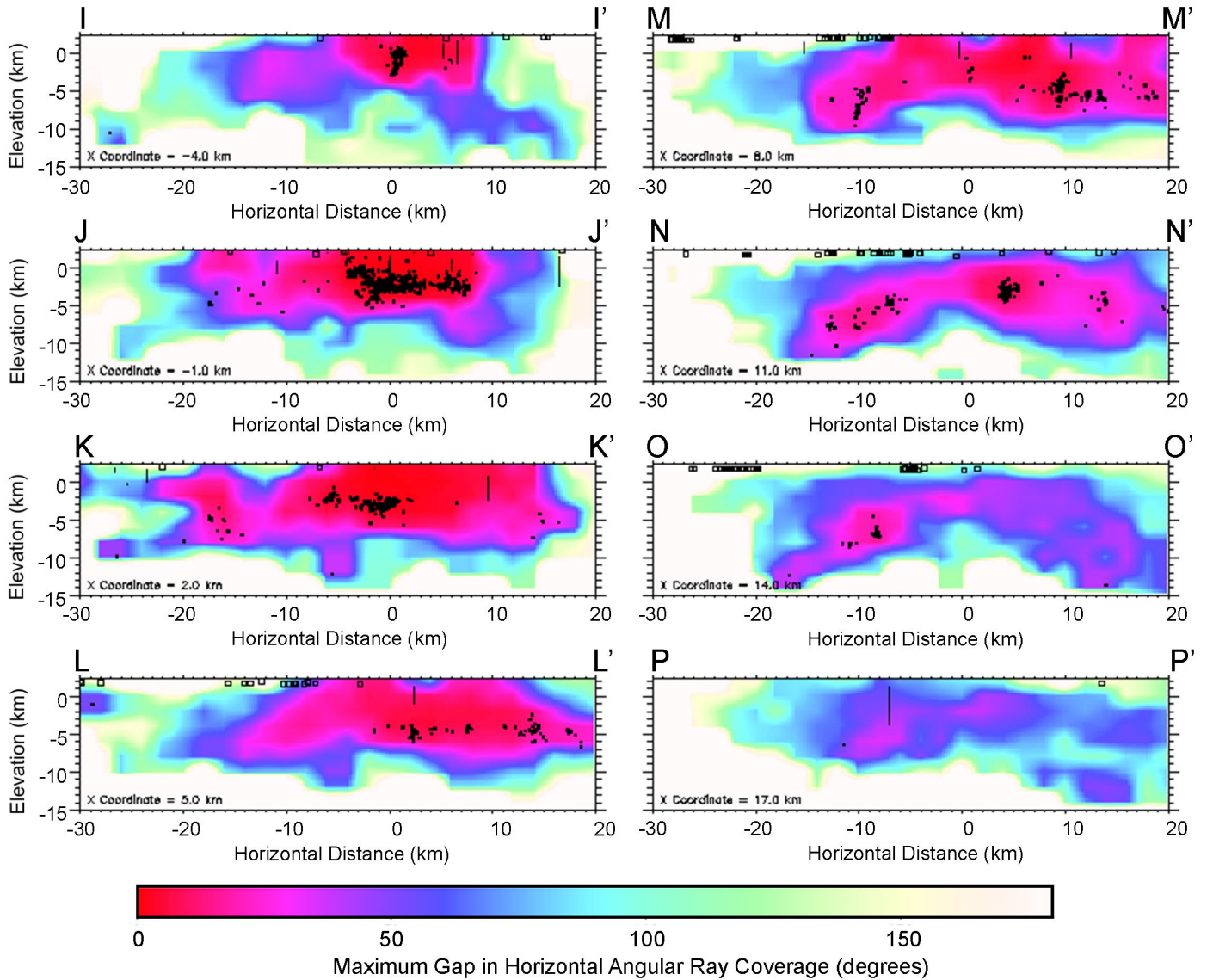


**Figure B-25: Vertical sections parallel to Paradox Valley of the maximum gap in P-wave horizontal angular ray coverage (deg.) for the final 3-D hypocenter-velocity inversion. The cross sections are spaced 3 km apart; their locations are shown in Figure 3-10 of the main report. The earthquakes (black dots), explosions (open black squares), and well log data points (black lines) within 1.5 km of each section are projected onto the sections.**



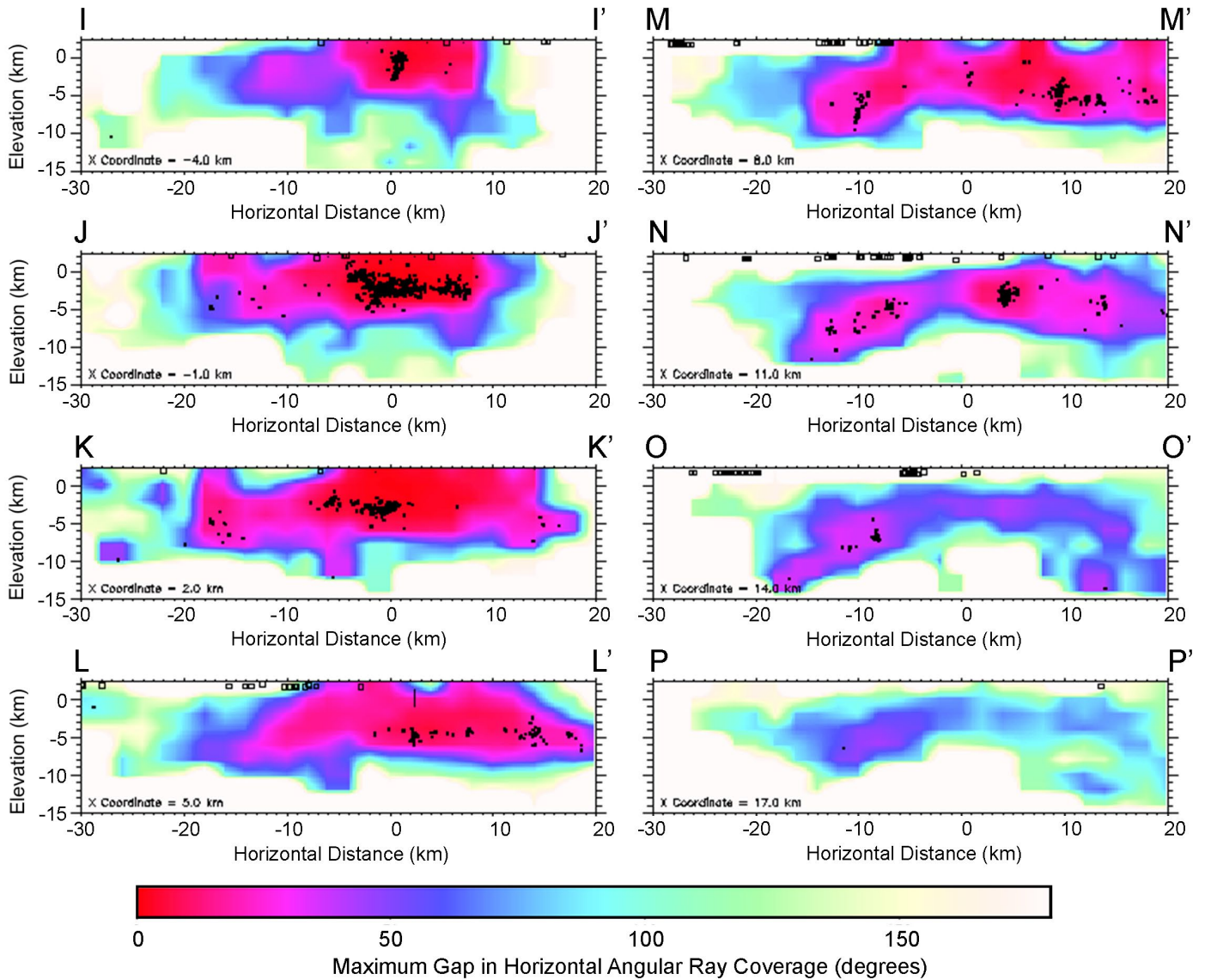


**Figure B-26: Vertical sections parallel to Paradox Valley of the maximum gap in S-wave horizontal angular ray coverage (deg.) for the final 3-D hypocenter-velocity inversion. The cross sections are spaced 3 km apart; their locations are shown in Figure 3-10 of the main report. The earthquakes (black dots), explosions (open black squares), and well log data points (black lines) within 1.5 km of each section are projected onto the sections.**

Technical Memorandum 86-68330-2024-7  
Development of a New Velocity Model for the Paradox Valley Area

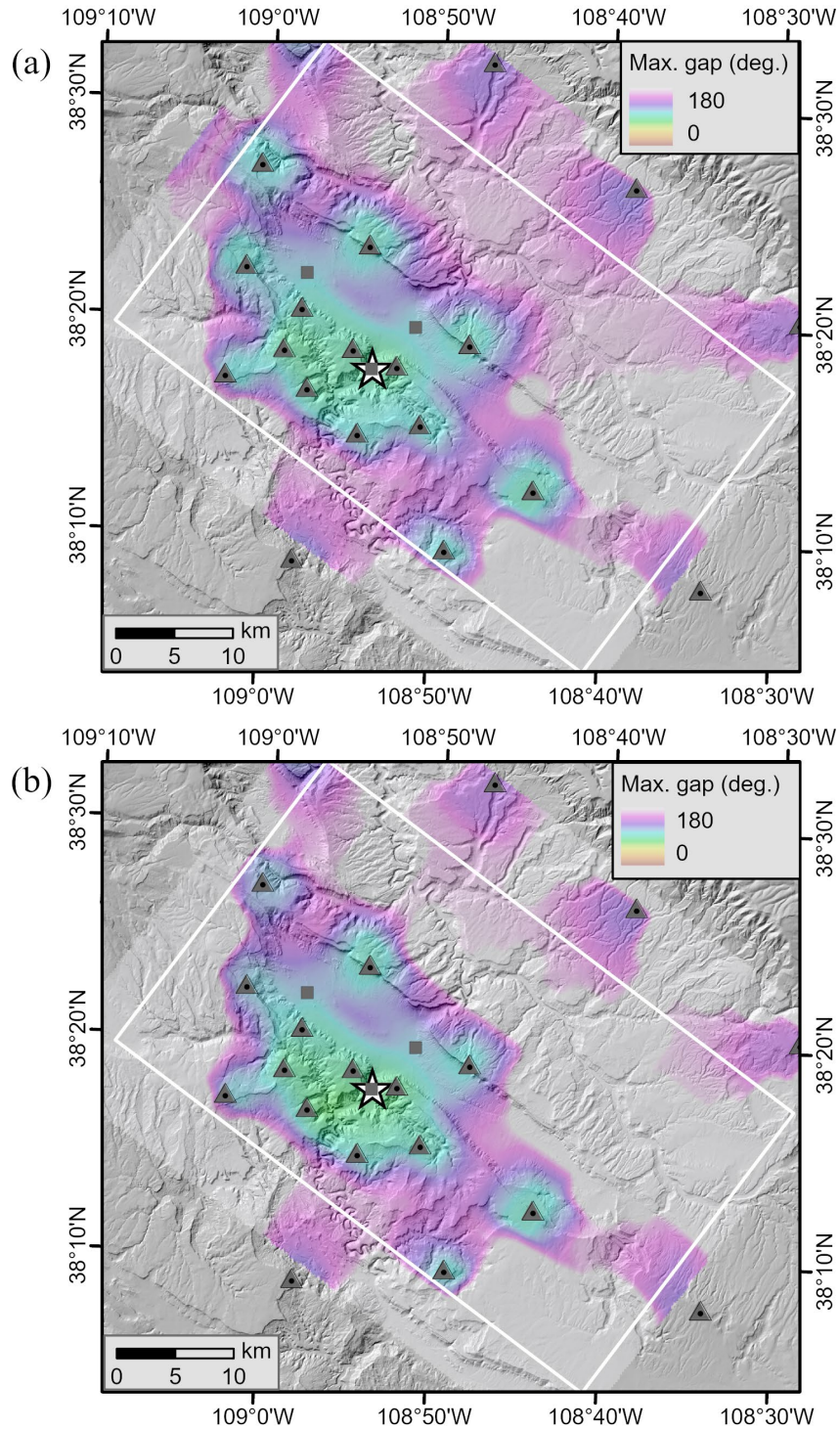


**Figure B-27: Horizontal section of the maximum gap in vertical angular ray coverage (deg.) for the final 3-D hypocenter-velocity inversion at an elevation of 1 km: (a) P waves (b) S waves. The white star is the location of the PVU injection well. The gray triangles are the locations of the broadband seismic stations, and the gray squares are the locations of the strong motion stations. The white rectangle is the area where velocities varied during the initial inversions.**



Technical Memorandum 86-68330-2024-7  
Development of a New Velocity Model for the Paradox Valley Area

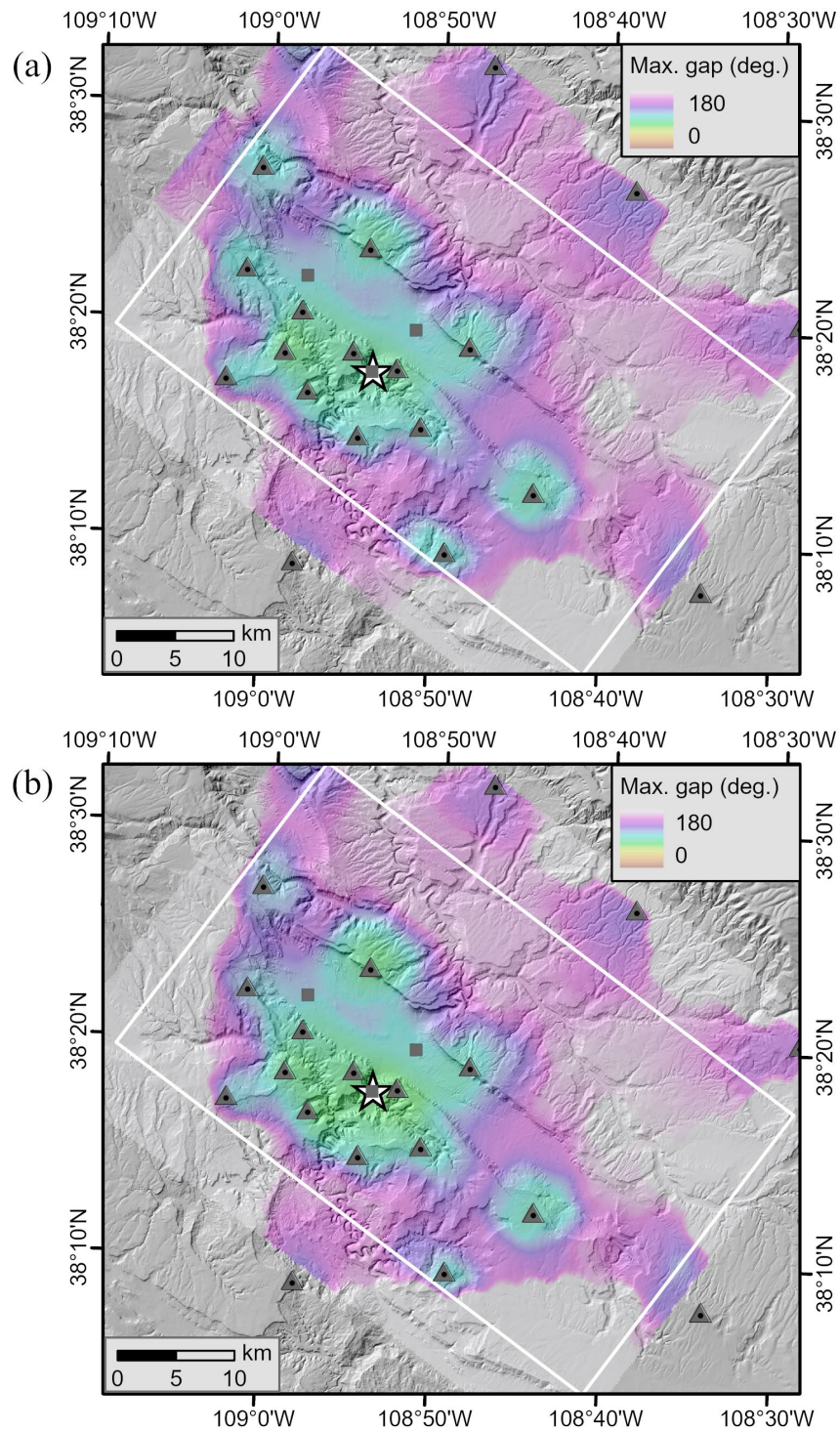


**Figure B-28: Horizontal section of the maximum gap in vertical angular ray coverage (deg.) for the final 3-D hypocenter-velocity inversion at an elevation of 0 km: (a) P waves (b) S waves. The white star is the location of the PVU injection well. The gray triangles are the locations of the broadband seismic stations, and the gray squares are the locations of the strong motion stations. The white rectangle is the area where velocities varied during the initial inversions.**

Technical Memorandum 86-68330-2024-7  
Development of a New Velocity Model for the Paradox Valley Area

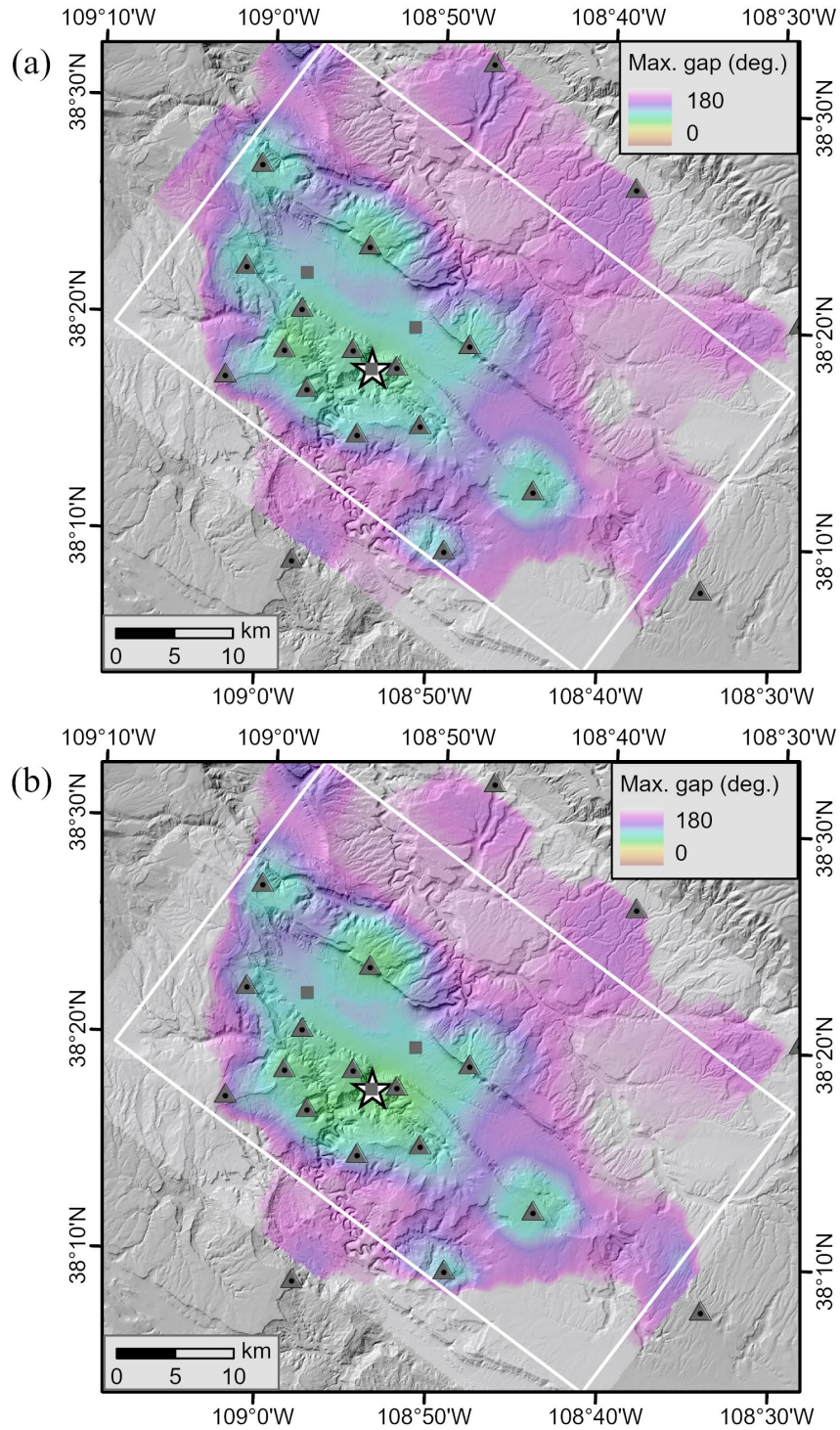


**Figure B-29: Horizontal section of the maximum gap in vertical angular ray coverage (deg.) for the final 3-D hypocenter-velocity inversion at an elevation of -1 km: (a) P waves (b) S waves. The white star is the location of the PVU injection well. The gray triangles are the locations of the broadband seismic stations, and the gray squares are the locations of the strong motion stations. The white rectangle is the area where velocities varied during the initial inversions.**



Technical Memorandum 86-68330-2024-7  
Development of a New Velocity Model for the Paradox Valley Area

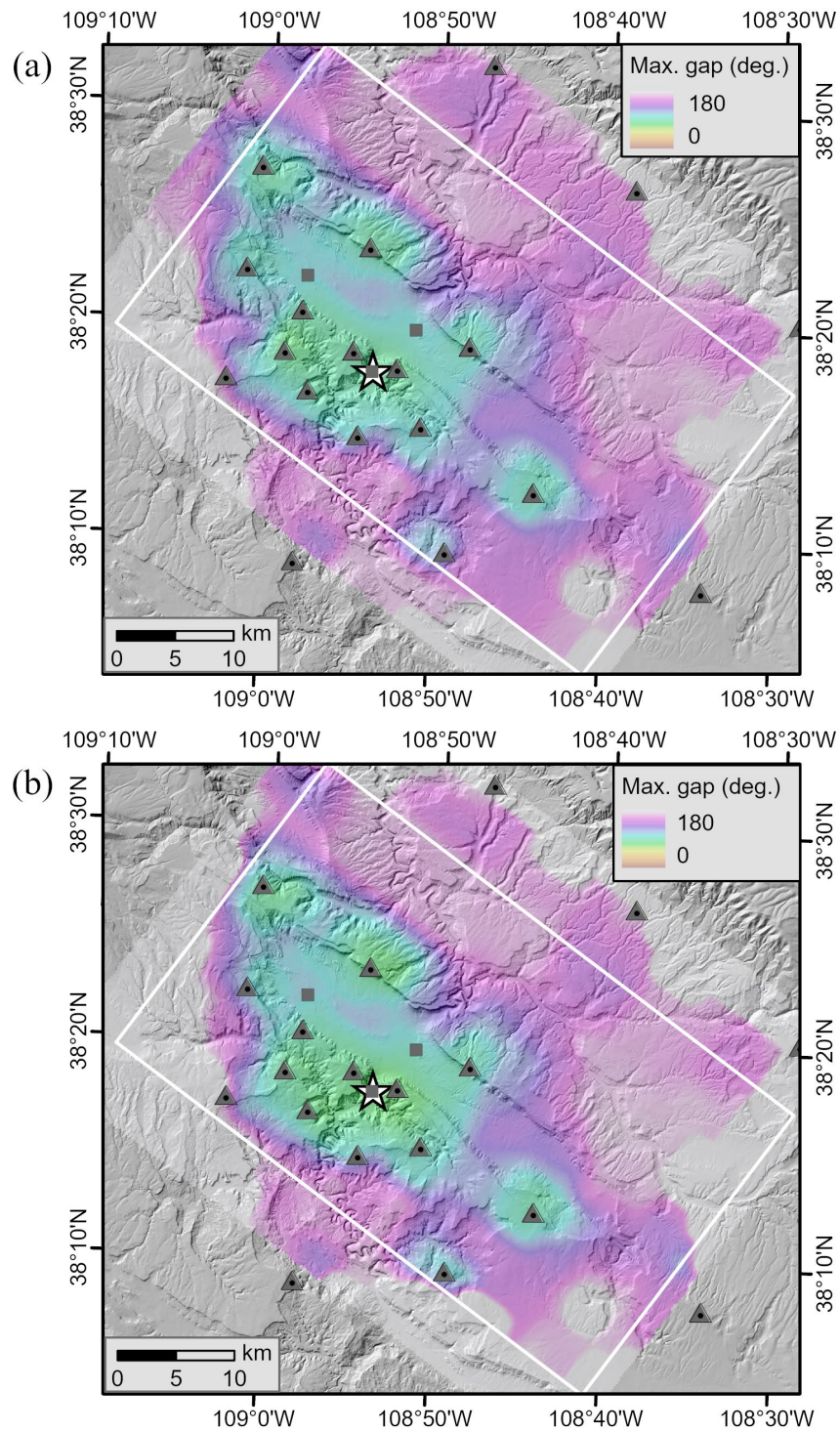


**Figure B-30: Horizontal section of the maximum gap in vertical angular ray coverage (deg.) for the final 3-D hypocenter-velocity inversion at an elevation of -2 km: (a) P waves (b) S waves. The white star is the location of the PVU injection well. The gray triangles are the locations of the broadband seismic stations, and the gray squares are the locations of the strong motion stations. The white rectangle is the area where velocities varied during the initial inversions.**

Technical Memorandum 86-68330-2024-7  
Development of a New Velocity Model for the Paradox Valley Area

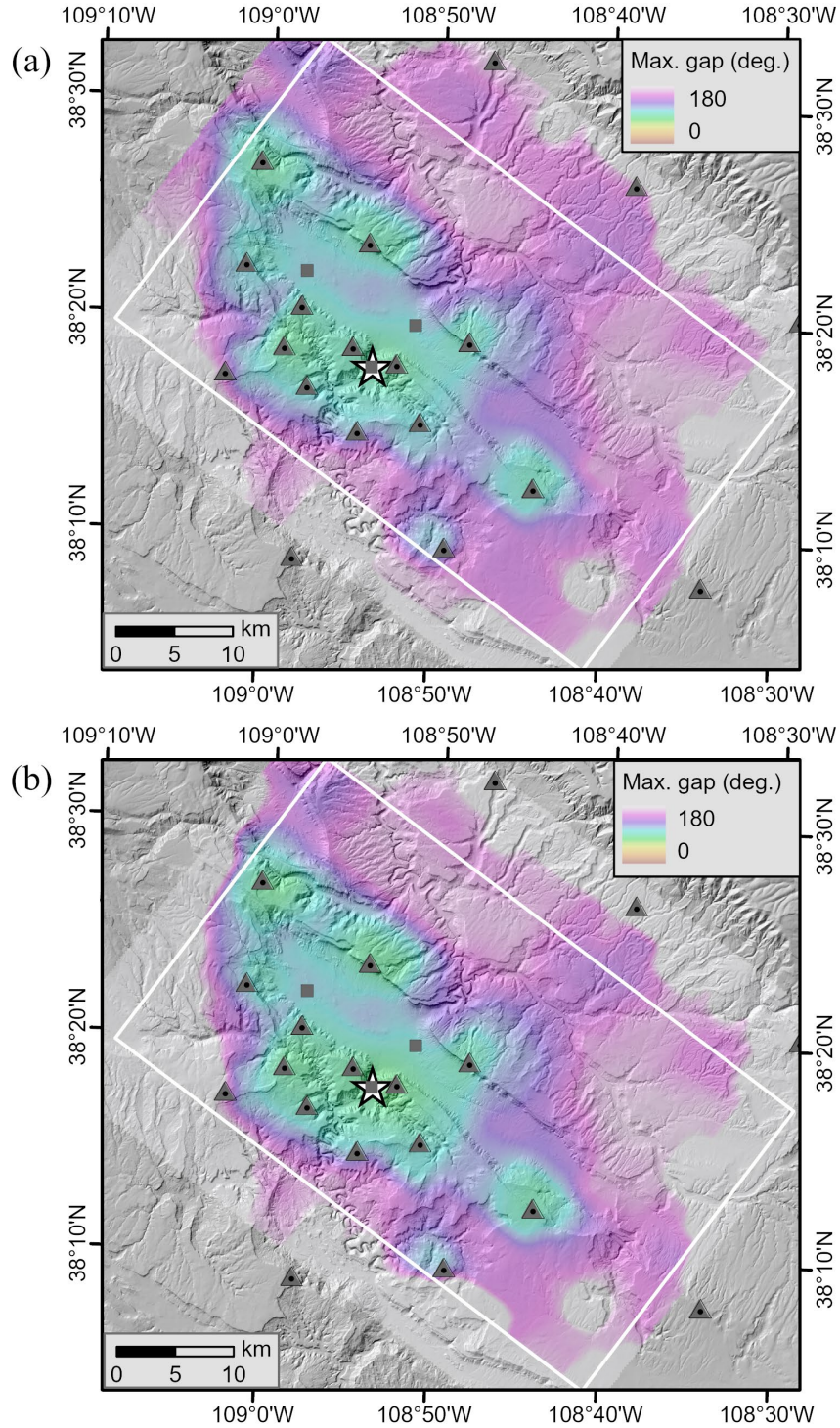


**Figure B-31: Horizontal section of the maximum gap in vertical angular ray coverage (deg.) for the final 3-D hypocenter-velocity inversion at an elevation of -3 km: (a) P waves (b) S waves. The white star is the location of the PVU injection well. The gray triangles are the locations of the broadband seismic stations, and the gray squares are the locations of the strong motion stations. The white rectangle is the area where velocities varied during the initial inversions.**



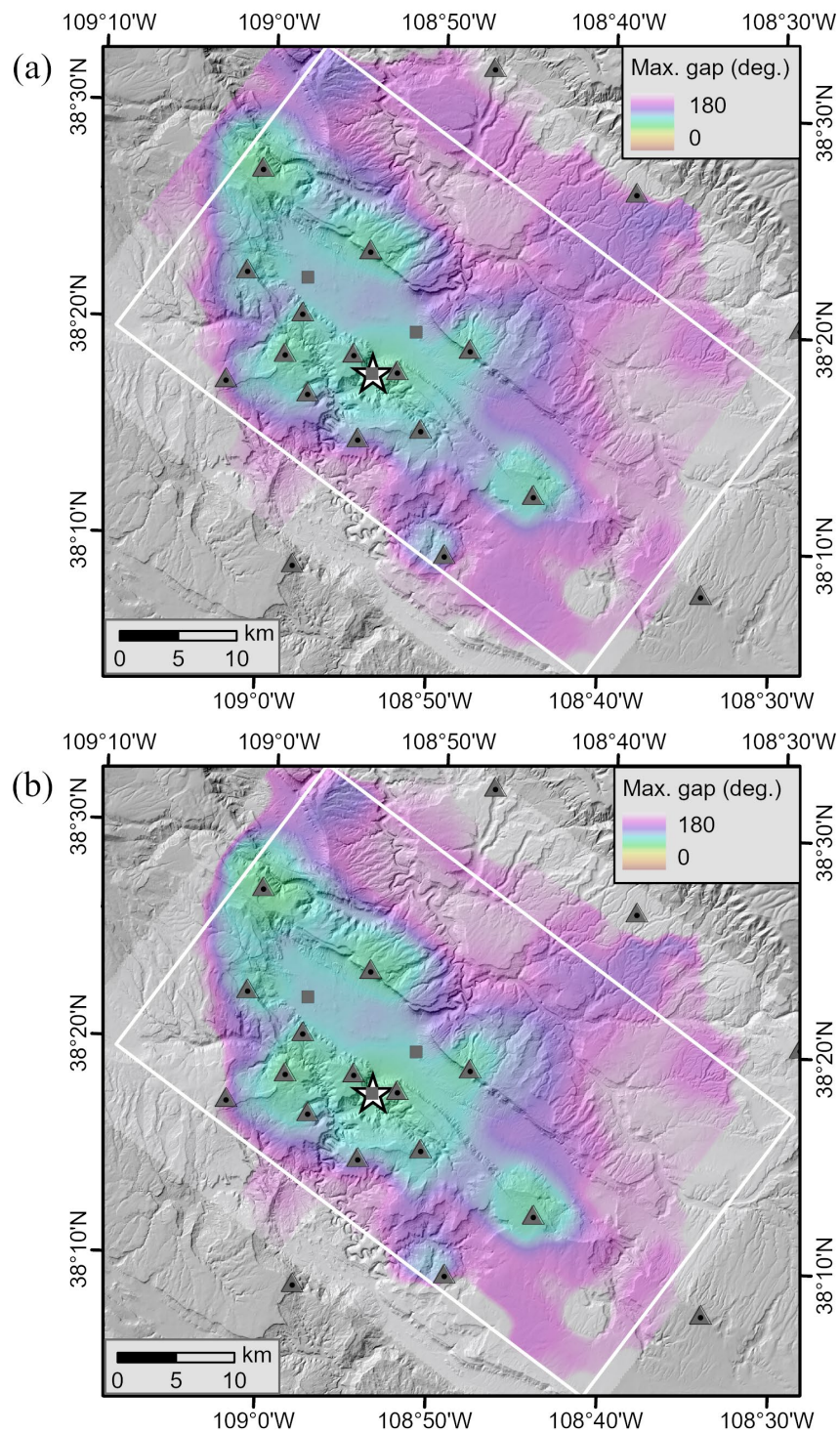


**Figure B-32: Horizontal section of the maximum gap in vertical angular ray coverage (deg.) for the final 3-D hypocenter-velocity inversion at an elevation of -4 km: (a) P waves (b) S waves. The white star is the location of the PVU injection well. The gray triangles are the locations of the broadband seismic stations, and the gray squares are the locations of the strong motion stations. The white rectangle is the area where velocities varied during the initial inversions.**

Technical Memorandum 86-68330-2024-7  
Development of a New Velocity Model for the Paradox Valley Area

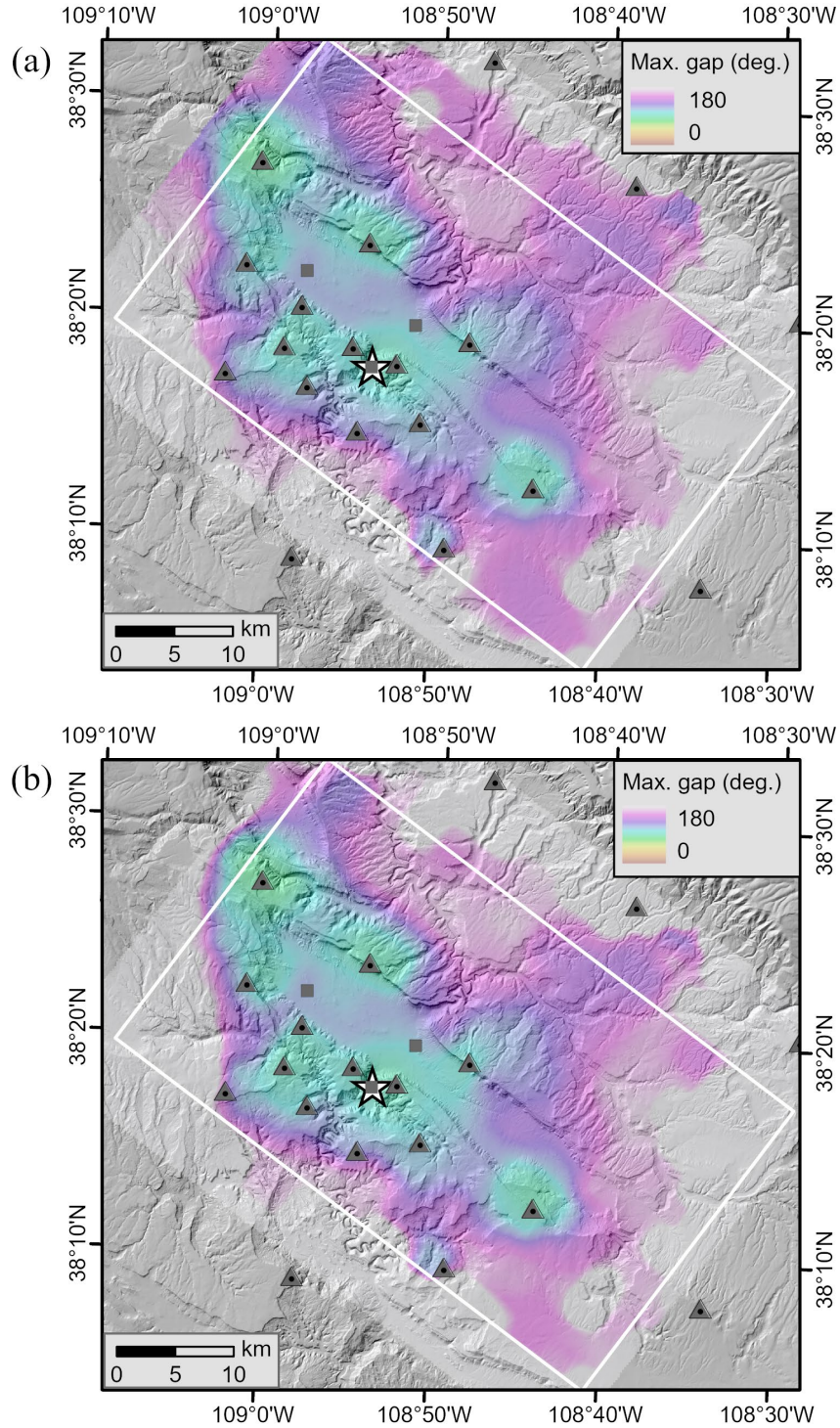


**Figure B-33: Horizontal section of the maximum gap in vertical angular ray coverage (deg.) for the final 3-D hypocenter-velocity inversion at an elevation of -5 km: (a) P waves (b) S waves. The white star is the location of the PVU injection well. The gray triangles are the locations of the broadband seismic stations, and the gray squares are the locations of the strong motion stations. The white rectangle is the area where velocities varied during the initial inversions.**



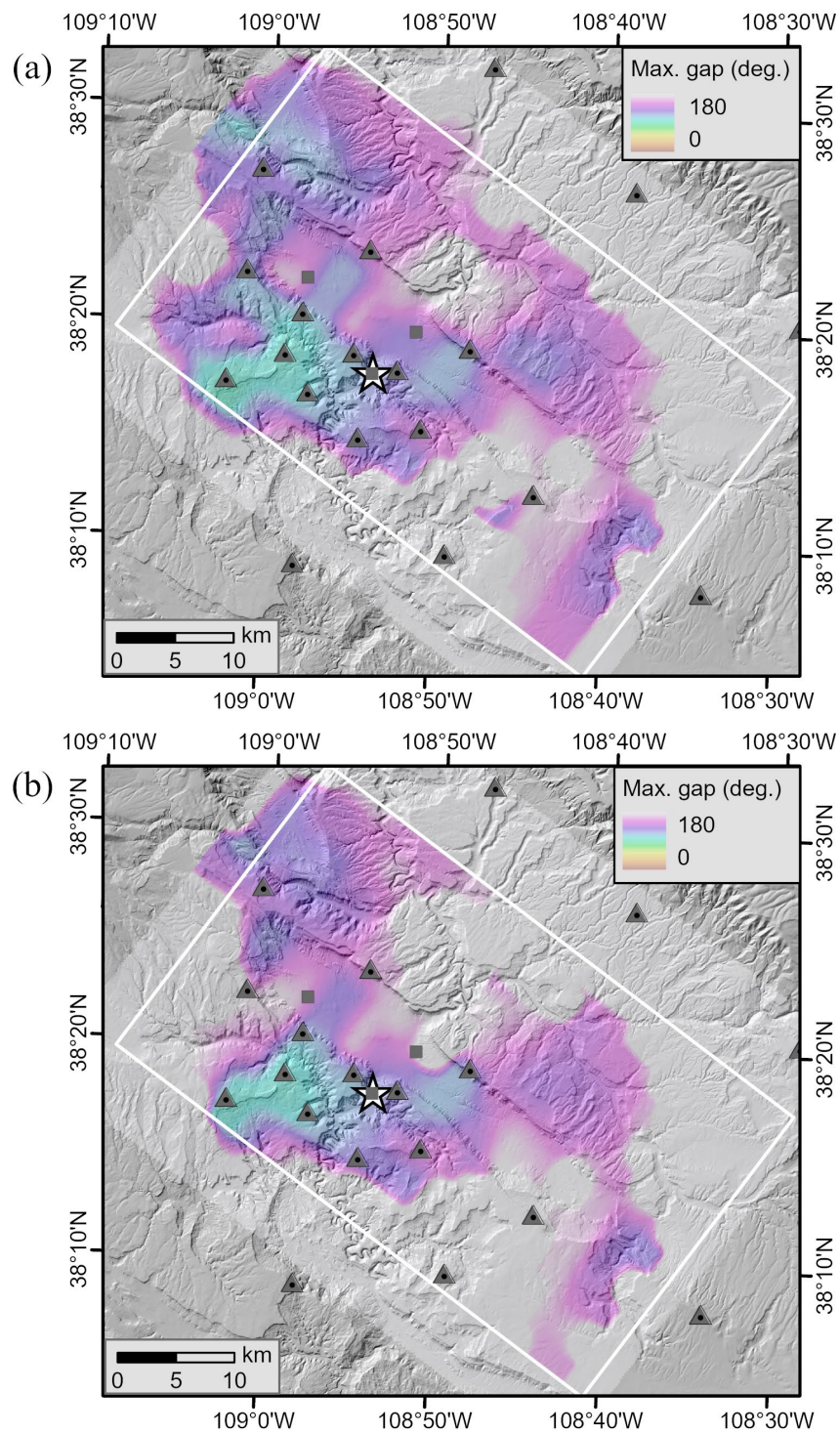


**Figure B-34: Horizontal section of the maximum gap in vertical angular ray coverage (deg.) for the final 3-D hypocenter-velocity inversion at an elevation of -10 km: (a) P waves (b) S waves. The white star is the location of the PVU injection well. The gray triangles are the locations of the broadband seismic stations, and the gray squares are the locations of the strong motion stations. The white rectangle is the area where velocities varied during the initial inversions.**

Technical Memorandum 86-68330-2024-7  
Development of a New Velocity Model for the Paradox Valley Area

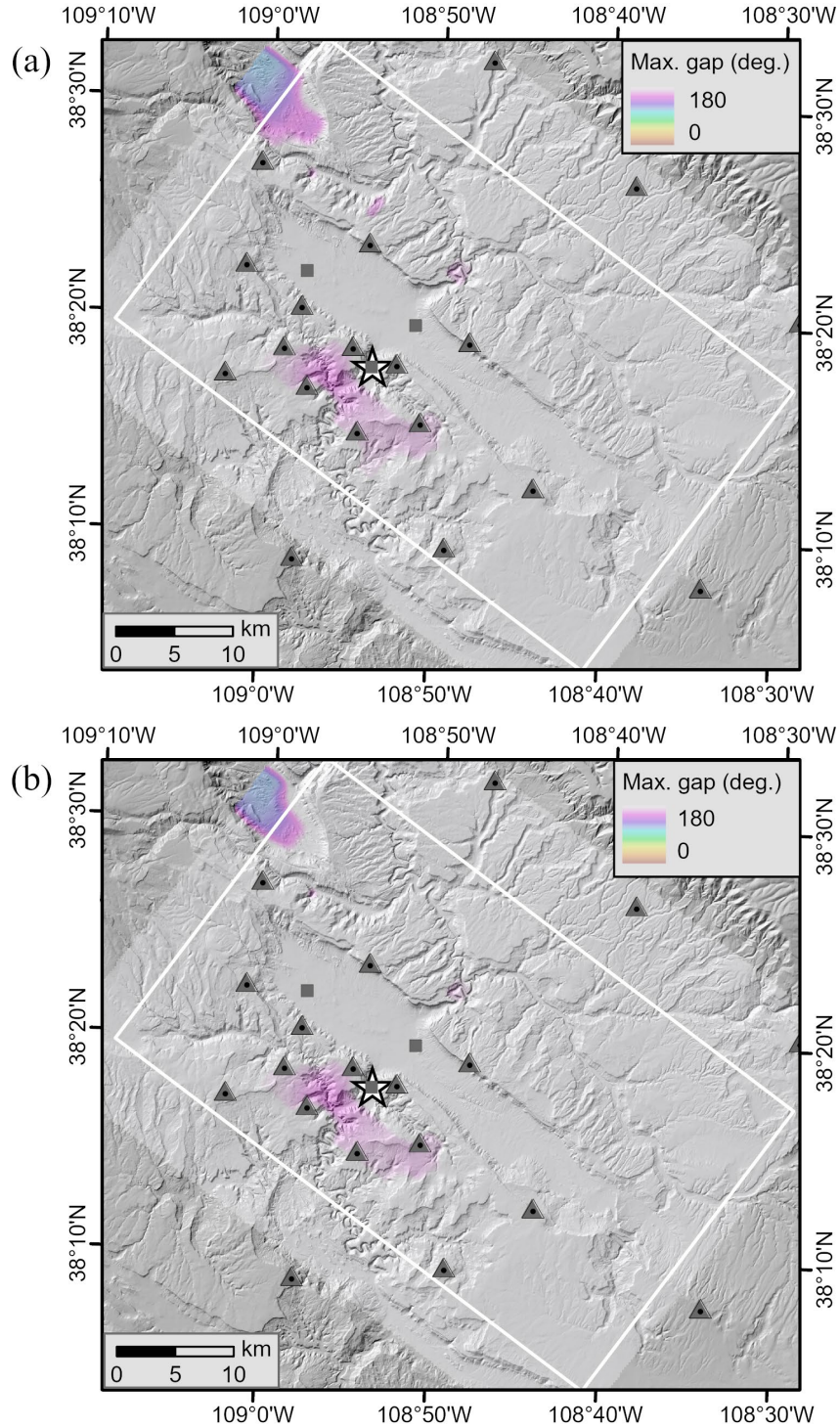


**Figure B-35: Horizontal section of the maximum gap in vertical angular ray coverage (deg.) for the final 3-D hypocenter-velocity inversion at an elevation of -15 km: (a) P waves (b) S waves. The white star is the location of the PVU injection well. The gray triangles are the locations of the broadband seismic stations, and the gray squares are the locations of the strong motion stations. The white rectangle is the area where velocities varied during the initial inversions.**



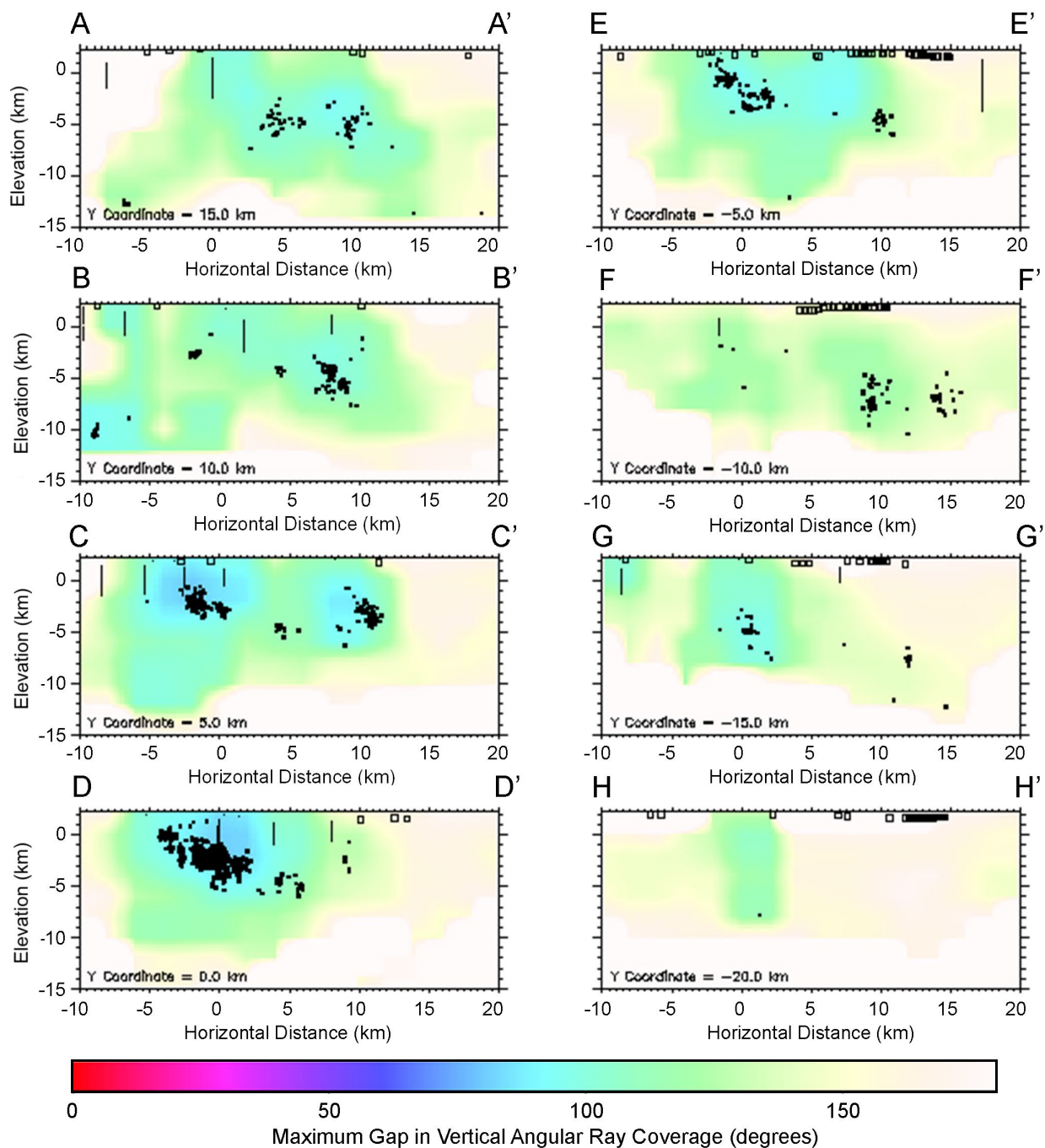


**Figure B-36: Vertical sections perpendicular to Paradox Valley of the maximum gap in P-wave vertical angular ray coverage (deg.) for the final 3-D hypocenter-velocity inversion. The cross sections are spaced 5 km apart; their locations are shown in Figure 3 10 of the main report. The earthquakes (black dots), explosions (open black squares), and well log data points (black lines) within 2.5 km of each section are projected onto the sections.**

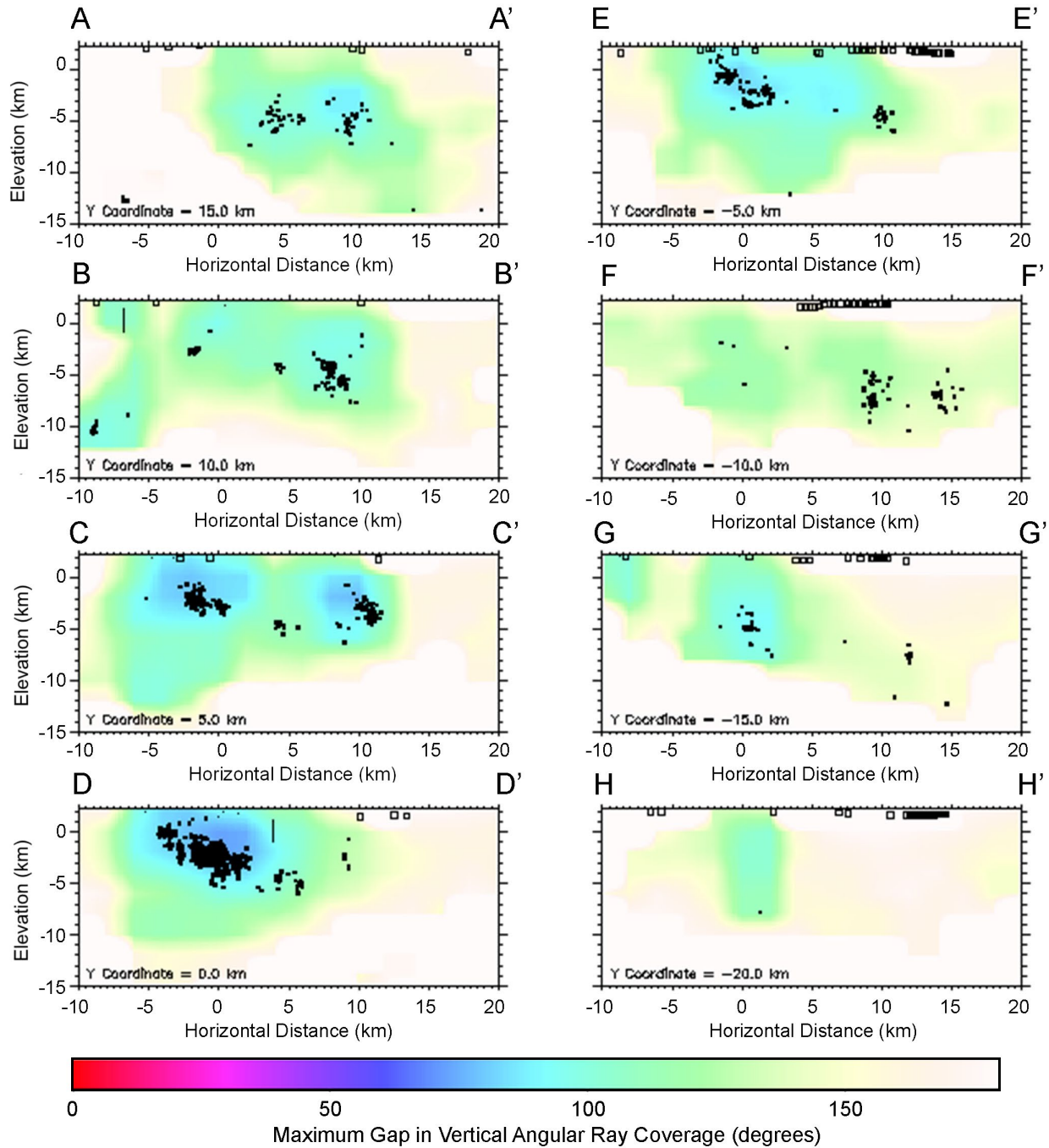


**Figure B-37: Vertical sections perpendicular to Paradox Valley of the maximum gap in S-wave vertical angular ray coverage (deg.) for the final 3-D hypocenter-velocity inversion. The cross sections are spaced 5 km apart; their locations are shown in Figure 3 10 of the main report. The earthquakes (black dots), explosions (open black squares), and well log data points (black lines) within 2.5 km of each section are projected onto the sections.**



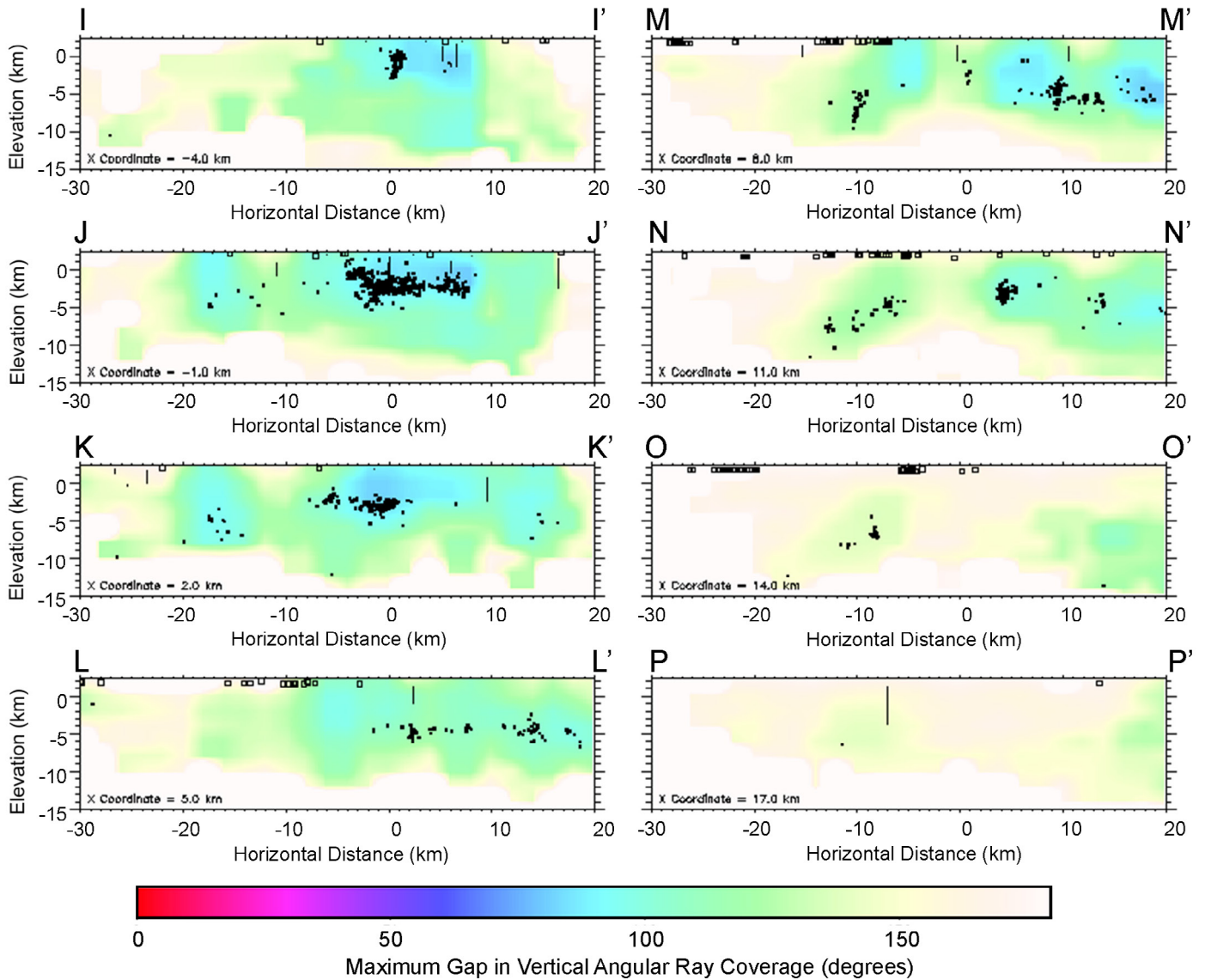


**Figure B-38: Vertical sections parallel to Paradox Valley of the maximum gap in P-wave vertical angular ray coverage (deg.) for the final 3-D hypocenter-velocity inversion. The cross sections are spaced 3 km apart; their locations are shown in Figure 3 10 of the main report. The earthquakes (black dots), explosions (open black squares), and well log data points (black lines) within 1.5 km of each section are projected onto the sections.**

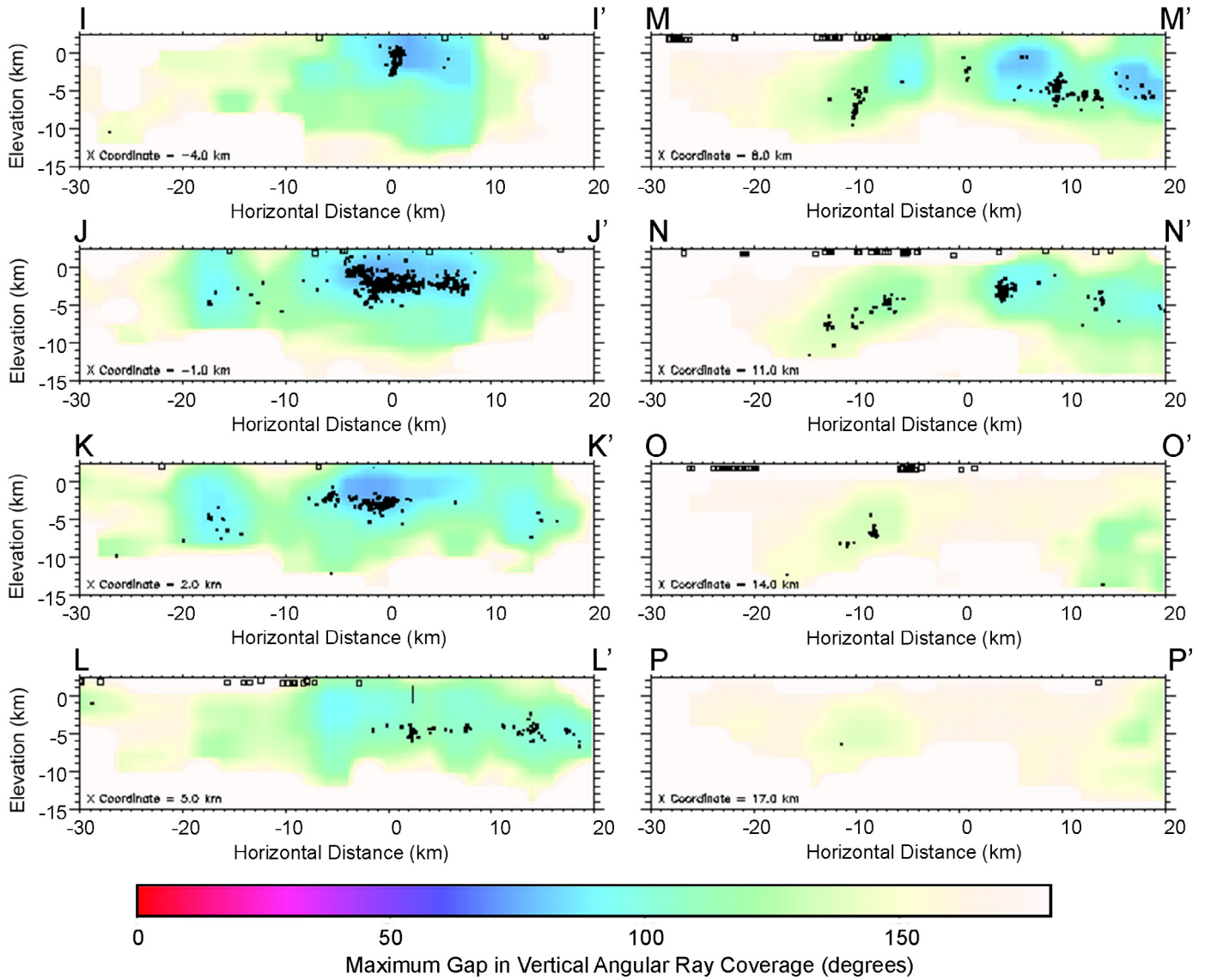


**Figure B-39: Vertical sections parallel to Paradox Valley of the maximum gap in S-wave vertical angular ray coverage (deg.) for the final 3-D hypocenter-velocity inversion. The cross sections are spaced 3 km apart; their locations are shown in Figure 3 10 of the main report. The earthquakes (black dots), explosions (open black squares), and well log data points (black lines) within 1.5 km of each section are projected onto the sections.**



## **Appendix C**

Electronic Attachment: 3-D Velocity Model and  
Station Corrections





The velocities and station corrections from the final 3-D hypocenter-velocity inversion are provided in an electronic attachment to this report. The station corrections, 3-D P-wave and S-wave velocity structures, and parameters for the Cartesian coordinate system are given in a single ascii file, “para\_vels.567”. The file consists of three parts:

1. Header - model ID and coordinate system information
2. Station corrections
3. Velocity model

Each part is described below.

**Part1 – header:**

Line 1 - project name

Line 2 - velocity model ID

Line 3 - *reflat reflon refdepth rotxy*

where:

*reflat, reflon* = the latitude and longitude of the origin of the Cartesian coordinate system (degrees)

*refdepth* = elevation of Reclamation’s internal depth datum (km); used to convert between depths computed by event locators that use 1-D velocity models and elevations computed in the event locator that uses the 3-D velocity model

*rotxy* = the horizontal rotation angle of the Cartesian system (degrees). The x and y axes are rotated by this angle counterclockwise from East and North, respectively.

For PVSN hypocenter calculations and velocity model development, the transformation between latitude and longitude and Cartesian coordinates is done using the software package *proj* (PROJ contributors, 2019), with an azimuthal equidistant (aeqd) projection and the Geodetic Reference System 1980 (GRS80) ellipsoid.

**Part 2 – station corrections:**

Line 1 = number of stations, *nsta*

Lines 2 to 1+*nsta* - *sname(i) pstcor(i) sstcor(i)*

where:

*sname(i)* = name of the *i*<sup>th</sup> station

*pstcor(i)* = P-wave station correction of the *i*<sup>th</sup> station (s)

*sstcor(i)* = S-wave station correction of the *i*<sup>th</sup> station (s)

Station corrections are added to the computed travel times.

**Part 3 – velocity model:**

Line 1 – numbers of velocity nodes in the x, y, and z directions

Line 2 – x coordinates of nodes (km) (line is wrapped)

Line 3 – y coordinates of nodes (km) (line is wrapped)

Line 4 – z coordinates of nodes (km) (line is wrapped). Z coordinates correspond to

elevations above mean sea level.

Block of P-wave velocities (lines are wrapped)

Block of S-wave velocities (lines are wrapped)

The P-wave and S-wave velocity blocks can be thought of as being listed as horizontal slices, from the minimum to maximum z coordinates. For each slice, the velocities are listed from the maximum to minimum y coordinates (i.e., from northwest to southeast for the Paradox Valley velocity model), and from minimum to maximum x coordinates (from southwest to northeast). Simplified lines from a Fortran code that would read the velocity part of the file are given below.

```
c Read grid coordinates. (1 = x direction; 2 = y direction; 3 = z direction)
  read(fileno,*) ngrid(1),ngrid(2),ngrid(3)
  read(fileno,*) (grid(1,i),i=1,ngrid(1))
  read(fileno,*) (grid(2,i),i=1,ngrid(2))
  read(fileno,*) (grid(3,i),i=1,ngrid(3))
c Read P-wave velocities
  do k=1,ngrid(3)
    do j0=1,ngrid(2)
      j=ngrid(2)-j0+1
      read(fileno,*) (pvel(i,j,k),i=1,ngrid(1))
    end do
  end do
c Read S-wave velocities
  do k=1,ngrid(3)
    do j0=1,ngrid(2)
      j=ngrid(2)-j0+1
      read(fileno,*) (svel(i,j,k),i=1,ngrid(1))
    end do
  end do
```

## References

PROJ contributors, 2019, PROJ coordinate transformation software library, Open Source Geospatial Foundation: URL <https://proj.org/>.